

**MODELING CHALLENGES OF ADVANCED THERMAL IMAGERS**

A Dissertation

Presented to

The Academic Faculty

By

Steven K. Moyer

In Partial Fulfillment

Of the Requirements for the Degree

Doctor of Philosophy in Electrical Engineering

Georgia Institute of Technology

August 2006

## MODELING CHALLENGES OF ADVANCED THERMAL IMAGERS

Approved by:

Dr. Gisele Bennett, Advisor  
School of Electrical and Computer  
Engineering  
*Georgia Institute of Technology*

Dr. John Buck  
School of Electrical and Computer  
Engineering  
*Georgia Institute of Technology*

Dr. William D. Hunt  
School of Electrical and Computer  
Engineering  
*Georgia Institute of Technology*

Dr. William T. Rhodes, Advisor  
School of Electrical and Computer  
Engineering  
*Georgia Institute of Technology*

Dr. Stephen P. DeWeerth  
School of Electrical and Computer  
Engineering  
*Georgia Institute of Technology*

Dr. Ronald G. Driggers  
Modeling and Simulation Division  
*Night Vision and Electronic Sensors  
Directorate*

Date Approved: December 14, 2005

What this feeble light leaves indistinct to the sight talent must discover,  
or must be left to chance. It is therefore again talent,  
or the favor of fortune, on which reliance must be placed,  
for want of objective knowledge.

Carl von Clausewitz, On War

This dissertation is dedicated to Richard and Louise Moyer  
whose reassurance and guidance throughout  
the years have made this possible.

## **Acknowledgements**

The author would like to thank a number of people who made this work possible. First and foremost is the steadfast support and encouragement provided by Gisele Bennett, William T. Rhodes, and Ronald G. Driggers. The expert opinions of Ted Corbin proved invaluable in the development and execution of the various field tests that were necessary in the completion of this work. The Urban Operations research team with their support of me and allowing me the time necessary to complete writing of this document. The Field Performance Branch for never letting me get bored. Finally, the U. S. Army, Night Vision, Electronic Sensors Directorate, who provided me the facilities to perform this research and brought together many of the exceptional people previously mentioned.

# Table of Contents

<b>Acknowledgements</b> .....	<b>iv</b>
<b>List of Tables</b> .....	<b>vii</b>
<b>List of Figures</b> .....	<b>viii</b>
<b>List of Abbreviations</b> .....	<b>xi</b>
<b>Summary</b> .....	<b>xiv</b>
<b>1 Introduction</b> .....	<b>1</b>
<b>2 Background</b> .....	<b>6</b>
2.1 Advanced Thermal Imagers .....	8
2.2 Thermal Imager Models .....	10
2.3 ACQUIRE Model .....	14
2.3.1 Historical Background .....	14
2.3.2 ACQUIRE Implementation .....	17
2.4 Sensor Measurements .....	21
2.4.1 Resolution Measurement: MTF .....	21
2.4.2 Sensitivity Measurement (Noise) .....	23
2.4.3 Human Performance Measurements .....	28
<b>3 Sampling</b> .....	<b>34</b>
3.1 Background .....	35
3.1.1 Historical Treatment of Sampling .....	37
3.1.2 Contemporary Treatment of Sampling .....	42
3.2 Experimental Design .....	48
3.2.1 Image Set and Preparation .....	49
3.2.2 Human Visual Perception Experiments .....	53
3.2.3 Experimental Results .....	54
3.3 Sampling Discussion .....	58
<b>4 Multiband Imaging</b> .....	<b>60</b>
4.1 Background .....	62
4.1.1 Historical Research .....	62
4.1.2 Principal Components Analysis (PCA) .....	65
4.1.3 Mathematical Description of Imaging Process .....	66
4.2 Data Collection .....	68
4.2.1 Temperature Calibration of Imagery .....	68
4.2.2 Field Test .....	71
4.2.3 Sensor Used .....	73
4.3 Correlation Analysis .....	77
4.4 Error Analysis .....	79
4.4.1 Dead Pixels .....	79
4.4.2 Thermal Imager Noise .....	80

4.5	Results.....	82
4.6	Multiband Discussion .....	86
<b>5</b>	<b>Target Acquisition Model for Handheld Objects .....</b>	<b>88</b>
5.1	Defining the Object Set.....	89
5.2	Image Collection.....	92
5.3	Image Processing for Experimentation.....	94
5.3.1	Mid-wave Infrared (MWIR) Spectrum.....	94
5.3.2	Long Wave Infrared (LWIR) Spectrum.....	96
5.3.3	Image Calculations.....	98
5.4	Experimental Methodology and Observer Results .....	100
5.5	Resolvable Cycles Calculations.....	102
5.6	Performance Model Predictions.....	105
5.7	Handheld Object Discussion.....	111
<b>6</b>	<b>Discussion .....</b>	<b>113</b>
<b>7</b>	<b>Recommendations .....</b>	<b>118</b>
<b>8</b>	<b>References .....</b>	<b>119</b>

## List of Tables

Table 1. List of all noise parameters from the 3-D noise model.[.].....	26
Table 3. Measured average pair-wise correlation coefficients for vehicles spanning their operational extent. (a) cold vehicles, (b) idled vehicles, and (c) exercised vehicles.	83
Table 4. Measured average pair-wise correlation coefficients of vehicles for specific hours over the day. (a) 1100 hours, (b) 1300 hours, and (c) 2100 hours.....	85
Table 5. Measured average pair-wise correlation coefficients of backgrounds for specific hours over the day. (a) 1100 hours and (b) 1300 hours. ....	85
Table 6. List of 33 items presented to law enforcement officers for ordering.....	90
Table 7. Ordered list of all items separated into categories.....	91
Table 8. Final list of objects imaged for the human perception experiments. ....	92
Table 9. Sensor specifications, heights, and ranges to the objects for each waveband. ...	93
Table 10. Experimental matrix showing the width of the applied blur parameters.....	96
Table 11. Average characteristic dimension and contrast for the image set for each experimental bin.....	99
Table 12. Johnson calibration factors for MWIR, and LWIR spectrum with coefficient of determination. ....	104
Table 13. Simulated ranges for the MWIR and LWIR spectrum with the corrected P(Id) at each range and the associated 95% confidence interval. ....	107
Table 14. Observer performance with MWIR range simulated imagery and model predictions for the same task.....	108
Table 15. Observer performance with LWIR range simulated imagery and model predictions for the same task.....	109
Table 16. Comparison of Loyd’s seven degrees of freedom as applied to past, present, and future generations of thermal imagers.....	114

# List of Figures

Figure 1. Relationship between the three primary components of an imager development program. Standard NATO agreements (STANAGs) exist that standardize the theoretical models and laboratory measurements used for thermal imagers. .... 6

Figure 2. Notional drawing of focal plane geometry with scan patterns. (a) A single detector focal plane. (b) A column of detectors on a focal plane array. (c) Several columns on a focal plane array. (d) A 2-dimensional detector grid which spans the FOV of the thermal imager. .... 8

Figure 3. Process for determining the probability of identification versus range curve for a given imager, atmospheric condition, and target set. (a) Necessary target and environmental descriptors are characteristic dimension, target contrast, range, and atmospheric transmission. (b) Intersection of target contrast at sensor and system performance curve (MRT) specifies the maximum number of resolved cycles per mrad. (c) Target Transfer Probability Function (TTPF) relates number of resolved cycles to visual task difficulty to compute probability. (d) Number of resolvable cycles changes due to the range to target, thereby creating new probability for each range. .... 18

Figure 4. MTF measurement using the super-resolution measurement method to overcome inadequate sensor sampling. (a) A schematic of the test configuration for a thermal imager measurement of MTF. (b) Representation of the edge function on the focal plane array. (c) Recombination of the data to produce a high resolution *esf*. (d) Final measured MTF. .... 22

Figure 5. Scene presented to sensor for a measurement of NETD.[.] ..... 24

Figure 6. Notional detector output scanned across a scene with a uniform target. .... 25

Figure 7. Noise cube with directional averaging operations to calculate the  $\sigma_{tv}$  parameter. .... 27

Figure 8. Example of two, 1-dimensional MRT's and the resultant 2-D MRT. .... 30

Figure 9. A simplified three-step sampled imaging system process in one dimension, where  $h(x)$  is comprised of atmospheric terms, optics, and detector blurs,  $s(x)$  represents the imager sample spacing, and  $p(x)$  is composed of all blurs occurring after sampling such as digital filters, and display blurs. .... 35

Figure 10. Notional plot of the sampled imager response function. (a) The pre-sample MTF  $H(f)$  is replicated at the sample frequency. The post-sample MTF  $P(f)$  filter both the baseband signal and the replicated signal. (b) The transfer response is the

pre-sample MTF multiplied by the post-sample MTF. The pre-sample replicas are also filtered by the post-sample MTF and become the aliased spectrum. ....	36
Figure 11. Graphical representation of Schade’s sampled imager guidance. ....	38
Figure 12. Leagalts design criteria as applied to the same imaging system shown in Figure 11. ....	40
Figure 13. Sequin criteria applied to a sampled imaging system. ....	41
Figure 14. An 2S3 self-propelled artillery piece at three different tactical ranges with the corresponding spatial frequency spectrum.....	46
Figure 15. Graphical representation of spatial frequency location for aliased components: (a) in-band aliasing, (b) mid-band aliasing, and (c) out-of-band aliasing. ....	47
Figure 16. Target set of images for the visual identification task.....	49
Figure 17. Original sized image used as a scene input for the controlled thermal imagers and the magnitude of its associated Fourier transform. ....	51
Figure 18. Results of the perception experiments to test the impact of aliasing allowed spatial frequency location on imager performance reduction. ....	56
Figure 19. Computed spurious response metrics using both the total integrated metric Equation (13), and the out-of-band metric Equation (15).....	58
Figure 20. Graphical representation of radiation path from emitter to detector for a spectrally filtered thermal imager. ....	67
Figure 21. Temperature reference image of the three fielded blackbodies.....	69
Figure 22. Example calibration curve for the first filter. ....	70
Figure 23. Histogram of image pixels after converting to radiometric equivalent blackbody source temperatures.....	71
Figure 24. Locations of vehicles and natural backgrounds during the field test portion of the research. ....	72
Figure 25. Front and side view of InSb midwave thermal imager with cold filter wheel. ....	74
Figure 26. Atmospheric transmission model and spectral wavebands for each cold filter. ....	76
Figure 27. Segmented image of 5-ton truck.....	77
Figure 28. Correlation coefficient decay as a function of applied image noise.....	81

Figure 29. Noise corrected correlation coefficients.....	82
Figure 30. Visible image illustrating the orientation of the objects to the thermal imagers. .....	93
Figure 31. Example MWIR images of all 12 objects at the same aspect.....	95
Figure 32. Example LWIR images of all 12 objects at the same aspect.....	98
Figure 33. Human observer results, corrected for chance, and shown by experimental cell as a function of the b parameter.....	101
Figure 34. Example of the MWIR vertical system CTF as calculated using Equation(28). .....	103
Figure 35. Resolvable cycles measured by the Johnson metric and the best fit curve for each spectrum.....	104
Figure 36. Measured probabilities of identification and NVTherm 2002 range performance predictions for both the MWIR and LWIR sensors.....	110

## List of Abbreviations

12AFC	12-Alternative Forced Choice
1-D	one-dimensional
2-D	two-dimensional
3-D	three-dimensional
AM	Ante Meridien
APC	Armored Personnel Carrier
CCD	Charged Coupled Device
COTS	Commercial Off The Shelf
CTF	Contrast Threshold Function
DARPA	Defense Advanced Research Project Agency
EDT	Eastern Daylight Time
EFL	Effective Focal Length
ERIM	Environmental Research Institute of Michigan
<i>esf</i>	edge spread function
FGAN-FFO	Forschungsgesellschaft fuer angewandte Naturwissenschaften
FLIR	Forward Looking Infrared
FOV	Field of View
HEMMT	Heavy Expanded Mobile Tactical Truck
HSI	Hyperspectral Imager
IFOV	Instantaneous Field of View
InSb	Indium-Antimonide

LWIR	Long Wave Infrared
MCT	Mercury-Cadmium-Teluride
MODTRAN	Moderate Spectral Resolution Atmospheric Transmission Algorithm
MRC	Minimum Resolvable Contrast
MRT	Minimum Resolvable Temperature
MRTD	Minimum Resolvable Temperature Difference
MSI	Multi-spectral Imager
MTDP	Minimum Temperature Difference Perceived
MTF	Modulation Transfer Function
MUSIC	Multi-Spectral Infrared Camera
MWIR	Mid-Wave Infrared
N <sub>50</sub>	50%-Probability of Correct Target Identification Resolvable Cycle Criteria
NASA	National Aeronautics and Space Administration
NATO	North Atlantic Treaty Organization
NETD	Noise Equivalent Temperature Difference
NVESD	Night Vision and Electronic Sensors Directorate
NVL	Night Vision Laboratory
PCA	Principal Components Analysis
PM	Post Meridien
QWIP	Quantum Well Infrared Photodetector
ROC-V	Recognition of Combat Vehicles
SITF	System Intensity Transfer Function
SNR	Signal-to-Noise Ratio

STANAG	Standard NATO Agreement
TDI	Time Delay Integration
TIMS	Thermal Infrared Multi-spectral Scanner
TNO	The Netherlands Organization
TOD	Triangle Orientation Discrimination
TTPF	Target Transfer Probability Function
TV	Television

## Summary

Unlike previous generations of thermal imagers, which use scanning detectors sensitive in either the 3 - 5 $\mu\text{m}$  or 8 - 12 $\mu\text{m}$  waveband, advanced or next-generation thermal imagers use two-dimensional (2-D) detector arrays that may be sensitive in more than one waveband. The performance and target acquisition capabilities of earlier-generation thermal imagers are well established and modeled in such programs as FLIR '92, NVTherm, and ACQUIRE<sup>1</sup>. These performance models guide thermal imager design and acquisition by allowing system designers and purchasers to perform theoretical tradeoff studies between various thermal imagers and to evaluate the impact of new technologies, such as quantum well infrared photodetectors (QWIPs). The introduction of advanced thermal imagers in combination with new operational spaces and scenarios creates new sensor performance modeling challenges. Some of these challenges include accurate prediction of sensor performance resulting from image under-sampling; determination of a suitable representation for mutual information in multi-waveband images; and suitable performance modeling of these sensors in the detection, recognition, and identification of nontraditional targets<sup>2</sup>. The advanced thermal imager research I report on in this dissertation provides (i) guidance for modeling the operational performance of thermal imaging sensors that produce under-sampled imagery, (ii) a methodology for the collection and assessment of information differences between multi-waveband images, and (iii) a model for thermal imager operational performance

---

<sup>1</sup> In this document, a "model" is a collection of mathematical formulas that quantitatively characterizes a sensor's physical attributes and capabilities. FLIR '92 and NVTherm model the MTF, noise, and sensitivity of thermal imager systems, while ACQUIRE utilizes the results of FLIR '92 and NVTherm to predict system range performance for a specific visual perception task.

<sup>2</sup> In this document, traditional targets are military vehicles. All other objects which the target acquisition process is applied are non-traditional targets.

prediction in the identification of handheld objects. My research advances thermal imager performance model understanding and provides guidance to system designers in the development of next-generation thermal imagers.

# 1 Introduction

During the past 30 years, thermal imagers have evolved from a single detector scanning configuration to the current two-dimensional (2-D) detector arrays, which can be sensitive to multiple wavebands. Concurrent with the development of first-generation thermal imagers, the U. S. Army began development of thermal imager performance models. The goal of thermal imager performance modeling was to develop mathematical equations that quantified the image quality a thermal imager produced and predicted the operational performance of an observer using the imager to complete a visual discrimination task. The initial thermal imager human performance models applied to imagers that scanned a column of detectors across the field of view (FOV). These models included the Ratches '76 model, FLIR '90, and FLIR '92. Both FLIR '90 and '92 were developed in parallel with second-generation thermal imagers, a 2-D focal plane array that scanned across the imager FOV. The 2-D focal plane array of second-generation thermal imagers consisted of only four columns of detectors requiring the scene to be scanned over the focal plane. Both FLIR '90 and '92 models were successful in predicting human performance for both first- and second-generation thermal imagers. However, advances in technology continued to improve and out-paced the current imager performance model development. This reduced the accuracy of the existing performance model predictions.

The existing models now provide insufficient guidance on quantifiable differences between various advanced infrared imagers. My research focuses on three areas that performance models either treat insufficiently or ignore: (i) modeling

performance of human observers viewing under-sampled imagery, (ii) assessing information differences in multi-waveband imagery, and (iii) modeling human performance for the visual discrimination task of identifying handheld objects.

To appreciate the significance of my research areas, a brief description of a third-generation thermal imager is provided. Current focal plane arrays consist of a 2-D, large format grid of detectors, which span the imager FOV. This focal plane array eliminates the need to scan the scene for image formation. These detector elements are large, 20 to 50 $\mu\text{m}$  on a side, as compared to visible spectrum detectors of  $\leq 10\mu\text{m}$ . Technology currently exists to stack several detector arrays on a common substrate, which allows for the capture of multiple images in different wavebands simultaneously. These different spectral images have perfect image spatial registration. Also, technological advancements now allow thermal imager operation without a cryogenic cooler. These un-cooled thermal imagers are smaller, lighter in weight, and, consequently, more mobile. The thermal imager may be as small as a rifle scope or head-mounted goggles. This advancement allows the imager to be taken into fundamentally different environments than have been previously modeled.

Earlier-generation thermal imagers utilize scanning methods for image formation, while advanced thermal imagers use a 2-D array of detectors that eliminates the need for scanning. Because of design rules from the television industry, it is wasteful to build a thermal imager with an array of detectors that produces a well-sampled image. Determining and modeling the performance impact of under-sampled images on human observer performance is the basis for my first research area focus. In addition to having a new detector array format, the detectors in these arrays can be sensitive to more than a

single broad waveband. For future models to account for these multi-waveband effects, it is necessary to understand, collect, analyze, and assess the image quality from different spectral bands. My second research area focus is on the collection and interpretation of information from a multi-waveband imager. By providing this image collection and interpretation methodology, I lay the foundation for future research efforts to complete the task of imager performance modeling for multi-waveband imagers. With the advent of new un-cooled sensors, thermal imagers are smaller and lighter in weight, and no longer restricted to vehicle platforms. Consequently, these sensors are being used in different operational environments. Previous research focuses on open-field engagements with military vehicles surrounded by a natural background, such as trees and grass. We need to verify and fully understand the imager performance models for an urban environment and for targets that are fundamentally different from military vehicles, e.g. civilian vehicles, clothing, and items which are held by people. Thus my final research area focus is to investigate and develop psychophysical models that quantify human observer performance in environments other than the classical open field engagement. The analysis addresses not just inanimate objects but also human beings interacting with these objects.

My research advances the body of knowledge for the thermal imaging community and imaging communities that operate in bands outside the thermal spectrum, such as Terahertz, millimeter wave, and television. My research assessing the impact on human performance of 2-D sampled thermal imager systems provides a methodology capable of addressing performance degradation for imagers operating in other spectral bands. The development of a methodology to assess information differences between different

spectral images is a first step towards the performance modeling of sensors that collect images of user-defined spectral content and then display these images simultaneously. The result of this segment of my research is useful to not only the broad-band thermal imager community, but also to the hyperspectral imaging community, and it provides a methodology for exploring and defining third-generation thermal imagers. My final research area shows that current validated psychophysical models already in use can be extended to fundamentally different objects in other spectral bands. The impact of this research allows thermal imager designers a more accurate evaluation of how changing various components affect human performance. The research also gives guidance to imaging communities employing systems to acquire and identify targets other than military vehicles. The understanding of the validity of human performance models to non-traditional targets has applications to homeland security, military force protection, and military urban operations. The results from this research are currently in use by system designers.

All three of my research areas contribute to the overall foundation for modeling the next generation of thermal imagers. However, since each area is unique and extensive, for coherence, my dissertation is organized with an over-arching background chapter followed by individual chapters for each of my research areas. The first chapter is a general background chapter intended to introduce the differences between advanced thermal imagers and their predecessors, the theoretical sensor model, the current validated human performance model, and the measurements that are needed to characterize thermal imagers. This general background chapter is followed by individual chapters for each of the three research topics. Within each topic chapter are sections that

include background specific to the research topic, the research that has been performed, and a discussion of the results of this research. I conclude the dissertation with a discussion chapter addressing the entire body of research, how these topics have advanced the body of knowledge, and recommendations for future work.

## 2 Background

Illustrated in Figure 1 are the three primary components associated with thermal imager research and development: theoretical models, field performance tests and models, and laboratory measurements. These three components are necessary for a successful thermal imager development program. The STANAGs shown in Figure 1 are standard NATO agreements which dictate which theoretical models, laboratory measurements, and field performance tests are used for the evaluation of thermal imagers.

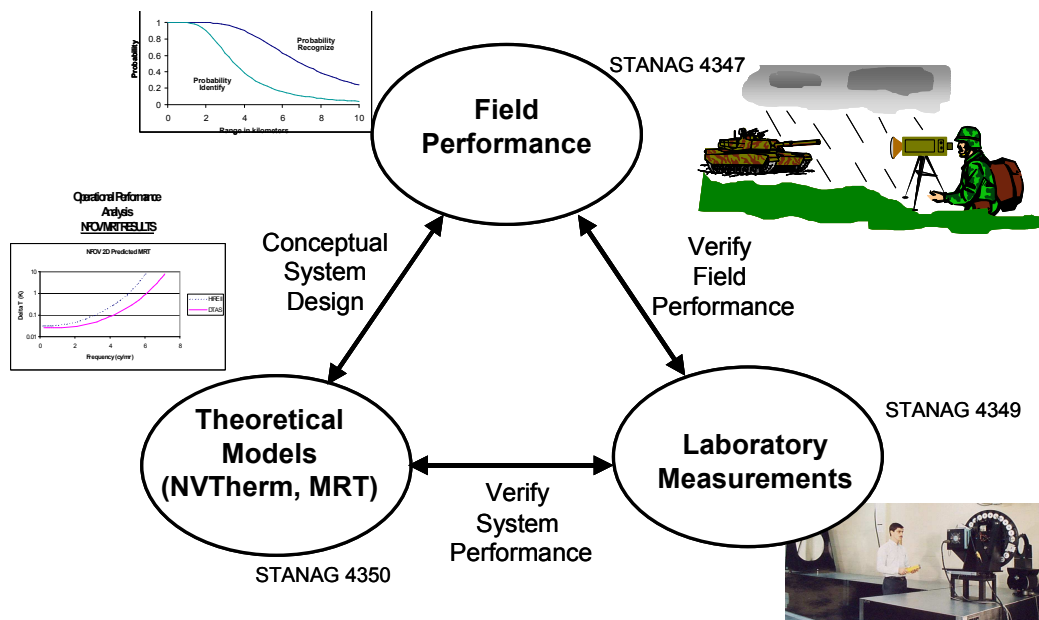


Figure 1. Relationship between the three primary components of an imager development program. Standard NATO agreements (STANAGs) exist that standardize the theoretical models and laboratory measurements used for thermal imagers.

Theoretical thermal imager models are used to evaluate new conceptual designs and describe thermal imager sensitivity, resolution, and human performance (visual

acuity through the thermal imager). These models use the underlying physics of the imaging system and predict how the interactions of the physical quantities affect human performance in an integrated system. Some physical characteristics in these models include the system Modulation Transfer Function (MTF), Noise Equivalent Temperature Difference (NETD), and Minimum Resolvable Temperature Difference (MRTD).

Target acquisition models are used to relate the theoretical thermal imager models to system field performance. This link allows theoretical models to predict field performance quantities, e.g., probabilities of detection, recognition, and identification. Field performance is measured outside the laboratory to refine the theoretical models and make them more accurate for advanced sensor applications. Since field performance activities are expensive, methods for the direct measurement of sensor performance are developed for the laboratory.

Laboratory measurements of sensor performance are developed both to validate theoretical models and to allow the prediction of field performance of a thermal imager given actual thermal imager measurements. The validation of the theoretical models occurs through comparing such measurements as system MTF and noise. Laboratory measurements should match the theoretical models predictions and also the field performance predictions.

Thermal imager characterization programs require accurate theoretical models, field performance measurements or predictions from acquisition models, and repeatable laboratory measurements. This triangle of development is successful for both first-generation and second-generation thermal imagers. However, with advanced thermal imager development, it is becoming increasingly difficult to maintain an accurate set of

theoretical sensor models, field performance models, and applicable laboratory measurements.

## 2.1 Advanced Thermal Imagers

The thermal imagers developed in the 1970s and 1980s were scanning sensors. Thermal imagers were designed to scan one detector or column of detectors across a scene and reconstruct the image through coordinated raster scanning on a display. With a single detector scanned across the scene, a uniform image could be rendered and, theoretically, a spatially well-sampled image could be obtained. With single-detector scanning sensors, the detector dwell time --the fraction of time the detector spends integrating a particular point in the scene-- was typically quite small and as a consequence, the signal-to-noise ratio (SNR) of early thermal imagers was low.

To increase the dwell time for a given detector, the scene was scanned across a column of detectors, as shown in Figure 2(b).

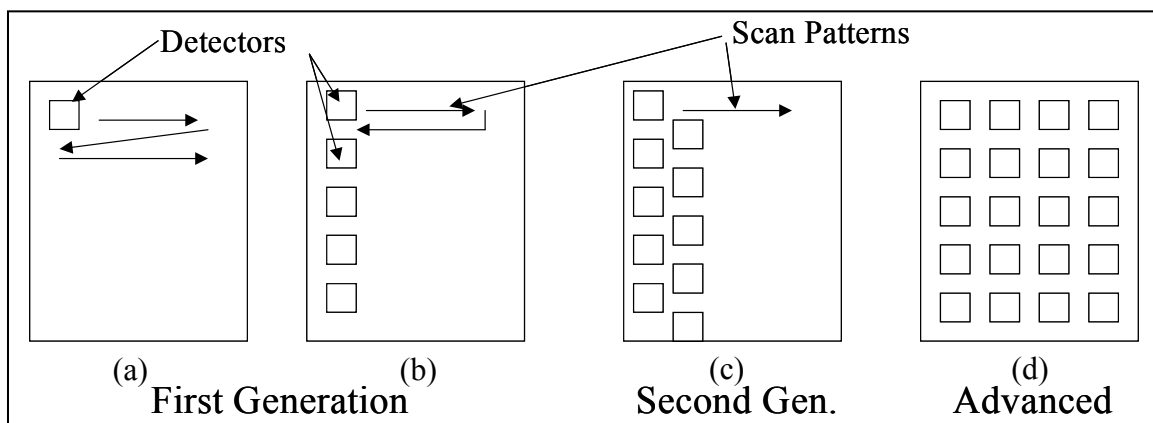


Figure 2. Notional drawing of focal plane geometry with scan patterns. (a) A single detector focal plane. (b) A column of detectors on a focal plane array. (c) Several columns on a focal plane array. (d) A 2-dimensional detector grid which spans the FOV of the thermal imager.

Since several detectors were used, each detector was allowed to image a different part of the scene, and longer dwell times were possible. The information provided in the horizontal or scan direction was analog and the vertical dimension was sampled by the detectors in the linear array. This scanning method introduced problems of non-uniform sensitivity between detectors and usually resulted in an image that was spatially under-sampled in the vertical dimension. Nevertheless, using a column of detectors improved the sensitivity of the sensor. For a given frame rate, the scene scan rates could be reduced compared to a single detector imager, and a spatially well-sampled image could still be produced in the horizontal dimension.

Second-generation thermal imagers employed multiple columns of detectors --for example, two or four columns placed side by side, as shown in Figure 2(c). This configuration of detectors allowed for time-delay integration (TDI) or the ability to sum together the outputs of adjacent columns. TDI allowed the same portions of the scene to be efficiently scanned multiple times, and, with temporal registration, the resulting independent scenes were co-added to produce an image with a higher SNR. During the development of these first- and second-generation thermal imagers, mathematical models were created to allow an independent comparison of the various technologies being utilized. The performance and target acquisition capabilities of first-generation thermal imagers were modeled with the Ratches '75 model and second-generation thermal imagers were modeled with improvements resulting in FLIR '90 and FLIR '92 models which were community-wide accepted standards [1].

Unlike these previous generations of thermal imagers, advanced thermal imagers, illustrated in Figure 2(d), utilize a staring array, or 2-D grid, of detectors and do not

require image scanning. The advent of the staring array has allowed very long integration times for the thermal imager detectors, with an associated increase in image SNR. Because of the new focal plane geometry and the progress in manufacturing detector elements from new materials, these thermal imager models need to be updated to accurately reflect the system impact on human performance.

## ***2.2 Thermal Imager Models***

Thermal imager models were a group of mathematical equations that took physical parameters as inputs and provided as output a characteristic curve describing the thermal imager performance. Johnson [2], working with image intensifiers, determined that the ability of an observer to detect, recognize, or identify military targets in a scene was closely correlated with how well the observer could resolve, through a viewing/acquisition device, bar patterns of varying frequencies at the same contrast as the target-to-background contrast. Subsequent research showed that this concept allowed the in-laboratory viewing of bar patterns, known as the minimum resolvable contrast (MRC) measurement, to be directly compared to the performance of sensors in a field environment. Converting the work of Johnson to thermal imagers, Ratches produced the first thermal imager model in 1975 [3]. In keeping with the Johnson hypothesis, a method was required to calculate the thermal imager response to four-bar targets.[4] This method or calculation attempted to predict the laboratory measurement of MRT, which is discussed in detail in section 2.4.3. The thermal imager MRT curve divided the contrast/spatial frequency space into a region where a four-bar pattern was resolvable and

a region where it was not resolvable. The first thermal imager MRT model was the Ratches '75 model given by

$$MRT(f_B) = \left( \frac{2.25\pi F^2}{\sqrt{14} H_{Tot}(f_B) f_{\lambda_1}^{\lambda_2} D^*(\lambda) \frac{\partial L(\lambda)}{\partial T} d\lambda} \right) \cdot \left( \frac{\alpha f_B Q(f_B) \Delta Y}{\eta_{OV} t_e A_d N} \right)^{1/2} \quad (1)$$

where

- F is the F-number of the optics (unitless),
- $H_{Tot}(f_B)$  is the total system MTF,
- $D^*(\lambda)$  is the detector specific detectivity (cm- $\sqrt{\text{Hz/W}}$  or Jones),
- $\partial L(\lambda) / \partial T$  is the partial of radiance with respect to temperature (W/cm<sup>2</sup>-sr- $\mu\text{m-K}$ ),
- $\alpha$  is the horizontal FOV (mrad),
- $f_B$  is the spatial frequency measure (cyc/mrad),
- $Q(f_B)$  is the spatial integration of the eye over a bar (unitless),
- $\Delta Y$  is the vertical instantaneous field of view (IFOV) of a detector (mrad),
- $\eta_{OV}$  is the overscan ratio (unitless),
- $t_e$  is the eye integration time (seconds),
- $A_d$  is the detector area (cm<sup>2</sup>),
- N is the number of detectors scanned and summed in series (unitless).

The only eye quantity included in this model is the eye integration time and MTF. This model did not take into account the contrast sensitivity of the human visual system, when the overall system performance was limited due to contrast. However, this model performed well with first-generation thermal imagers that were noise-limited.

With increased detector sensitivity and dwell time, thermal imagers eventually reached a point where imager noise was not the limiting factor, but, rather the human

visual system contrast sensitivity was the limiting factor. Vollmerhausen [5] incorporated an eye sensitivity function, the contrast threshold function (CTF), into the MRT calculation and also provided changes to incorporate improved human eye MTFs. The incorporation of eye parameters allowed the model to take into consideration such parameters as the distance of the observer from the display, whether one or two eyes were used, the effect of average display brightness on the observer, and the effect of glare on the display from outside light sources. These and other improvements led to the MRT equation used in NVTherm 2002:

$$MRT(\xi) = \left[ \left( \frac{2 \cdot S_{tmp} \cdot CTF(\xi)}{M_{Display} \cdot H_{Baseband}(\xi)} \right)^2 + \left( \frac{K_{eye} \cdot CTF(\xi) \cdot F\#^2 \cdot \pi \cdot \xi \cdot \sqrt{BW \cdot BL}}{M_{Display} \cdot H_{Baseband}(\xi) \cdot D_{\lambda Peak}^* \cdot \delta \cdot f \cdot \tau_{Optics} \cdot SL \cdot \sqrt{2 \cdot t_{eye} \cdot \eta_{eff}}} \right)^2 \right]^{1/2} \quad (2)$$

where

$S_{tmp}$  is the scene thermal contrast which results in average display luminance (Kelvin),

CTF is the human contrast threshold function (unitless),

$M_{Display}$  is the contrast available on the display (unitless),

$H_{Baseband}$  is the system MTF (unitless),

$K_{eye}$  is the eye threshold calibration constant (unitless),

$F\#$  is the f-number of the optical system (unitless),

$\xi$  is the spatial frequency variable (cyc/mrad),

$f$  is the effective focal length of the optics (cm),

$D_{\lambda Peak}^*$  is the peak specific detectivity of the detectors (cm- $\sqrt{Hz/W}$  or Jones),

$\tau_{Optics}$  is the transmission through the optics (unitless),  
 $t_{eye}$  is the eye integration time (seconds),  
 $\eta_{eff}$  is the scan efficiency of the sensor (unitless),  
 $\delta$  is the detector response integral (W/cm<sup>2</sup>-sr- $\mu$ m-K),  
 $S_L$  is the spatial signal integral (cm<sup>2</sup>),  
 $B_W$  and  $B_L$  are the spatial noise integrals for the width and length of the bar pattern (cm<sup>2</sup>) respectively [6].

Equation (2) was the MRT equation for a single dimension, either vertical or horizontal. The 2-dimensional MRT could be calculated by taking the geometric mean of the vertical and horizontal MRT at each contrast. Rearranging the terms of Equation (2), one obtains

$$\frac{MRT}{2S_{tmp}} = \left( \frac{CTF(\xi)}{M_{Display} \cdot H_{Baseband}(\xi)} \right) \cdot \left[ 1 + \left( \frac{K_{eye} \cdot F\#^2 \cdot \pi \cdot \xi \cdot \sqrt{B_W \cdot B_L}}{D \lambda_{Peak}^* \cdot \delta \cdot f \cdot \tau_{Optics} \cdot 2S_{tmp} \cdot S_L \cdot \sqrt{2 \cdot t_{eye} \cdot \eta_{eff}}} \right)^2 \right]^{1/2} \quad (3)$$

This formulation of the MRT equation is known as the thermal imager system CTF equation. The first term of the equation contains the human visual system CTF, the thermal imager system MTF, and the display contrast term. The second term contains the various thermal imager properties such as optics transmission and detector material properties as well as noise terms, eye integration time, and eye threshold calibration constant. It should be noted that if thermal imager noise is zero, Equation (3) simplifies to

$$\frac{MRT}{2S_{tmp}} = \frac{CTF(\xi)}{M_{Display} \cdot H_{Baseband}(\xi)} \quad (4)$$

This form of the thermal imager system CTF equation is only dependent upon the thermal imager system MTFs and has no other wavelength dependent parameters, which is useful

if a thermal imager is emulated in a synthetic environment, or if thermal imager noise does not limit human performance.

## **2.3 ACQUIRE Model**

The field performance model, ACQUIRE, has been in development since the late 1980s. ACQUIRE uses the MRT curves from FLIR '90, '92, or NVTherm 2002, to predict the performance of a human observer performing a visual discrimination task such as detection, recognition, or identification of targets. This section provides an in-depth historical look at the development of imager performance modeling, followed by a section on the mathematical workings of the ACQUIRE model. The historical section begins with the 1958 Johnson paper [7] and concludes with the refinements that Vollmerhausen and others provided. [3, 8-11] The mathematical section provides an in-depth description of how ACQUIRE works.

### **2.3.1 Historical Background**

The primary goal of thermal imager performance modeling is to quantify the performance differences that exist between different thermal imagers on the basis of a human's ability to perform a visual discrimination task. Visual discrimination tasks for the U. S. Army are detection, recognition, and identification. For my research, consistent with the usage of these terms in the target acquisition community [12], detection is defined as determining which region of an image, if any, the observer thinks possesses a military asset, vehicle or human, to the extent that the observer stops searching and takes an action, such as changing the thermal imager FOV. Recognition is defined as

discriminating between diverse categories of objects such as tanks, armored personnel carriers (APCs), or self-propelled artillery. Identification is defined as discriminating between objects within a diverse class such as a T-72, a T-62, a Leopard 2, or an M1A1, which are all tanks. These definitions are not universal but instead vary between imaging communities. However, each community does recognize that several layers of visual discrimination tasks exist, with some tasks being easier than others. The thermal imager performance model takes into account various physical parameters that describe the quality of imagery produced by a thermal imager an observer would use to accomplish the discrimination tasks just described.

In 1958 John Johnson, of the U.S. Army Night Vision Laboratory (NVL), proposed what is considered to be the seminal hypothesis for the U.S. Army's target acquisition model [7]. Johnson hypothesized that the ability of an observer to detect, recognize, or identify military targets in a scene was closely correlated with how well he could resolve, through a viewing/acquisition device, bar patterns of varying frequencies at the same contrast as the target-to-background contrast. Johnson performed an experiment [2] that used scale models of eight different military vehicles and one soldier as targets. These targets were placed against a featureless background in the laboratory. Observers viewed the targets through image intensifiers and performed detection, recognition, and identification visual perception tasks, as defined earlier. U. S. Air Force three-bar charts with the same contrast as the scale targets were used to establish the limiting contrast performance of the image intensifiers. By this means, the maximum number of resolvable cycles across the target's critical dimension was determined for each task. The target critical dimension was defined as that distance that represented the

distinguishing features of the target. It was found that the number of cycles an observer could resolve across the critical dimension of each target was within 25 percent of a fixed number of cycles required to perform each discrimination task. For this particular set of targets, one cycle was needed for detection, four cycles for recognition, and 6.4 cycles for identification. These cycle criteria, designated  $N_{50}$ , are for a 50 percent success rate in a visual task performance. Through the cycle criteria, the ability of the observers to perform these target discrimination tasks outside the laboratory was related to their ability to resolve bar patterns inside a laboratory environment. For most vehicles, the target critical dimension was the vertical dimension independent of profile. Therefore, this model did not predict the improved range performance that occurs when an observer views a tactical vehicle from the side versus viewing the vehicle from the front. The Johnson model visual discrimination performance predictions were conservative. However, the assumption that the contrast ratio of a bar pattern could be compared to a visual discrimination task was a starting point for target acquisition and imager performance modeling.

Lawson, Ratches, Johnson, Vollmerhausen, and others evolved a target acquisition range performance model based on Johnson's work and extended the original work from image intensifiers to thermal imagers [3, 8-11]. In the more recently developed target acquisition models, the square root of the target area presented to the thermal imager is used rather than the target critical dimension [4]. This change has two consequences: first, the original perception model used only the horizontal resolution of the sensor compared to the critical dimension of the target to predict sensor performance. For most vehicles, the critical dimension was the vertical dimension. The recent model

uses both the horizontal and vertical resolution characteristics of the sensor, requiring the characterization of both dimensions. Second, this change allows the model to predict the improved range performance that occurs when a tactical vehicle is viewed from the side. The original model was also changed to incorporate the limitations of the human eye [5,13]. Incorporating eye parameters forced system designers to take into consideration the additional parameters mentioned in section 2.2. The incorporation of the eye contrast threshold function (CTF) allowed the modeling of thermal imager performance limited by contrast and rather than sensor noise.

### **2.3.2 ACQUIRE Implementation**

The method for producing a probability of target identification curve for a given thermal imager and atmospheric condition is shown in Figure 3. Five parameters are needed to generate a probability of discrimination curve as a function of range for static imagery: (i) inherent target-to-background contrast, (ii) characteristic dimension, square root of the target area, (iii) atmospheric transmission within the waveband of interest, (iv) thermal imager MRT, as predicted by the theoretical thermal imager model, and (v) a quantified measure of the discrimination difficulty for the set of targets. It should be noted that for this model to predict the probability of visual task performance, the thermal imager is completely represented by the MRT curve.

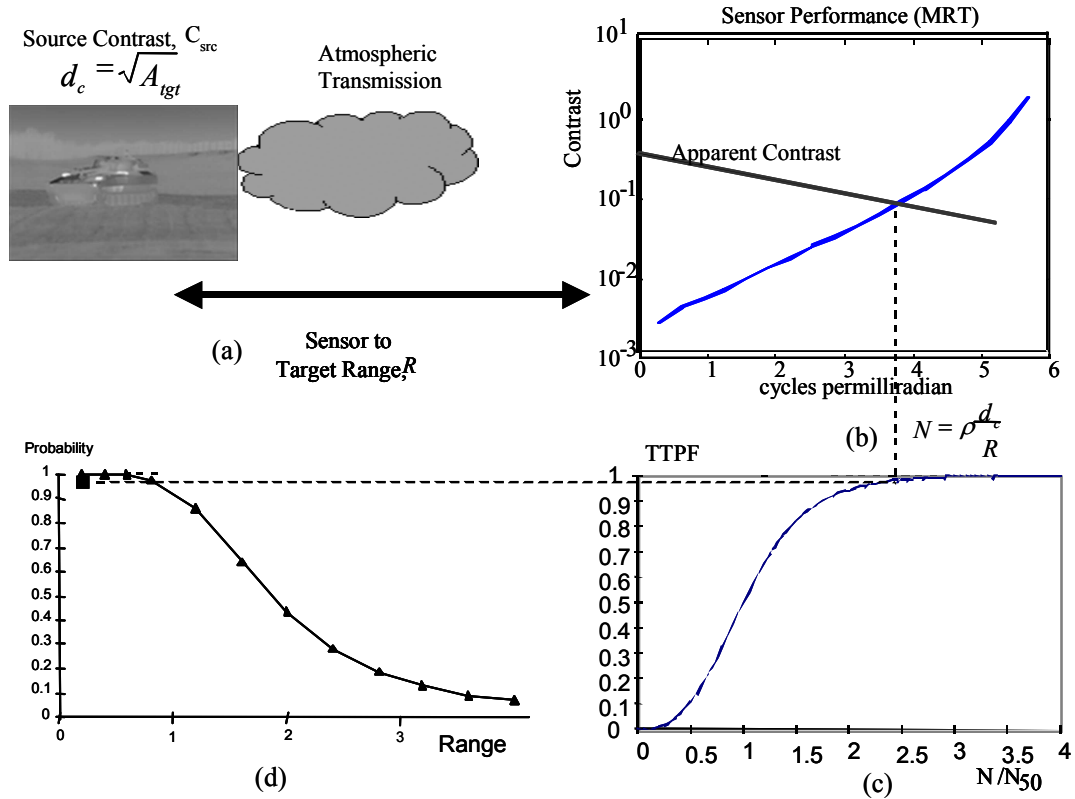


Figure 3. Process for determining the probability of identification versus range curve for a given imager, atmospheric condition, and target set. (a) Necessary target and environmental descriptors are characteristic dimension, target contrast, range, and atmospheric transmission. (b) Intersection of target contrast at sensor and system performance curve (MRT) specifies the maximum number of resolved cycles per mrad. (c) Target Transfer Probability Function (TTPF) relates number of resolved cycles to visual task difficulty to compute probability. (d) Number of resolvable cycles changes due to the range to target, thereby creating new probability for each range.

The target set is statistically represented by two quantities, the average characteristic dimension and the average inherent contrast. The characteristic dimension,  $d_c$ , shown in Figure 3(a), is calculated as the square root of the target area presented to the thermal imager. The inherent target-to-background contrast equation defines the target  $\Delta T_{RSS}$  as

$$\Delta T_{RSS} = \sqrt{\sigma_{igt}^2 + \Delta \mu^2} \quad (5)$$

where  $\sigma_{igt}$  is the standard deviation of the target temperature and  $\Delta \mu$  is the difference in average temperature between the target and the background adjacent to the vehicle. The atmospheric transmission and corresponding path radiance are determined and an apparent target contrast is calculated at the thermal imager. The highest resolved frequency of the system is the intersection of the target apparent contrast and the system MRT, as shown in Figure 3(b).

Once the highest system spatial frequency that can be resolved as a result of target contrast is determined, the number of resolvable cycles across the target characteristic dimension,  $N$ , can be calculated using

$$N = \rho \frac{d_c}{R} \quad (6)$$

where  $\rho$  is the maximum resolvable spatial frequency in cycles per milliradian for the thermal imager at the target apparent contrast,  $d_c$  is the target characteristic dimension, and  $R$  is the range from the thermal imager to the target. The probability of target identification is determined using the target transfer probability function (TTPF) shown in Figure 3(c) and given by the equation

$$P_{ID}(N) = \frac{\left(\frac{N}{N_{50}}\right)^{\left(2.7+0.7 \cdot \left(\frac{N}{N_{50}}\right)\right)}}{1 + \left(\frac{N}{N_{50}}\right)^{\left(2.7+0.7 \cdot \left(\frac{N}{N_{50}}\right)\right)}}, \quad (7)$$

where  $N_{50}$  is the number of resolved cycles required on the average target for a 50 percent probability of object identification for the given target set.

The ACQUIRE model assumes that there are a number of physical characteristics that improve the probability of target identification outside the thermal imaging system design. The model predicts improved performance with larger targets, closer ranges, higher target-to-background contrasts, and higher atmospheric transmission. For the thermal imager system, any change that produces a modeled performance curve, MRT, requiring less contrast to see higher frequencies will produce a better range performance curve for a given task, target set, and environmental conditions. The  $N_{50}$  parameter represents the difficulty an observer has in performing a visual task. Given an  $N_{50}$ , a different system MRT curve, and different atmospheric conditions, the range performance for an ensemble of targets may be evaluated for a specific thermal imager.

Throughout this discussion, the thermal imager MRT curve used in the ACQUIRE model is the modeled performance curve and not the curve one would obtain from the sensor MRT measurement. As mentioned earlier in section 2.2, for first- and second-generation thermal imagers, the measurement of the system MRT agreed well with the field performance and model predictions. With the advent of advanced thermal imagers and staring focal plane array systems, the measurement of the MRT for the imaging system no longer produces good agreement among laboratory measurement, field performance, and model predictions. The ACQUIRE model describes the performance of an average of observers performing a visual task against a set of targets. ACQUIRE is also incapable of predicting performance from multiple spectral inputs as are encountered with advanced thermal imagers.

## **2.4 Sensor Measurements**

The performance of a thermal imager is characterized by resolution, sensitivity, and the ability of a human to perceive a scene through the thermal imager. There are two measurements that objectively characterize a thermal imager resolution and sensitivity; MTF and noise, respectively. The other measurement is the subjective MRTD or MRT. MRT is the measure of human visual acuity through a thermal imager. These measurements are discussed in the following sections.

### **2.4.1 Resolution Measurement: MTF**

The MTF is a measure of the spatial frequency throughput of a sensor. An experimental setup for measuring MTF is shown in Figure 4(a) [14]. A point source target is projected into a collimated space and is the input to the thermal imager. The width of the resulting blur spot, or point spread function, is measured and transformed into the Fourier spatial frequency domain. The magnitude of the resulting function is the thermal imager MTF. The width of this function characterizes the spatial frequency throughput of the thermal imager to include the thermal imager optics, detectors, electronic filters, and display.

The point source method is difficult to realize and implement. For an alternative method, the thermal imager MTF is assumed to be separable in Cartesian coordinates into two one-dimensional functions. This assumption allows slit and edge targets to be used to measure the system MTF normal to the direction of the slit or edge instead of a point source. For example, utilizing an edge function to perform the measurement, the thermal imager under test is placed in the optical system, as shown in Figure 4(a) [14], with an edge target as the input scene. Taking a single line of pixels from the image normal to the

edge function produces the thermal imager representation of the edge or the edge spread function (*esf*). Differentiating the *esf* response determines the point spread function for the imager in one dimension. Once the point spread function is determined, the MTF is obtained in the same manner as for a point source. However, the resulting MTF is one-dimensional. The MTF in the perpendicular direction may be measured by rotating the input edge by 90°. This method works well for the scanned first- and second-generation thermal imagers. For insufficiently sampled thermal imagers, a slight modification to the edge target measurement is required.

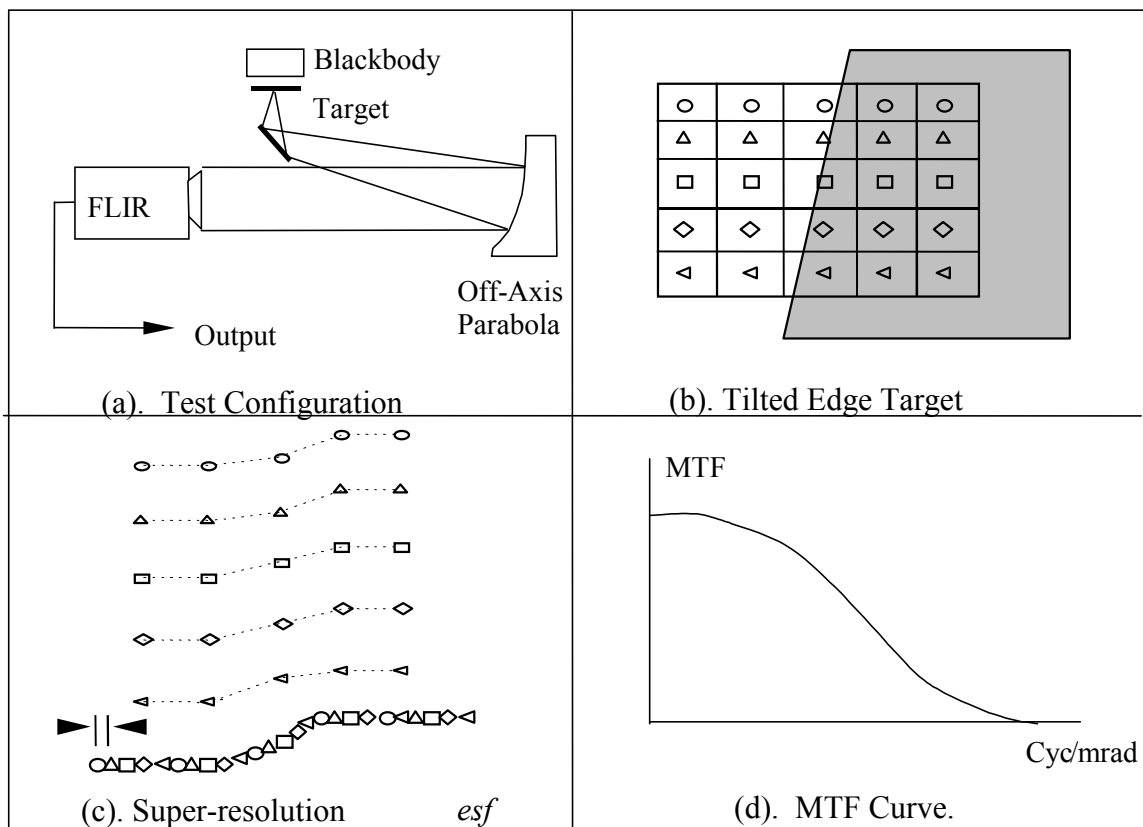


Figure 4. MTF measurement using the super-resolution measurement method to overcome inadequate sensor sampling. (a) A schematic of the test configuration for a thermal imager measurement of MTF. (b) Representation of the edge function on the focal plane array. (c) Recombination of the data to produce a high resolution *esf*. (d) Final measured MTF.

To measure the MTF of a thermal imager that produces under-sampled imagery, the thermal imager under test is placed in the optical system, as shown in Figure 4(a). An edge target is again the input to the thermal imager. However, the edge target is tilted relative to the detector grid [14-17]. The tilt allows the edge target to obscure incrementally less detector area between the detectors, as shown in Figure 4(b). The portion of the image that contains the slanted edge is isolated, as shown in Figure 4(c). By taking the vertical pixel values along the edge target, a higher resolution *esf* is measured because of the additional sampling achieved via the tilt of the edge. The sample spacing for this measurement becomes the original sensor sample spacing divided by the number of pixels used to create the super-resolved *esf*. Once the data has been reshaped, the derivative is calculated, which approximates the one-dimensional point spread function and the MTF is determined as before.

This measurement technique applies to the ideal case in which the image of the step function contains minimal amounts of noise. If significant levels of noise are present in this measurement, the derivative operation amplifies the noise and potentially leads to improper characterization of the MTF. A method to mitigate large quantities of temporal noise is the summation of several frames,  $N$ . Assuming the noise is not temporally correlated, the summation will improve the SNR by a factor  $\sqrt{N}$ .

#### **2.4.2 Sensitivity Measurement (Noise)**

Noise equivalent temperature difference (NETD) and three-dimensional (3-D) noise quantify thermal imager sensitivity. NETD is a measure developed for scanning thermal imagers. To measure NETD, a thermal imager is operated at its maximum scan rate with

a reference filter in place to standardize the thermal imager bandwidth and is presented with a uniform target against an ambient temperature background, as shown in Figure 5.

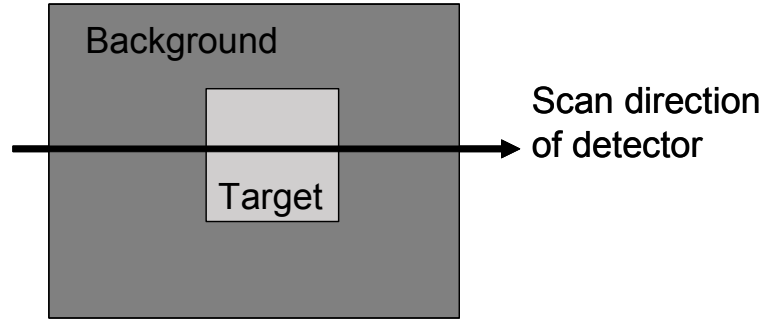


Figure 5. Scene presented to sensor for a measurement of NETD [18].

Dereniak and Boreman [18], calculated NETD as

$$NETD = \frac{\Delta T}{\left( \frac{v_{signal}}{v_{noise}} \right)}, \quad (8)$$

where  $v_{signal}$  is the peak signal voltage from the transition of the detector between the background and target,  $v_{noise}$  is the rms voltage value of the noise level around the ambient temperature measured from the background, and  $\Delta T$  is the temperature difference between the target and background, as shown in Figure 6.

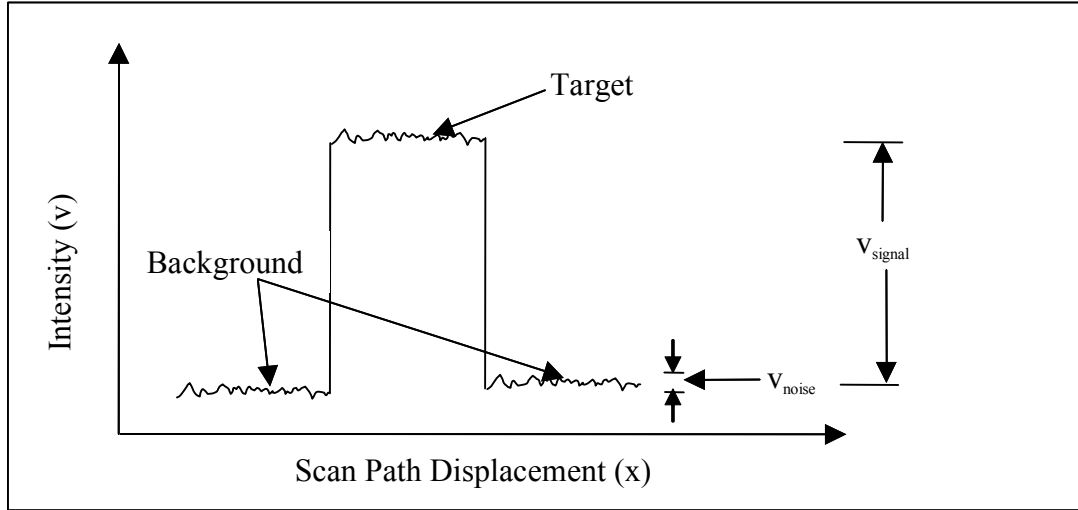


Figure 6. Notional detector output scanned across a scene with a uniform target.

In scanning thermal imagers, the NETD measurement is made on a detector-by-detector basis. Hence, NETD is an excellent characterization of temporal noise for thermal detectors. For staring array thermal imagers, unless several detectors are scanned over the background and target scene, this measurement quantity is misleading as a characterization. If a staring array thermal imager is not scanned, the comparison of  $v_{\text{signal}}$  to  $v_{\text{noise}}$  is made between different detectors imaging different portions of the input scene. The consequence affects the representation of fixed pattern noise in the NETD value. Thermal imager integration time also affects this measurement. A longer integration time results in a lower temporal noise in Kelvin. It is clear that a different noise measurement technique is required for staring array thermal imagers.

The 3-D noise measurement technique requires the collection of a noise cube. A noise cube is a set of sequential images of a source at ambient temperature consisting of  $X$  rows,  $Y$  columns, and  $Z$  frames, consistent with the definition of a cube  $X=Y=Z$ . Noise cubes are obtained by placing a laboratory blackbody emitter directly in front of a

thermal imager. This ensures that the entire sensor field of view is a uniform temperature (ambient) and emissivity is constant within the tolerance of the source. To correct for the roll-off trends in every row and column of the noise cube, no more than a second-order polynomial is fit to the data. This allows for the accurate measurement of the high frequency pixel-to-pixel and image-to-image noise characteristics without measuring optical effects such as  $\cos^4$  trends. Once these trends are removed, the cube is converted from counts to apparent blackbody temperatures in Kelvin. Eight different noise parameters are measured from the cube and are presented in Table 1.

Table 1. List of all noise parameters from the 3-D noise model [19].

Noise Term	Description	Source
$\sigma_{tvh}$	Random spatio-temporal noise	Detector temporal noise
$\sigma_{tv}$	Temporal row noise	Line processing, readout
$\sigma_{th}$	Temporal column noise	Scan effects
$\sigma_{vh}$	Bi-directional fixed pattern noise	Pixel processing, detector non-uniformity
$\sigma_v$	Line-to-line non-uniformity	Detector non-uniformity
$\sigma_h$	Column-to-column non-uniformity	Scan effects, detector non-uniformity
$\sigma_t$	Frame-to-frame noise	Frame processing
$\Omega$	Overall noise parameter	
S	Average of all noise components	

“Directional averaging” is performed to isolate the various noise parameters as shown in Figure 7 [1, 14, 19-22].

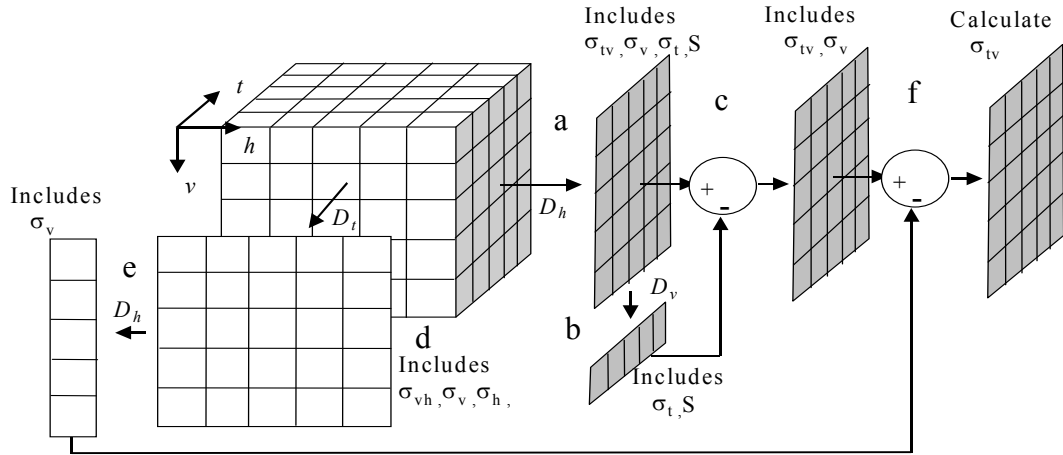


Figure 7. Noise cube with directional averaging operations to calculate the  $\sigma_{tv}$  parameter.

For example, to find the  $\sigma_{tv}$  noise parameter, in step a an average is taken across all the columns of the image cube, leaving a 2-D structure that possesses  $X$  rows and  $Z$  frames. An average is then taken across all the rows, step b, leaving a 1-D structure in the direction of time. The standard deviation of this data,  $Z$  frames, is then the  $\sigma_t$  noise parameter. Subtracting this value, in step c, from the  $X$  rows and  $Z$  frames data leaves just the  $\sigma_{tv}$  and  $\sigma_v$  noise parameters. Averaging across the frames of the image cube in step d produces a 2-D structure of  $X$  rows and  $Y$  columns. Step e averages across the columns leaving a 1-D structure of  $X$  rows, and the standard deviation of this is the  $\sigma_v$  noise parameter. Subtracting this  $\sigma_v$  parameter from the previous  $X$  rows and  $Z$  frames in step f leaves only the  $\sigma_{tv}$  noise parameter. An assumption of 3-D noise is that each noise component is uncorrelated with the other noise components.

This representation of noise is more descriptive than the single number of NETD, but it also contains the temporal measurement of noise as NETD. It has also correlated

some of the parameters to specific noise sources, thus providing designers useful feedback for the design of future thermal imagers.

### **2.4.3 Human Performance Measurements**

Human performance measurements are those laboratory measurements conducted to determine the visual acuity of an observer looking through a thermal imager. These measurements require that human observers view thermal imager target patterns. For scanning thermal imagers, these measurements have been correlated to measurements of range performance. However, with the advent of staring array sensors, this correlation to range performance is no longer valid. To address the inadequacies of this measurement, NVESD (U.S.A.), TNO (Netherlands), and FGAN-FFO (Germany) have proposed replacement measurements. This section begins with the classical US Army MRT measurement, progress through the U.S. approach for under-sampled thermal imagers and the Dutch triangle orientation detection (TOD) measurement, and concludes with the German minimum temperature difference perceived (MTDP).

#### **2.4.3.1 Minimum Resolvable Temperature: MRT**

MRT is the most controversial measurement that is performed on thermal imaging systems because this measurement is subjective and may not be repeatable between individuals or repeatable for the same individual at different times. The goal of the MRT measurement is to relate the resolution *and* sensitivity characteristics of the thermal imager to human visual acuity performance.

The thermal imager is placed in a test configuration, as shown in Figure 4(a). The target in front of the blackbody consists of four bars, with the bars being either horizontally or vertically oriented to the thermal imager. The starting temperature is sufficiently high to produce a high contrast four-bar pattern on the output of the thermal imager when compared to the ambient background. The differential temperature is then lowered on the blackbody until all four bars of the target are barely visible. This temperature is recorded. The temperature is lowered until the bars appear colder than the background. Again, the temperature is adjusted until the bar pattern is just visible and then recorded. The absolute average of these two recorded temperatures is taken to be the temperature (contrast) required to see a four-bar target of that specific spatial frequency. By varying the spatial frequency of the bar patterns and repeating this measurement, a curve is plotted that relates average differential temperature to resolvable spatial frequency. The targets are rotated by  $90^\circ$ , relative to the thermal imager detector array, and the measurement process is repeated for all previously measured frequencies.

This generates two resolution curves, one for each orientation of bar pattern. The 2-D MRT curve is found by calculating the geometric mean of the spatial frequencies between the two 1-D curves at each target contrast, as shown in Figure 8 [23]. Since the measurement of MRT correlates target differential temperatures to spatial frequency, the 2-D MRT curve separates the frequency-contrast space into regions where spatial frequencies are visible and not visible.

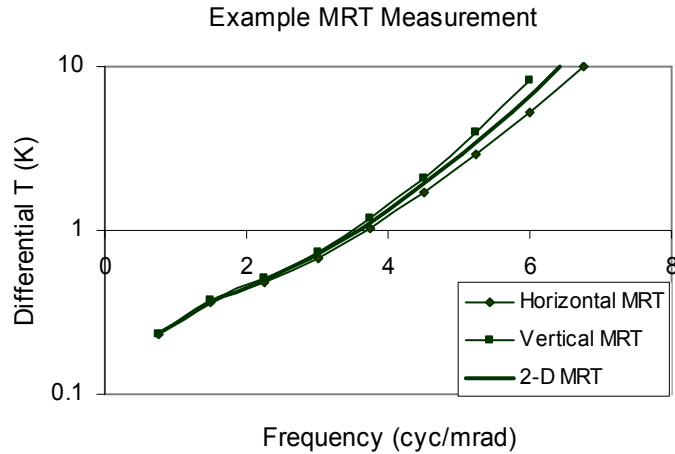


Figure 8. Example of two, 1-dimensional MRT's and the resultant 2-D MRT.

MRT measurements are extremely time consuming and completely subjective. With the advent of staring array sensors, questions have arisen about the reliability of MRT measurements and their meaningfulness [1, 14, 23, 24]. In particular, how far in spatial frequency, relative to the half-sample frequency, are the MRT measurements meaningful as a result of under-sampling? The next section introduces alternative measurements to the classical MRT measurement for use with under-sampled thermal imagers.

### 2.4.3.2 Alternatives to Classical MRT

To address the issue of under-sampled imagers, the U.S. Army Night Vision and Electronic Sensors Directorate (NVESD) proposes a calculation solution. This solution not only re-establishes the link between laboratory measurements and field performance, but also addresses the lack of repeatability in the MRT measurement. Equation (3) provides the NVTherm 2002 thermal imager model, which predicts system MRT. Given

that the 3-D noise, thermal imager MTF, and display parameters are measured, the MRT of the thermal imager is calculated. The additional benefit is that the calculation renders a characteristic curve useable for range prediction. This methodology preserves the model separability along the dimensions of the detector grid and also preserves the interpretation of linear shift invariant systems for thermal imagers.

Triangle orientation detection (TOD) is a measurement that (1) measures a constant threshold as a function of spatial frequency independent of the observers' internal decision criterion, (2) allows the reliability of the observers' responses to be statistically checked, and (3) still maintains a simple task for the observer. An observer is presented a series of equilateral triangles of different sizes and contrast levels. The observer then has to determine the direction the triangle is pointed, either up, down, left, or right. The thermal contrast for this measure is defined as the difference between the test pattern and background temperatures. The effective area of the triangle is defined as the square root of the area of the triangle, and the reciprocal of this measure is the frequency measure that may be used in the ACQUIRE model [25-28].

The psychometric function used to model the observer responses is a Weibull function of the form

$$P_{\alpha\beta\gamma\delta}(x) = (1 - \delta) - (1 - \gamma - \delta) \cdot 2^{-\left(\frac{x}{\alpha}\right)^\beta} \quad (9)[27]$$

where

x is the stimulus strength,

$\alpha$  is the stimulus strength threshold,

$\beta$  is a fit parameter for the steepness of the curve,

$\gamma$  is the guess rate (The guess rate for a 4-alternative forced choice experiment is 0.25),

$\delta$  is the probability that the observer accidentally hit the wrong button (usually set to 0.02).

This function presents the continuum of all responses from low probabilities to very high probabilities depending on the stimulus strength. The acceptable level of performance has been chosen by TNO human factors group to be the 75 percent correct level for the stimulus strength. This level is calculated using the previous parameters found in Equation (9) and takes the form of

$$\frac{\alpha_{75}}{\alpha} = \left[ -2 \log \left( \frac{0.25 - \delta}{1 - \gamma - \delta} \right) \right]^{\frac{1}{\beta}} \quad (10)[27]$$

The resolution-contrast space of a thermal imager can then be divided along the level of 75 percent correct responses. This space is then correlated to contrast and spatial frequency and is used in the same manner as MRT. The TOD methodology has been shown to predict thermal imager field performance. However, the NVESD MRT allows a measurement separable into two 1-D measurements, whereas the Fourier transform of the TOD methodology is not separable in either Cartesian or polar coordinates. The strength of this measurement methodology is a four-alternative forced choice perception experiment, which removes the observer subjectivity.

Germany's FGAN-FFO proposes a replacement measurement to resolve the inherent problem in measuring the MRT for insufficiently sampled imagers. Minimum temperature difference perceived (MTDP) addresses the problem of measuring the MRT of a thermal imager that is under-sampled. This measurement of thermal imager phase, or

the relative displacement between the scene and sensor, is very important. The MTDP technique uses much of the theory from the MRT test and the same targets, the four-bar pattern. However, the requirement to resolve all four bars is relaxed. A valid frequency contrast point can be made with the observer seeing as few as two bars for frequencies greater than the half-sample frequency of the sensor [28, 29]. This allows the MRT to extend above the half-sample frequency and more effectively allows the Johnson theory to better compensate for the fundamental limit occurring at the half-sample frequency. This methodology does not provide for linear shift-invariant modeling or measurement approach, as some output frequencies are not the same as the input frequencies. Also, the relaxation of the requirement to observe all four bars in the pattern allows the Johnson theory to give overly optimistic range performance predictions.

### 3 Sampling

The past 20 years have seen thermal imagers evolve from scanning imaging systems to staring array imaging systems. The ability to produce an array of infrared-sensitive detectors has greatly increased the sensitivity and the SNR of these thermal imagers. Unlike scanning systems, the detectors in a staring array integrate the image signal for a larger fraction of the sensor frame time. Because the thermal imager detector elements are large (30 to 50 $\mu\text{m}$ ) and sample the image, aliased components result in the output image if the input scene is not suitably band limited. Although design criteria addressing the effects of aliasing have been developed for TV-type imagers [30-32], the performance consequences of under-sampling or improper filtering have been characterized in a subjective form.

This chapter begins with a background section on the previous research performed in the area of under-sampled imagers. This background section reviews the historical design criteria developed by Schade, Kell, and others, and reviews the contributions provided for characterizing the performance impact on current thermal imagers. The background is followed by a section describing the design of a human perception experiment to study the effects of aliasing on human performance. A comparison to the historical experiments performed by NVESD and the conclusions are provided.

### 3.1 Background

A model of a sampled imaging system is illustrated in Figure 9. The input-output relationship for this system is given in the Fourier transform domain by

$$I(f) = \sum_{n=-\infty}^{n=\infty} O(f - n f_s) H(f - n f_s) P(f), \quad (11)$$

where  $f$  denotes spatial frequency, usually in cycles per milliradian;  $I(f)$  and  $O(f)$  are the Fourier transforms of the output image and object, respectively;  $H(f)$  is the transfer function associated with all pre-sample blurs, including effects of imaging system optics, scattering of the thermal radiation, and the size and shape of the imager detector elements; and  $P(f)$  is the transfer function associated with all post-sample blurs, including effects of the display and any electronic filters.

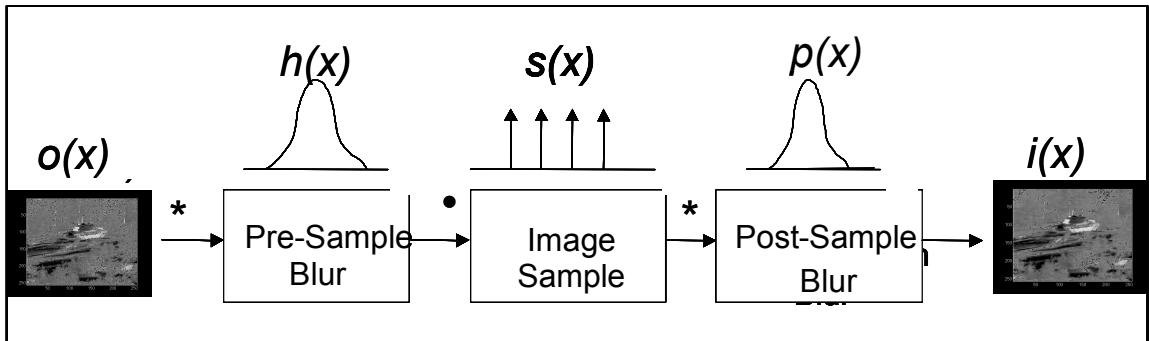


Figure 9. A simplified three-step sampled imaging system process in one dimension, where  $h(x)$  is comprised of atmospheric terms, optics, and detector blurs,  $s(x)$  represents the imager sample spacing, and  $p(x)$  is composed of all blurs occurring after sampling such as digital filters, and display blurs.

Equation (11) can be represented as the sum of two components to emphasize the effects of aliasing:

$$I(f) = O(f)H(f)P(f) + \sum_{n \neq 0} O(f - n f_s)H(f - n f_s)P(f). \quad (12)$$

The first term, referred to in this work as the *transfer response term*, is the only term that remains in the absence of any aliasing, i.e., when there is no sampling or when the sample frequency  $f_s$  is sufficiently high. The second term represents the aliased spatial frequency components. This latter term is generally referred to by members of the thermal imaging community as the *spurious response spectrum*.

Figure 10 illustrates an imaging system transfer response and aliased response for the case where the Fourier transform of the object contains higher spatial frequencies than the limiting pre-sample filter of the imager,  $H(f)$ . Note that through the adjustment of the sample frequency and the widths of  $H(f)$  and  $P(f)$ , the aliased component distribution changes in both magnitude and location along the spatial frequency axis.

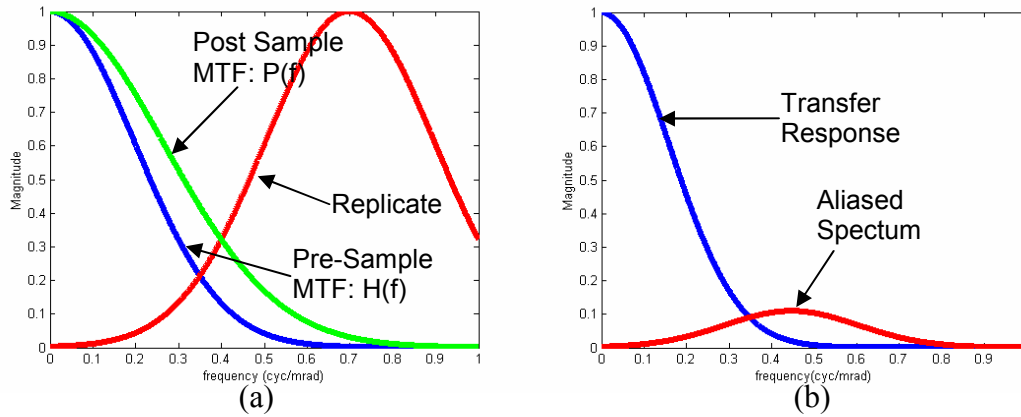


Figure 10. Notional plot of the sampled imager response function. (a) The pre-sample MTF  $H(f)$  is replicated at the sample frequency. The post-sample MTF  $P(f)$  filter both the baseband signal and the replicated signal. (b) The transfer response is the pre-sample MTF multiplied by the post-sample MTF. The pre-sample replicas are also filtered by the post-sample MTF and become the aliased spectrum.

### **3.1.1 Historical Treatment of Sampling**

Research conducted decades ago by the television industry provided design guidance regarding the widths of various system MTFs and the associated reduction of objectionable aliased components [30-32]. Although these guidelines focused on television technology, they provided some design guidance for modeling advanced thermal imagers. None of this guidance quantified the performance reduction associated with specific visual discrimination tasks and hence had limited applicability to the focus of target acquisition performance and this research.

#### **3.1.1.1 Kell Factor**

The Kell factor was developed in the early years of television, 1934, to quantify the number of resolvable lines on a cathode ray tube (CRT). Hence, the Kell factor addressed sampling that occurred only at the display. In addition to only quantifying the sampling effects at the display, the Kell factor was a spatial term, not a spatial frequency term. This factor accounted for the loss of limiting resolution in the direction of the raster sampling. The Kell factor related the number of resolvable lines,  $R_v$ , to the number of active raster lines,  $N_a$ , in a display as  $R_v = KN_a$ , where  $K$  was the Kell factor [33]. An extensive study was performed by Luxenburg and Kuehn [34], where the Kell factor possessed a range from 0.53 through 0.85. The Kell factor was not fixed for all displays and has recently been shown to have a high variability based upon image construction scan pattern [35].

### 3.1.1.2 Schade's Criteria

Schade developed his criteria to minimize aliasing to an acceptable level based on viewing sampled images. The transfer response term was related to the half-sample frequency of the imager. He determined that the product of these MTFs, the pre-sample and reconstruction MTFs, should be no more than 15 percent of the peak value at the half-sample frequency of the imager, as shown in Figure 11 [30]. As further guidance, Schade suggested that the input MTF and display MTF should be equal. Therefore, at the half-sample frequency, each of the MTFs; replica, baseband, and reconstruction, were no larger than 40 percent of the peak value, as shown in Figure 11.

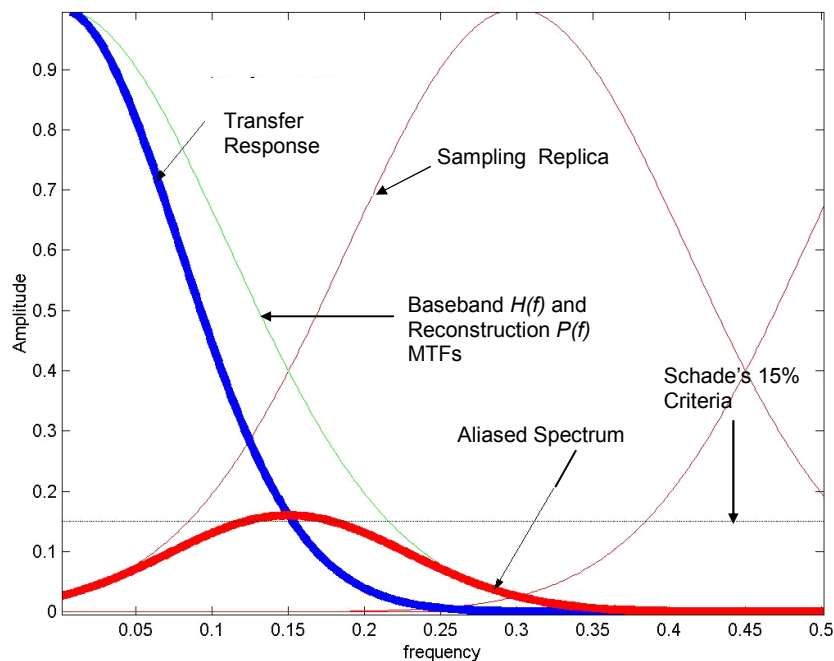


Figure 11. Graphical representation of Schade's sampled imager guidance.

The horizontal line in Figure 11 is the 15 percent requirement that Schade recommended. Therefore, the minimum half-sample frequency for this imager should be no less than 15 percent, as an example. Schade's criterion provided guidance on a maximum limit for aliasing with respect to the display. However, human CTF, distance from the display, or the number of eyes used in viewing are not considered. An assumption is made that the display would be placed at an optimum distance for the observer to minimize the high-frequency sampling effects through the filtering capabilities of the eye.

### **3.1.1.3 Legault Criteria**

Similar to Schade, Legault established a relationship between the transfer response MTF of an imaging system and the half-sample frequency. This criterion did not require the matching of the pre-sample MTF with the display or reconstruction MTF, and was therefore more relaxed than Schade's criteria. Legault stated that when integrating the transfer MTF, 95 percent of the MTF area was to be located at frequencies less than the imager half-sample frequency [31]. The application of this requirement to the transfer response MTF of Figure 11 is shown in Figure 12.

If the pre-sample and reconstruction MTFs are equal, as suggested by Schade's criteria, then Legault and Schade provide very similar design guidance. However, the Legault criterion does not require the pre-sample and reconstruction MTFs be equal and, therefore, provides less restrictive guidance.

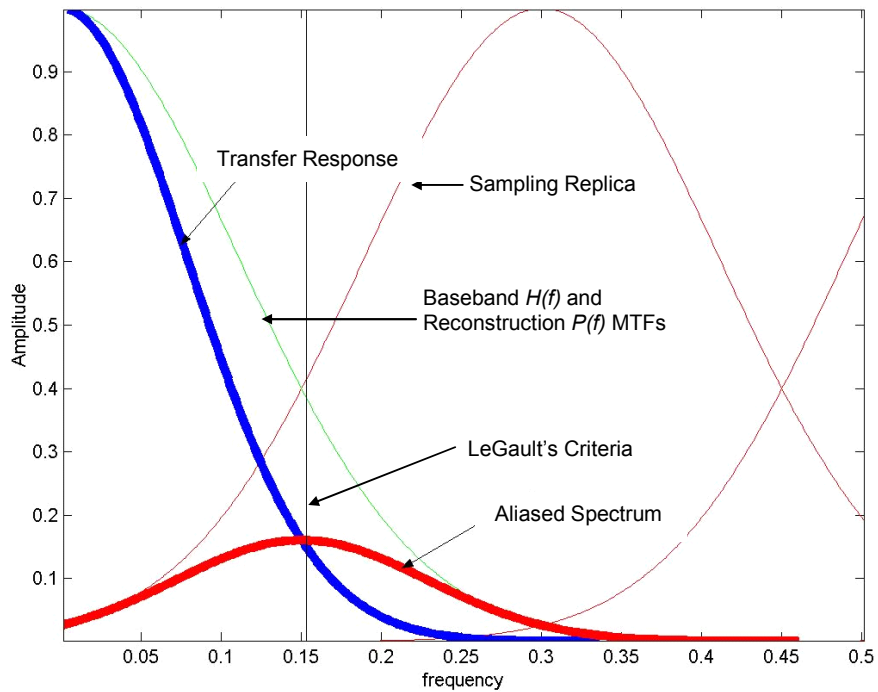


Figure 12. LeGault's design criteria as applied to the same imaging system shown in Figure 11.

### 3.1.1.4 Sequin Criteria

Sequin, while investigating interlacing in CCD devices, suggested that the maximum response frequency of a sensor system is the point where the aliased spectrum equals one-half of the transfer response [32]. The vertical line in Figure 13 denotes the spatial frequency that satisfies Sequin's criterion. This is more pessimistic than either Schade's or Legault's criteria. The Sequin frequency (the point where the spurious signal is half of the system transfer response) is generally specified as a percentage of the half-sample frequency.

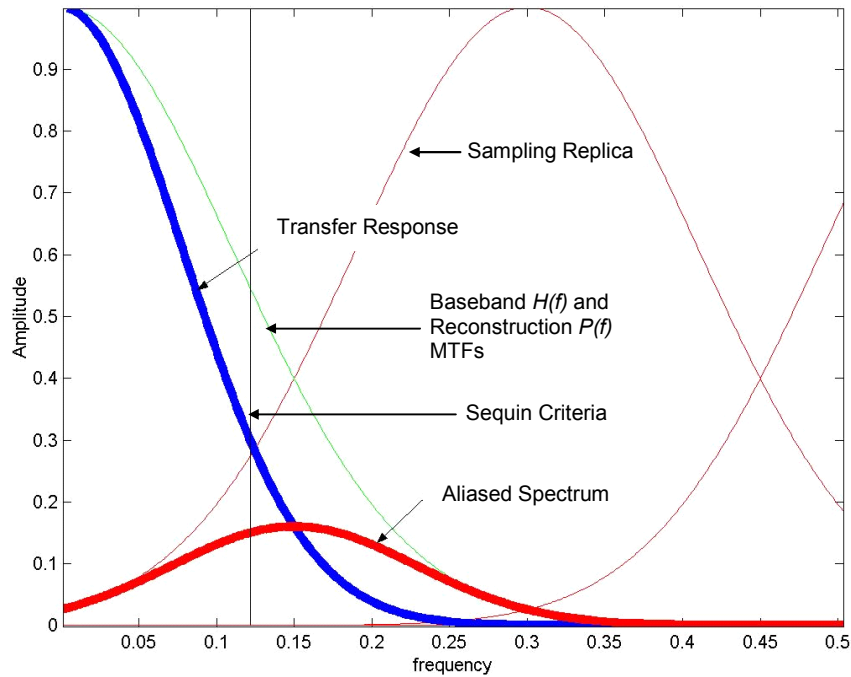


Figure 13. Sequin criteria applied to a sampled imaging system.

The historical design criteria of Schade and Legault only consider the physical display as part of the reconstruction or post-sample MTF. The assumption is that an observer would optimize the distance from the display in order to filter out such artifacts as the display raster. Given this assumption, the Schade, LeGault, and Sequin criteria only address the aliased spectrum that occurs at frequencies less than the half-sample frequency of the imaging system. Finally, these criteria are design guides and do not address quantitative performance reduction because the aliased spectrum exists in an imaging system.

### 3.1.2 Contemporary Treatment of Sampling

There is a large literature base on the characterization of the under-sampling effects of staring arrays [36-51]. For first- and second-generation thermal imagers, laboratory measurements, such as MRT, have been used to provide useful predictions of field performance through such models as ACQUIRE [15-18]. The relationship that ACQUIRE provides between laboratory measurements and field performance has been an overall success for visual discrimination tasks of thermal imagers. However, the corresponding relationship between laboratory measurement and field performance for staring array systems has discrepancies that have not been adequately investigated. Although laboratory measurements for staring arrays are available, there is limited field performance data on these same systems. The data available suggests a different laboratory-to-field relationship than that seen with first- and second-generation thermal imagers [36].

There are a number of theories on how the presence of aliased components affects human performance. One theory treated aliasing as fixed-pattern noise [38]. Other research, which includes the use of an eye model, shows that aliasing reduced the probability of finding targets; however, no general relationship was developed to describe the effects of these aliased components [39]. Through the use of this eye model, a general trend was shown that an increase in the amount of aliasing corresponds to a decrease in the probability of detection. There have been additional studies that suggest a change in the Johnson cycle criteria would compensate for the differences in staring and scanning thermal imager performance [40]. These studies experimentally showed that there is a greater difference between a staring thermal imager and a scanning thermal imager than a

change in the Johnson criteria could overcome. Sampled imagery has even been described using information density and efficiency, but this description has not been calibrated for human responses [41].

There were a number of experiments that intended to investigate the effects of under-sampling. These experiments accomplished their objective of demonstrating that there is a strong relationship between reduced recognition performance and under-sampling. One experiment by D'Agostino et al. [43] was designed to investigate the reductions in the recognition of vehicle images resulting from the consequences of under-sampling. This particular experiment studied the reduction in recognition rate as a function of changing the number of samples per detector angular subtense, or detector dwell, in a scanning thermal imager system. The investigation found that the 2-D sample density, as well as detector dwell, was a critical performance parameter. A second experiment, by Howe et al. [44], supported the results of D'Agostino. In this experiment, identification was studied as a function of samples per detector dwell. The results of Howe's second experiment showed that both sampling aperture<sup>3</sup> and sample spacing were critical factors in human performance.

It was found during previous NVESD experiments [45] that imager performance could be related to the ratio of integrated aliasing to integrated transfer response. Three metrics are proven useful in quantifying the aliased components: total integrated spurious response metric, defined by Equation (13), in-band spurious response metric, defined by Equation (14), and out-of-band spurious response metric, defined by Equation (15). If the various replicas of the pre-sample blur overlap, then the aliased signals in the overlapped

---

<sup>3</sup> Sampling aperture refers to the size of the detector element.

region are root-sum-squared before integration. It may be thought that Equation (13) effectively measures the capacity of an imaging system to produce aliased components.

$$SR_{Total} = \frac{\int_{-\infty}^{\infty} \left| \sum_{n \neq 0} H(f - n f_s) P(f) \right| df}{\int_{-\infty}^{\infty} |H(f) P(f)| df} \quad (13)$$

$$SR_{in-band} = \frac{\int_{-v/2}^{v/2} \left| \sum_{n \neq 0} H(f - n f_s) P(f) \right| df}{\int_{-\infty}^{\infty} |H(f) P(f)| df} \quad (14)$$

$$SR_{out-of-band} = SR_{Total} - SR_{in-band} \quad (15)$$

These three metric equations assume that the input scene or target possesses sufficient spectral width to be treated as a point source at the thermal imager entrance optics. This assumption is justified, considering that the further the range, the wider the target spectrum. Figure 14 shows an example of a vehicle at 1km, 2km, and 4km with its associated Fourier transform. The input scene may be treated as a point source, and more importantly, the NVESD metrics may be applied to all vehicles and a vehicle specific theory need not be developed.

Equations (14) and (15) show that the definitions of these metrics are based upon the location of the aliased spectrum to the half-sample frequency of the imaging system as illustrated in Figure 15. Aliasing that occurs at frequencies below the half-sample frequency is referred to as in-band aliasing. This location of aliasing appears as shifted edges in imagery; therefore, straight lines may appear as stair steps or have varying thickness. Aliasing that occurs at frequencies above the half-sample frequency is referred to as out-of-band aliasing. This location of aliasing appears as raster or pixel effects in imagery; therefore the imagery appears to have a mask placed over top of it in either 1-D

for raster pattern or 2-D for pixels. In the case of mid-band aliasing, aliased components appear both above and below the half-sample frequency. This location of the aliased components would therefore contain a mix of in-band effects and out-of-band effects.

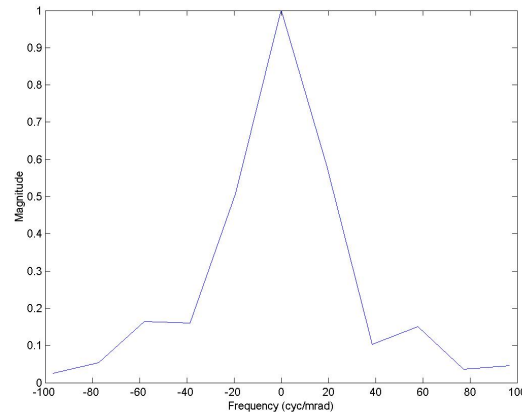
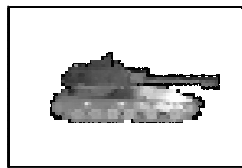
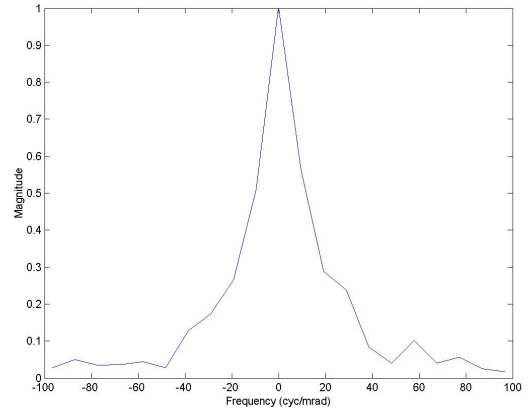
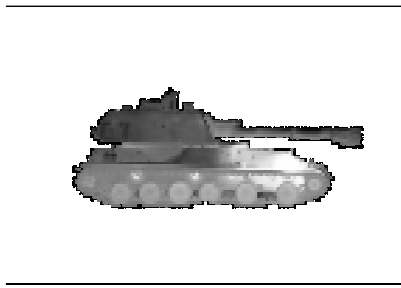
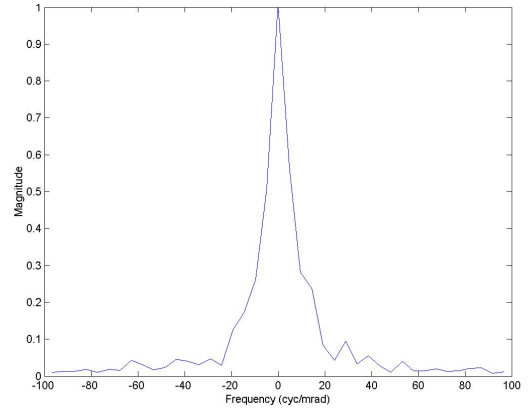
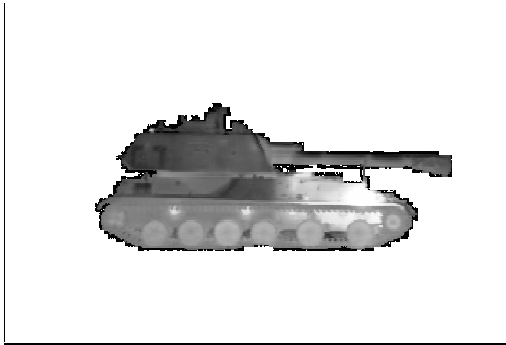


Figure 14. A 2S3 self-propelled artillery piece at three different tactical ranges with the corresponding spatial frequency spectrum.

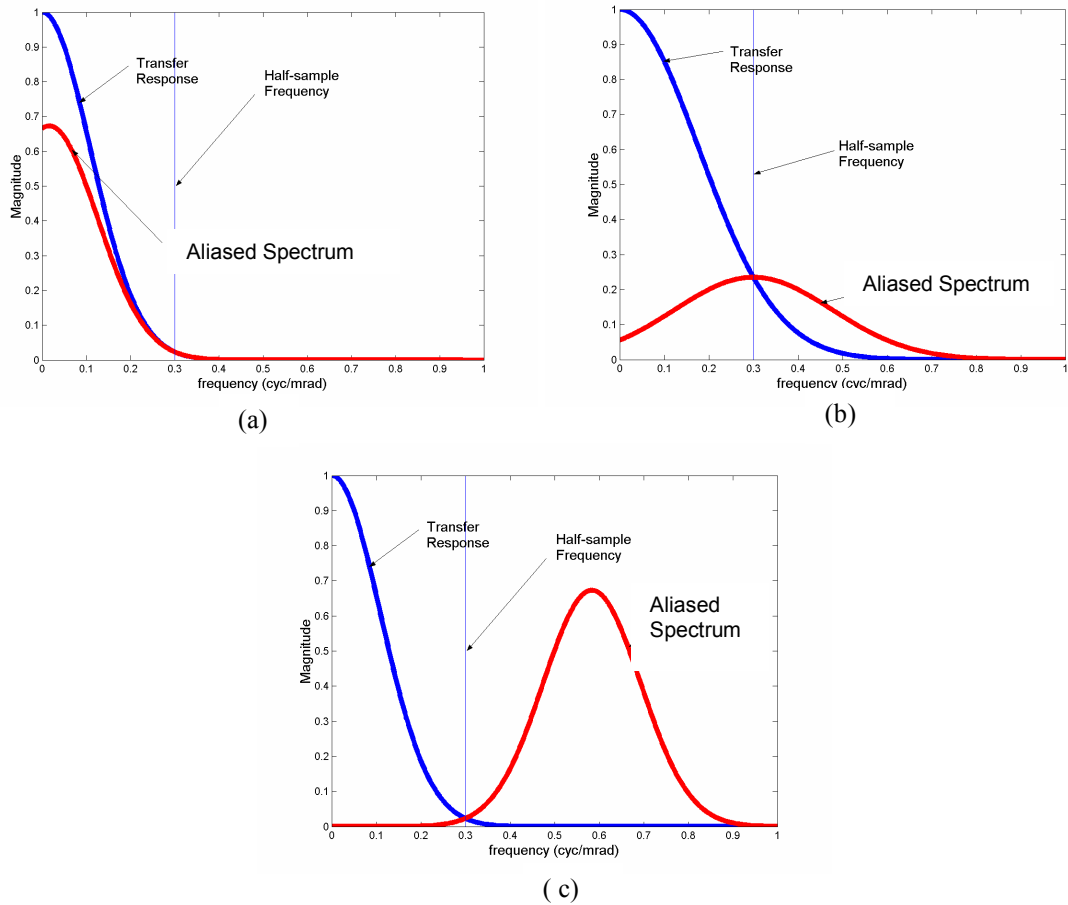


Figure 15. Graphical representation of spatial frequency location for aliased components: (a) in-band aliasing, (b) mid-band aliasing, and (c) out-of-band aliasing.

Previous NVESD experiments [46-48] quantified the relationship between the sampling artifacts generated by typical sampled thermal imagers and target recognition and identification performance. One experiment was a character recognition test [48] and the second was a target identification test [49]. On the basis of data from these tests, it was determined that the performance loss associated with sampling could be modeled as an increased system blur. The blur increase was characterized as a function of the total integrated spurious response metric for the recognition task and as a function of the out-of-band spurious response metric for the identification task. Overall, the literature

supports the use of the spurious response metrics (Equations (13) through (15)) to characterize under-sampled systems [48-51].

### **3.2 *Experimental Design***

In this research, experiments were developed to investigate the reduction on target identification performance by human observers based on the amounts of the total integrated spurious response metric allowed by the imaging system. These experiments were not based on real sensors but rather a controlled sampled thermal imager system, modeled in Figure 9. This imaging system cascaded a pre-sample blur, a sampling operation, and a post-sample or reconstruction blur. Emulating a real sensor, as previous research did, produced a single data point relating performance degradation to the level of aliasing as measured by Equations (13) through (15). The experiments I developed emulated 54 different thermal imager configurations. This allowed a refinement to the relationship between the spurious response metrics defined in Equation (13) through Equation (15) and human performance degradation. These experiments on the affects of under-sampling to human observer target identification performance answer the following questions: (i) What is the relationship between the quantity of total integrated spurious response metric and imager performance? and (ii) Does the spatial frequency location of the spurious spectrum change the relationship found in question (i)? The levels of the total integrated spurious response metric, Equation (13), at each of the spatial frequency locations were controlled at 0, 0.2, 0.3, and 0.4. Having noted a trend in the previous experiments between the out-of-band aliasing components and observer

relative performance, an additional experiment was later added to achieve 0.5 and 0.7 levels of total integrated spurious response metric with out-of-band aliased components.

### 3.2.1 Image Set and Preparation

A set of 12 tracked military vehicles used for model development at NVESD are shown in Figure 16. This set consists of self-propelled artillery pieces, armored personnel carriers (APCs), and tanks. This image set provides a historical database to compare the observer results of the sampling experiments with the observer results of previous human performance experiments.

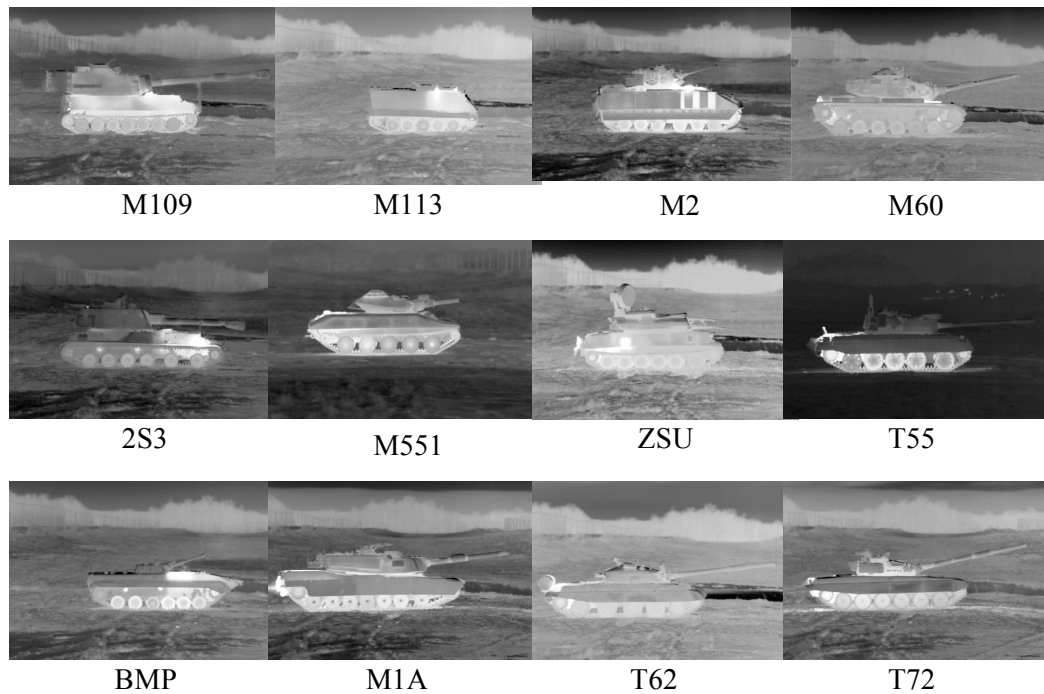


Figure 16. Target set of images for the visual identification task.

Short-range, high-resolution thermal images were taken of all the target vehicles at 12 different aspects to the imager. With this image set, human observer identification experiments were conducted. The thermal imager was an Agema Thermovision 1000 with a 20°x13° field of view (FOV) and an instantaneous FOV (IFOV) of 0.6 mrad for each detector sample. The focal plane consisted of several mercury-cadmium-telluride (MCT) sprite detectors that were sensitive to 8-12 μm radiation and output 12-bit imagery.

The images in each experimental cell<sup>4</sup> were processed with a fixed level of blur and three levels of the total integrated spurious response metric as quantified by Equation (13). The aliasing was achieved by using a three-step process of applying a pre-sample blur function, down-sampling, and applying a post-sample blur function, as shown in Figure 9. Each blur function took the form of

$$f(x) = \text{sinc}\left(\frac{x}{b}\right) \bullet \exp\left[-\pi\left(\frac{x}{4b}\right)^2\right], \quad (16)$$

where  $b$  was a width parameter in pixels for the pre-sample and post-sample blur function sizes. The  $b$  parameter for each experimental cell and the down-sample frequency are shown in Table 2. This blur function more closely replicated an ideal filter with the benefit of reducing the ringing associated with an ideal filter because of the rapid decay of the Gaussian envelope function. The calculation of the aliasing amounts assumed that the input scenes were point sources and therefore represented the emulated thermal imagers capacity for aliasing. The point source assumption was valid for this set of

---

<sup>4</sup> An experimental cell consists of a sub-set of images. All the images of an experimental cell are processed with a common methodology. This methodology is changed in a known fashion between the cells of an experiment.

images since the Fourier transform of the vehicle images were larger than the most restrictive pre-sample MTF of the emulated thermal imagers.

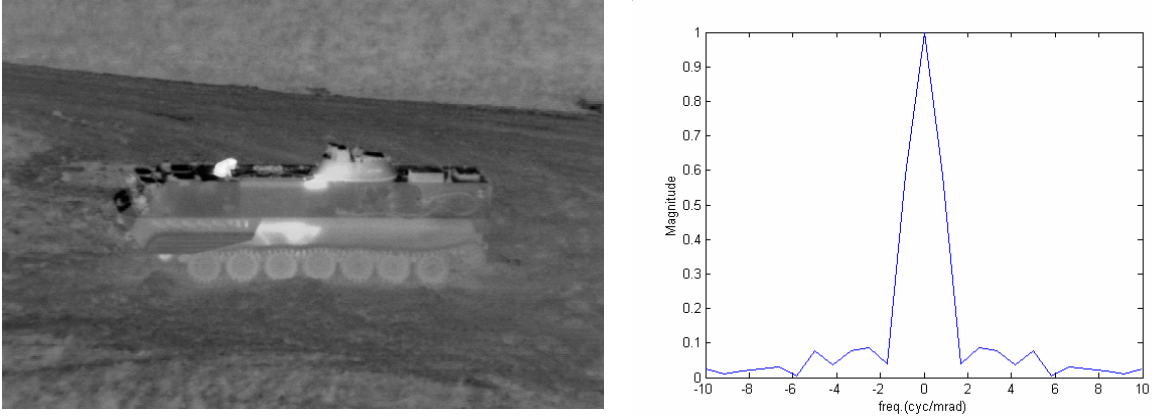


Figure 17. Original sized image used as a scene input for the controlled thermal imagers and the magnitude of its associated Fourier transform.

To simulate in-band aliasing, shown in Figure 15(a), the blur associated with reconstruction (post-sample) was set to the same values as the non-sampled baseline imagery. The width of the pre-sampled image blur was then adjusted to provide total integrated spurious response metric values of 0.2, 0.3, and 0.4, as shown in Table 2. These metric values were chosen as being representative of a typical thermal imager. To simulate the out-of-band aliasing spatial frequency location, the pre-sampled image blur size was set to the same specific values as the reconstruction blur of the in-band experiment. The reconstruction blur was adjusted to provide the previously mentioned total integrated spurious response metric values, 0.2, 0.3, and 0.4. Mid-band aliasing required both pre-sample and post sample blur sizes to be equal.

Table 2. Blurs and downsamples to achieve the desired levels of spurious response for all locations. Each cell lists the pre-sample blur width, the downsample spacing, and the post-sample blur width in that order.

Spurious Response	Blur Width			Blur Width			Blur Width			Blur Width			Blur Width			Blur Width		
	In	Out	Mid	In	Out	Mid	In	Out	Mid	In	Out	Mid	In	Out	Mid	In	Out	Mid
0	0 1 5	5 1 0	5 1 5	0 1 10	10 1 0	10 1 10	0 1 15	15 1 0	15 1 15	0 1 20	20 1 0	20 1 20	0 1 25	25 1 0	25 1 25	0 1 30	30 1 0	30 1 30
0.2	3.2 4 5	5 4 3.2	3.8 4 3.8	6.4 8 10	10 8 6.5	7.6 8 7.6	9.6 12 15	15 12 9.5	11.3 12 11.3	12.8 16 20	20 16 12.7	15.2 16 15.2	16 20 25	25 20 16	19 20 19	20.2 25 30	30 25 20	23.5 25 23.5
0.3	2.9 4 5	5 4 2.9	3.55 4 3.55	5.8 8 10	10 8 5.9	7.1 8 7.1	8.9 12 15	15 12 8.7	10.6 12 10.6	11.6 16 20	20 16 11.7	14.2 16 14.2	14.6 20 25	25 20 14.6	17.6 20 17.6	18.5 25 30	30 25 18.5	22.1 25 22.1
0.4	2.7 4 5	5 4 2.75	3.35 4 3.35	5.4 8 10	10 8 5.45	6.7 8 6.7	8.2 12 15	15 12 8.2	10.1 12 10.1	10.9 16 20	20 16 10.9	13.3 16 13.3	13.6 20 25	25 20 13.65	16.7 20 16.7	17.2 25 30	30 25 17.1	20.8 25 20.8

Once the images were prepared with the various values of the total integrated spurious response metric, the experimental cells were randomized within each experiment. Each experiment tested the spectral location of the aliased spectrum. By randomizing the cells within each experiment, Observer learning effects were minimized.

### **3.2.2 Human Visual Perception Experiments**

To quantify human performance degradation because of under-sampling, several human perception experiments were conducted. The human perception experiments were designed to measure the additional reduction in human performance which could not be accounted for by additional blur. This section describes the observer training and the distribution of the images in the creation of a balanced psychophysical experiment.

Twenty-three observers were trained on the identification task for the vehicle set shown in Figure 16. The observers were given a pre-training test using the software package Recognition of Combat Vehicles (ROC-V). The pre-training test consisted of 48 images selected from the total vehicle set of 12 vehicles used in the experiment and chosen from 12 different aspects. The observers were then directed to utilize the timed test utilities and the image library contained in ROC-V to study the infrared signatures of the vehicles. This phase of the training was self-paced. When the observer completed the ROC-V training package, a random 48-image post-training test was administered on the computer and the observer was required to score a 95 percent, correctly identifying at least 46 out of the 48 images, to be considered trained on the vehicle set. If the observer failed the post-training test, an instructor assisted the observer in learning the vehicle set until he was able to achieve the required test score. This ensured that each of the

observers could perform the identification task on this set of vehicle images without simulated thermal imager blurs or sampling effects.

The display screens were calibrated for a maximum pixel brightness of  $70 \text{ cd/m}^2$  and a minimum pixel brightness of  $0.5 \text{ cd/m}^2$ . This allowed the pupil size of the observers to be predicted and their eye MTF to be modeled using the Overington eye model. The observers were then sequentially shown all 24 images in a test cell. Each experiment testing the location of the aliased spectrum consisted of 576 images and required about an hour and a half to complete. The observers were allowed as many breaks as they desired during each test and were encouraged to take a break half way through each test. The test area was dimmed to minimize glare on the displays from surrounding light sources.

In order to not process all 144 images (12 targets at 12 aspects) with six different blurs, the image set was evenly distributed across the six experimental cells, shown in Table 2. Each cell possessed two images of each aspect and two images of each target. This methodology helped control the length of each perception experiment while maintaining a balance on the number of aspects and vehicles observed in each cell and allowing each cell to be of a similar difficulty. The observers were aware that they were being tested on a subset of imagery in each experimental cell, but unaware of the method used to select the subset. The 24 experimental cells were randomized in an attempt to minimize learning effects by the observers during the experiment.

### **3.2.3 Experimental Results**

The results of the experiments are shown in Figure 18. Experiment A showed in-band aliased imagery, B and D showed out-of-band aliased imagery, and experiment C showed

mid-band aliased imagery. Of the 23 observers, 13 participated in experiments A, B, and C. The remaining ten participated in experiment D. As shown in Figure 18, for experiments A and C, the in-band and mid-band aliasing of the levels tested had little to no effect on the target identification task. However, experiments B and D showed that out-of-band aliasing had a significant impact on the target identification performance. These results were consistent with previous experiments [47,48]. The larger the value of the total spurious response metric for out-of-band aliasing the more detrimental the sampling-generated artifacts were on target identification performance (at least in the comparison of these limited cases). For experiments B and D, the performance at the 20-pixel blur level for the 0.4  $SR_{Total}$  performance curve seems to be better than for the 0.5  $SR_{Total}$  performance curve, as shown in Figure 18. The average probability of identification for the 0.4  $SR_{Total}$  curve at this point was 0.208 with a standard deviation of 0.155. The average probability of identification for the 0.5  $SR_{Total}$  curve at this point was 0.295 with a standard deviation of 0.117.

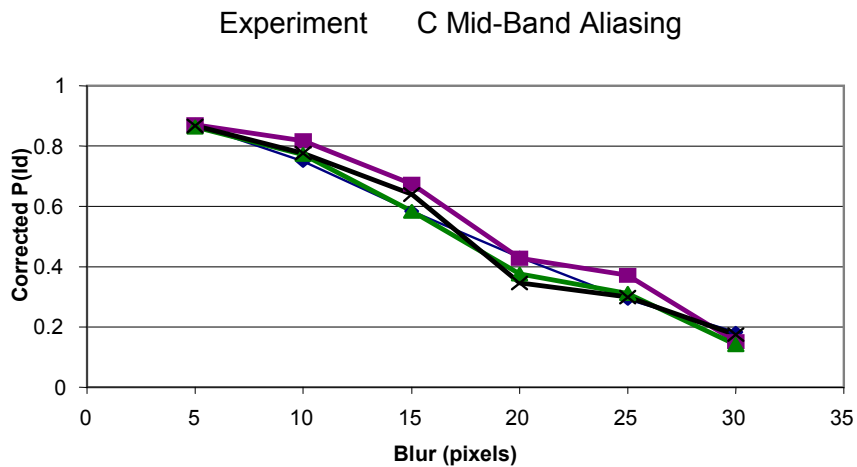
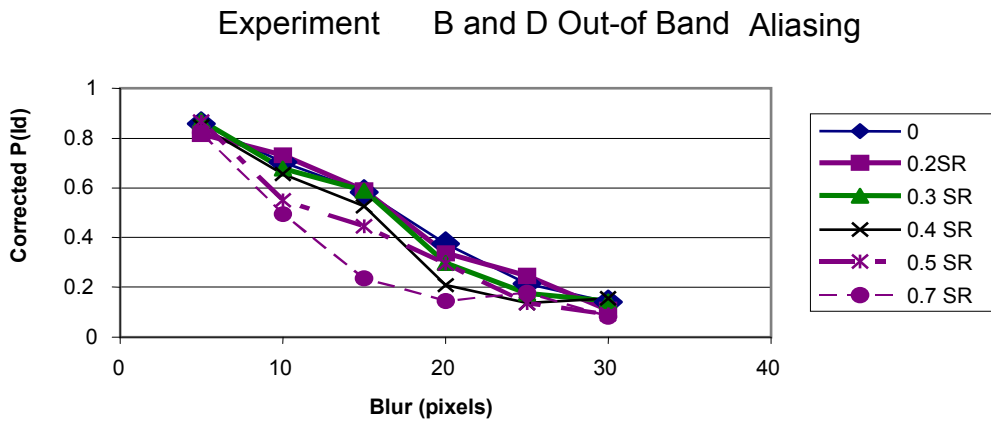
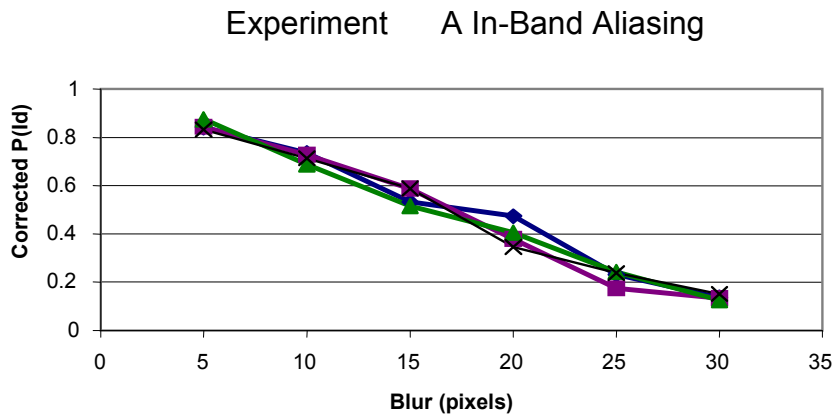


Figure 18. Results of the perception experiments to test the impact of aliasing allowed spatial frequency location on imager performance reduction.

A simple curve was fitted to the baseline curve, showing the results of the imagery without sampling effects, of each experiment. This curve related blur to observer performance and is shown in Figure 18 labeled as the 0 curve in each experiment. The requirements for a “simple” curve were that the blur values had to occur dependent on one variable, and the curve also had to roughly represent the observer performance curve for the aliased imagery results. These “simple” curves allowed the observer performance on the imagery possessing aliased components to be modeled with a performance curve that described the baseline performance and allowed the comparison between the blur values that described both curves. The ratio of the blur values was then plotted versus the two spurious response metrics. The results, shown in Figure 18, suggest that in-band and mid-band aliasing have little to no impact on the perception task. The out-of-band spurious response metric, Equation (15), was used to quantify the amount of aliasing, as was the total integrated spurious response metric, Equation (13). A straight line was fitted to the data, as shown in Figure 19, to predict the amount of system MTF contraction necessary to account for the performance degradation because of the aliased frequencies. This MTF contraction or squeeze methodology is explained in depth in [47].

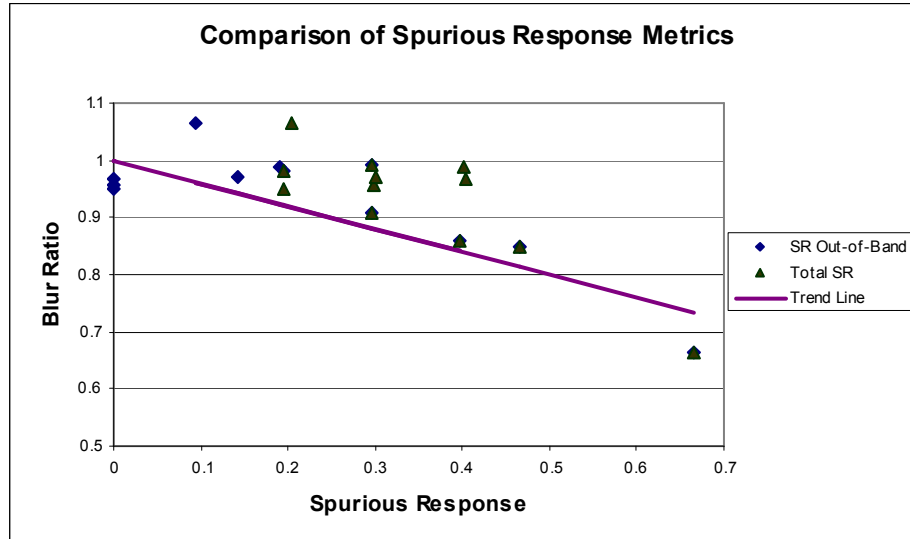


Figure 19. Computed spurious response metrics using both the total integrated metric Equation (13), and the out-of-band metric Equation (15).

A straight line was fitted to the out-of-band spurious response metric and the MTF contraction. The relationship was found to be

$$Ratio = 1 - 0.4(SR_{OOB}), \quad (17)$$

where  $SR_{oob}$  is the out-of-band spurious response metric defined in Equation (15). The curve defined in Equation (17) fit experiments A, B, C, D well with a correlation coefficient of 0.66, as shown in Figure 19. This ratio models the performance degradation observed for these specific experiments. The experiments determined that the spatial frequency location of the aliased components is a major factor on imager performance.

### 3.3 Sampling Discussion

To account for the performance degradation resulting from sampling effects, the imaging system is modeled as a non-sampled system. The resulting system MTF is then

contracted by the factor found in Equation (17) related to the amount of out-of-band aliasing. This factor is much less severe than the original factor reported by Vollmerhausen and Driggers [46]. The system MTF is a factor in calculating the system MRT curve, shown in Figure 3(b). A contraction of the system MTF causes the MRT curve to move primarily to the left, which means that the task requires more contrast to see higher frequencies. For a given contrast, there are fewer resolvable cycles available to the observer to complete the visual task. This impact results in lower probabilities of performance. All that is required to predict the target acquisition performance of a well-sampled imaging system are the MTFs of the system and the human CTF. The target acquisition performance of an under-sampled system requires the system MTFs and human CTF but also the amount of the out-of-band spurious response metric in order to impose the additional penalty for the masking effects.

## 4 Multiband Imaging

Single “color” broad waveband thermal imagers have been in use for many decades. With current manufacturing techniques, it is now possible to place several layers of detectors on a common focal plane array substrate. This allows thermal imagers to capture different spectral wavebands while the individual detectors are registered in space. Previous research [52-56] in the hyperspectral and multispectral imaging communities shows an advantage in target detection by using multiple wavebands through image differencing and other algorithms. A major disadvantage of these multiple wavelength focal plane arrays is their substantially higher cost. Also, there has been no guidance provided as to which spectral wavebands allow for the greatest advantage in clutter suppression or target enhancement for high-level visual tasks such as recognition or identification. Multi-waveband devices are successfully employed on aircraft missile warning systems. However, this application of missile detection differs significantly from the detection, recognition, or identification of tactical military vehicles in a thermally cluttered environment. The discrimination of military vehicles may be a very low contrast task, depending on the operational history of the vehicle at the time it is observed, whereas the missile detection application usually has the missile silhouetted against a cold background. This research provides a technique for determining which spectral wavebands and bandwidths are most beneficial for target detection, recognition, and identification.

Hyperspectral imagers (HSI) have been used in the past to show the advantages multiple wavelengths provide in reducing background clutter. HSI devices are hampered by low SNRs because of the narrow spectral extent of each image and the large number

of images per scene they collect (typically hundreds of images at various wavelengths). Multiple waveband devices or multispectral imagers (MSI) allow for higher SNRs, and, by their nature, collect fewer images per scene than HSI devices.

In August 2001, I planned and executed a data collection to obtain high signal-to-noise ratio (SNR), high-resolution multiwaveband imagery of both military vehicles and natural backgrounds. All vehicles, backgrounds, and blackbody reference sources were placed at the same range. The blackbody reference sources allowed for radiometric correction of the imagery. The collected images were then segmented to isolate the military vehicle targets and backgrounds of interest. After isolating the subject matter portions of the images, correlation coefficients were calculated between the waveband images of a common target to assess the spectral information differences contained in the radiometric images. This research establishes a methodology for collecting radiometric images outside of a laboratory environment, utilizes a meaningful information metric for the comparison of spectral images, and bounds the uncertainty effects of dead pixels and thermal imager noise to the information metric.

This chapter begins with a background section overviewing the historical research on hyperspectral and multispectral imaging, outlines a brief description of principal component analysis (PCA), and concludes with a mathematical description of photons leaving a source and traveling a distance through the atmosphere and falling on a thermal imager detector. The background is followed by an overview of the data collection, a description of the sensor used to collect the imagery, and an analysis of the errors introduced into the comparison metric because of dead pixels and thermal imager noise.

The source temperature conversion and correlation analysis of the data is provided, followed by a discussion of the results.

## **4.1 Background**

A definition of HSIs [57] are imagers “which produce, at a minimum, hundreds of spectrally narrow images.” Ironically, this large number of images is both a strength and a weakness for these devices. The strength is that the spectral images are sufficiently narrow, 3–10 nm, so that quantities like material spectral emissivity may be assumed constant over the spectral extent, while the large number of images provides many combinations of fused imagery. This makes the HSI well suited as a research and development tool to identify specific spectra of interest in a given scenario. Conversely, the large number of images ensures that an exhaustive search of all combinations of spectra requires significant effort, while the narrow spectra results in low SNRs. An HSI is poorly suited as a tactical sensor. Multiple waveband devices or multispectral imagers (MSI) allow for higher SNRs and, by their nature, collect fewer images per scene than HSI devices. MSIs are able to exploit the spectral differences in materials and provide high SNRs to complete visual discrimination tasks. If the ideal waveband combination was known for vehicle recognition and identification, an MSI imager could be manufactured to improve human performance on the battlefield.

### **4.1.1 Historical Research**

There have been research efforts in the past to exploit the distinctions in spectral characteristics of natural and man-made targets. Preliminary modeling performed by

Cederquist et al. [52] suggested that vehicle paint compositions possessed a sufficient spectral difference from natural backgrounds to allow for clutter or background suppression. Several data collections were performed, Eisman in 1993 [53] and also Schaffer and Johnson from 1993 to 1995 [54], with military vehicles in natural backgrounds. A major result of their research was the finding of a pair of wavebands in the LWIR spectrum that correlated natural sources very well (correlation coefficients in excess of 0.999) and possessed lower correlations for man-made objects, such as painted flat panels and vehicles. Stocker, Schwarz, Evans, and Lucey [55,56,58] subsequently verified these findings. The correlation coefficient is a statistical measure that quantifies the linear relationship between two sets of data with values ranging from  $-1$  to  $1$ . In the research performed by Eisman, Schaffer, Stocker et al., the data sets were images of the same scene in different spectral wavebands.

In 1997, Schwartz and his collaborators [56] found that averaging several adjacent spectral scenes from an HSI sensor did not significantly diminish the performance of these combined HSI images. Such findings support the notion of a multi-waveband sensor with higher SNR while the images preserve the desirable spectral discrimination capabilities found in HSI.

Scribner et al. [59,60] were among the first to attempt to quantify the amount of information dissimilarity between wavebands by performing correlation analysis on whole scene images. These images were collected with the ERIM M7 sensor. The ERIM sensor was composed of 16 wavebands ranging from  $0.36 - 12.11 \mu\text{m}$ . The sensor possessed one broad band midwave infrared (MWIR) band and two longwave infrared (LWIR) bands. The results of their correlation analysis showed that the visible bands had

negative correlation coefficients with the LWIR bands. The visible images contained complementary information to the LWIR wavebands. The visible bands had correlation coefficients less than 0.30 with the MWIR band. The correlation coefficient between the MWIR and the LWIR bands was 0.59. Their analysis showed significant information differences between the visible spectrum and the broad band thermal wavebands. Information differences also existed between the MWIR and LWIR spectra. These correlations were performed on whole scenes that contained both man-made objects and natural backgrounds. There was no attempt to determine the cause of the information differences (i.e., whether the differences were caused solely by backgrounds, man-made structures, or a combination of both). Also, the imagery was not radiometrically corrected, meaning that environmental effects such as path radiance may have provided some of the correlation effects.

All the previous data collections [52-56,58-60] had sensors based in towers or aircraft. The amount of atmosphere imaged through was less than a similar path length in a surface-to-surface application. Also, the focus of these data collections was target detection. For example, could a sufficient amount of clutter rejection be obtained to enhance the detection of a target? Another problem with the data collection methods was radiometric correction. If radiometric correction was attempted, the reference sources were located a few feet from the sensor. This location of a reference source allowed image gray scales to be converted to a radiometric quantity. However, sources located this close to the imager allowed for only the calibration to apparent radiometric quantities. To compensate for such confounds as path radiance and atmospheric

transmission, a model was needed to predict the path radiance given environmental data such as the U.S. Air Force MODTRAN model.

Developing a measurement methodology that provides for resolved reference sources, with the capability of compensating for the path radiance and quantifying the information differences between isolated vehicles and isolated backgrounds, would be a valuable tool for the infrared imaging community.

#### **4.1.2 Principal Components Analysis (PCA)**

The large amount of information from an HSI prevents an exhaustive search for the ideal waveband combination to be used in particular situations. Research is being conducted to determine ideal waveband combinations for the detection task, and several statistical techniques are used to reduce the HSI dimensionality and find the necessary waveband combinations [56,61,62]. One of these statistical techniques is called principal component analysis (PCA). This technique takes a highly dimensional space, such as a hyperspectral image cube, and is capable of reducing the dimensionality and defining a subspace that contains the information related to detecting a target. Each hyperspectral image cube can be cast as a set of image vectors.

$$A = [V_1, V_2, V_3, \dots, V_k] \quad (18)$$

where  $V_1$  through  $V_k$  are the hyperspectral images as vectors. The covariance matrix then becomes

$$C = A A^t. \quad (19)$$

A basis may be formed for the covariance matrix  $C$  by using the Gram-Schmidt orthogonalization procedure. This procedure states that the first vector of the covariance

matrix is the first basis vector of the space. The second basis vector is formed by calculating the unique information that exists in the second vector but not the first vector. This procedure is continued until all basis vectors are found that describe the space. Mathematically, this process is represented as

$$\begin{aligned} b_1 &= V_1 \\ b_2 &= (1 - \rho_{12}^2)^{-1/2} [V_2 - \rho_{12} V_1] \end{aligned} \quad (20)$$

for the first two basis vectors, where  $\rho_{12}$  is the correlation coefficient between vectors  $V_1$  and  $V_2$  [63]. Once the basis is found, the information exists to determine which image vectors contain the most unique information to enhance target discrimination and which image vectors suppress background discrimination. This dimensionality reduction technique shows that the correlation coefficient between spectral images is already used as an information metric to ensure linear independence between image cube basis vectors in the PCA technique.

#### **4.1.3 Mathematical Description of Imaging Process**

MSIs such as NASA's Thermal Infrared Multispectral Scanner (TIMS) sensor, DARPA's Multi-Spectral Infrared Camera (MUSIC) sensor, and the ERIM M-7 sensor have been used on a variety of data collections and have shown the capability to detect low contrast targets. The task of imaging through the atmosphere may be represented by the illustration in Figure 20.

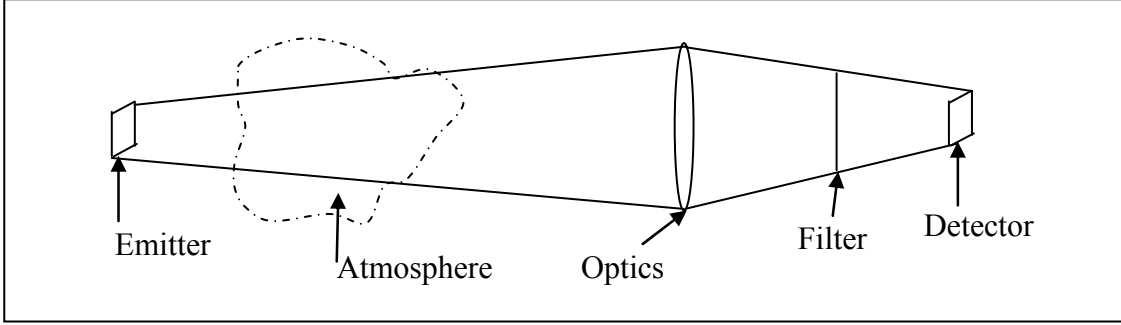


Figure 20. Graphical representation of radiation path from emitter to detector for a spectrally filtered thermal imager.

The path of a photon from the emitter to the thermal imager detector is shown in Figure 20. The equation modeling the voltage out of the detector due to the flux from the emitter is

Gray Levels =

$$K \int_{\lambda_1}^{\lambda_2} \frac{\varepsilon(\lambda)M_{emitter}(\lambda, T) + \rho(\lambda)M_{ambient}(\lambda, T)}{\pi} A_{detector} \Omega_{optics} \tau_{atmosphere}(\lambda) \tau_{filter}(\lambda) \tau_{optics}(\lambda) \mathfrak{R}(\lambda) d\lambda \quad (21)$$

where

$\lambda$  is the wavelength of radiation ( $\mu\text{m}$ ),

$\varepsilon$  is the target emissivity (unitless),

$M_{emitter}$  is the spectral radiant emittance from the target ( $\text{W}/\text{cm}^2\text{-}\mu\text{m}$ ),

$\rho$  is the spectral reflectance of the target (unitless),

$M_{ambient}$  is the reflected spectral irradiance from the environment ( $\text{W}/\text{cm}^2\text{-}\mu\text{m}$ ),

$A$  is the area of the detector ( $\text{cm}^2$ ),

$\Omega$  is the solid angle subtended from the emitter to the optics (mrad),

$\tau_{atmosphere}$  is the spectral transmission through the atmosphere (unitless),

$\tau_{filter}$  is the spectral transmission through the filter (unitless),

$\tau_{\text{optics}}$  is the spectral transmission through the collection optics (unitless),  
 $\mathfrak{R}$  is the detector spectral responsivity (V/W), and  
K converts volts to gray shade values.

As may be seen in the integral in Equation (21), the power a detector receives from a Lambertian target has two components,  $M_{\text{emitter}}$  and  $M_{\text{ambient}}$ . The  $M_{\text{emitter}}$  term represents the power emitted by the target, while the  $M_{\text{ambient}}$  term represents the power reflected by the target. Both of these power terms propagate through the atmosphere, which attenuates the power received by the detector. Previous field research did not directly account for the spectral transmission through the atmosphere in a rigorous fashion.

## **4.2 Data Collection**

The goal of the data collection was to obtain images of military vehicles and natural backgrounds that could be radiometrically corrected and compared to assess the information differences between the different waveband images. This section describes the methodology used to obtain temperature conversion information from the field test, outlines the field test objectives and methods, and concludes with a description of the sensor that collected the imagery.

### **4.2.1 Temperature Calibration of Imagery**

Placing calibration blackbodies at the range of the vehicles allowed the spectral characteristics of the atmosphere, collection optics, spectral filters, and detectors to be taken into account for radiometric correction. Equation (21) contains the emissive and

reflective characteristics of the target. A similar equation can be written where  $\epsilon=1$  for blackbody sources. This equation relates equivalent blackbody source temperature to gray levels, thereby allowing for the calibration of the gray levels at the sensor to source exitance. For the blackbody case, the exitance was identical to the source emittance. This calibration method was similar to the mapping of sensor counts to radiometric temperature as performed by a laboratory system intensity transfer function (SITF). The difference here was that the calibration curve included all components of the optical path to the detector, even the atmospheric path. The fielded blackbodies were imaged every hour to provide temperature reference images (shown in Figure 21 is an example reference image). The minimum number of non-edge pixels was nine on the +15°C (white) source, while the ambient and -5°C (black) sources both contained approximately 50 pixels each.

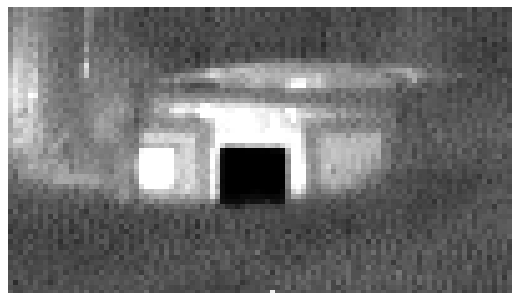


Figure 21. Temperature reference image of the three fielded blackbodies.

The reference images were used to generate calibration curves for each waveband at every hour of the field collection, shown in Figure 22. Since there were three blackbodies, a second-order polynomial was fitted to the calibration data. This curve fit

was then used to map sensor gray levels back into radiometric equivalent blackbody source temperatures.

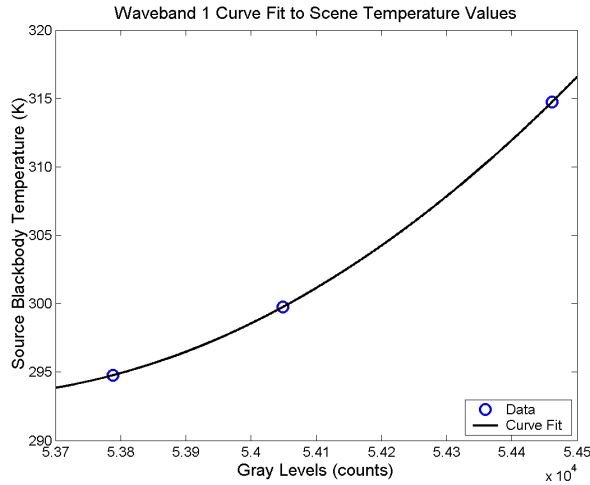


Figure 22. Example calibration curve for the first filter.

With this method of temperature correction, the majority of the pixels fell within the limits of the calibration blackbodies, as shown in Figure 23. By bounding the scene content with the calibration sources, the entire scene could be converted to source temperatures by interpolating between the calibration points. No extrapolation of the curve was needed outside the blackbody temperatures. For this example, the minimum blackbody temperature was 296.5K and the maximum blackbody temperature was 316.5K.

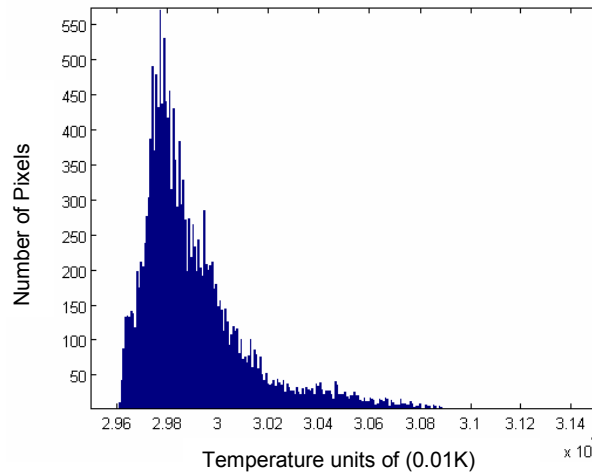


Figure 23. Histogram of image pixels after converting to radiometric equivalent blackbody source temperatures.

#### 4.2.2 Field Test

The goals of the field test were to obtain imagery that allowed for the isolation of targets from the natural backgrounds and to obtain imagery capable of being radiometrically corrected. Achieving these goals allowed for quality multiband imaging analysis. The data collection spanned the diurnal cycle and three states of vehicle operation: quiescent (cold), idled, and exercised. A cold vehicle is when the vehicle is sitting without its engine operating, an idled vehicle has its engine on but the vehicle is not driven, and an exercised vehicle has its engine running and is either currently driving or has recently been driven.

The site of the test was a military facility in the United States during late summer. The test range provided an area large enough to place six vehicles simultaneously at the same range without obscuration. To obtain imagery that allowed for the easy isolation of

targets and backgrounds, the vehicles were placed in a grass field and imaged from a slight elevation, shown in Figure 24. This location provided a bland grass background that was removed during segmentation. Segmentation was the process where all non-target pixels were set to zero.

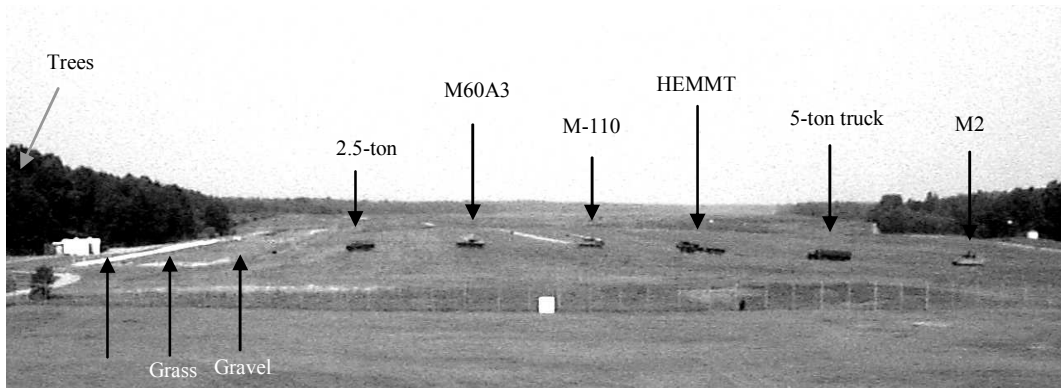


Figure 24. Locations of vehicles and natural backgrounds during the field test portion of the research.

The chosen vehicles for the data collection were a 2.5-ton truck, a 5-ton truck, an M60A3, an M-110, an M-2, and a HEMMT. The vehicles represented a diversity of shape and construction materials. For instance, the M-110, the M60, and the M-2 had tracks, while the rest of the target set had rubber wheels. The 2.5-ton truck had wooden sides around the bed of the truck. The natural backgrounds present were gravel, grass, sand, and deciduous trees, which represented common backgrounds. Three blackbodies were also placed at the same range as the vehicles. As stated earlier, these blackbody sources allowed the generation of calibration curves to convert sensor gray levels to equivalent blackbody source temperature. The meteorological data collected were wind

speed, wind direction, relative humidity, ambient temperature, ground temperature, visible down welling solar radiance, visible upwelling solar radiance, thermal down welling infrared radiance, and thermal upwelling infrared radiance.

The field test was conducted over four distinct days. The first day was equipment setup. During this time, the imaging system was setup and the vehicles were driven into place at the appropriate range. The second day, the vehicles remained on the range with their engines off during the collection. This provided imagery of “cold” vehicles that had been dormant for many hours. The third day, the vehicle engines were idled for the data collection. The targets were not exercised or driven during this time period except for re-fueling. This ensured that the only source of heat from the vehicle was the engine and exhaust. The fourth day, the vehicles were exercised prior to the data collections and the engines were left idling. Position stakes were placed on the test range to ensure that the vehicles were returned approximately to their previous position after the exercise period. These three operational states represented the most common vehicle states of operation. By changing the state of operation of the vehicles during the data collection, spectral information changes could be measured and compared.

### **4.2.3 Sensor Used**

The thermal imager used to collect the imagery was a FLIR Systems LabCAM provided by FLIR Systems, Boston. This thermal imager consisted of a pour-fill liquid nitrogen dewar containing a 320x240 pixel InSb MWIR focal plane array, a manually adjustable four-position cold filter wheel, a modified MilCAM RECON product optics, and COTS camera drive and data acquisition electronics, as shown in Figure 25.

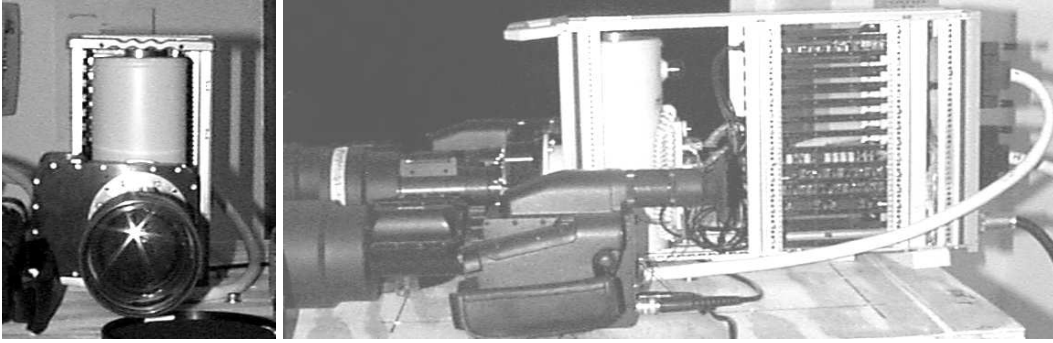


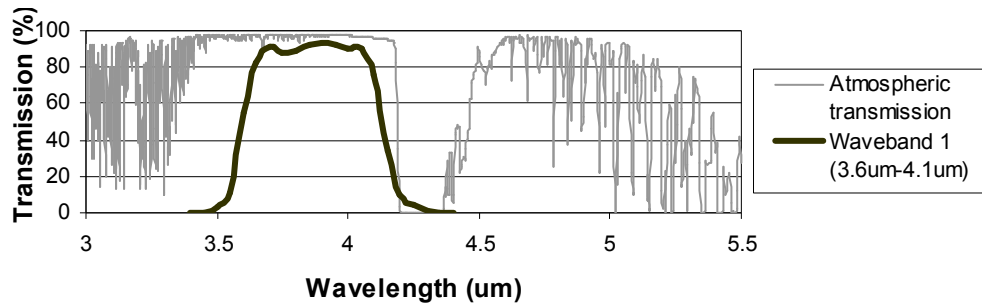
Figure 25. Front and side view of InSb midwave thermal imager with cold filter wheel.

The optical filters were housed in a manual four-position filter wheel contained within the vacuum dewar. Shielded from external warm surfaces and cooled by conductive and radiative processes, the optical filters achieved temperatures below 150 K, minimizing out-of-band background radiation. The center wavelengths for three of the filters were 3.9  $\mu\text{m}$ , 4.7  $\mu\text{m}$ , and 4.3  $\mu\text{m}$ . The fourth filter was a CO<sub>2</sub> blocking filter and spanned the wavelengths of 3.6 to 4.1  $\mu\text{m}$  and 4.5 to 4.9  $\mu\text{m}$ . Figure 26 shows each filter spectral transmission characteristic and the atmospheric model provided by MODTRAN. These filters provided reasonable MSI characteristics in both spectral wavelength and spectral extent. The filters were also available in a size compatible with the filter wheel openings.

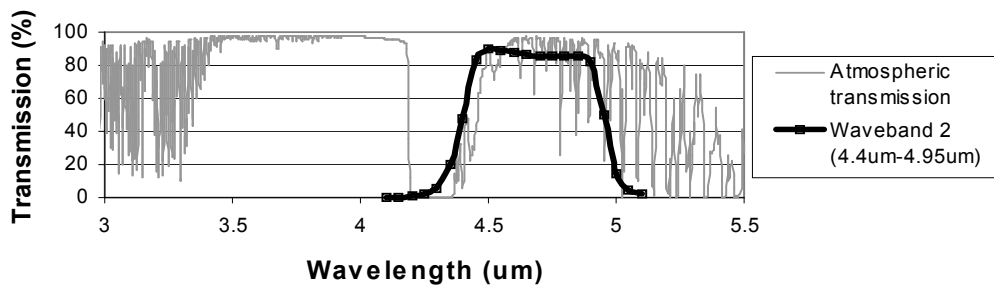
Imagery was acquired for each filter setting by sequentially adjusting the filter wheel by means of an external rotary knob. The optics used on the LabCAM were a modified version of FLIR's RECON product optics. Specifically, the optics were an F/4.5 with a narrow FOV of 1.7° and effective focal length (EFL) of approximately 320 mm.

The configuration of the sensor and filters provided additional challenges not found with the use of spectral filters positioned in front of the collection optics. These cold filters, located between the collection optics and the detector array, were in a converging beam. Because of the location of the filters, refocusing was required when a new filter was selected.

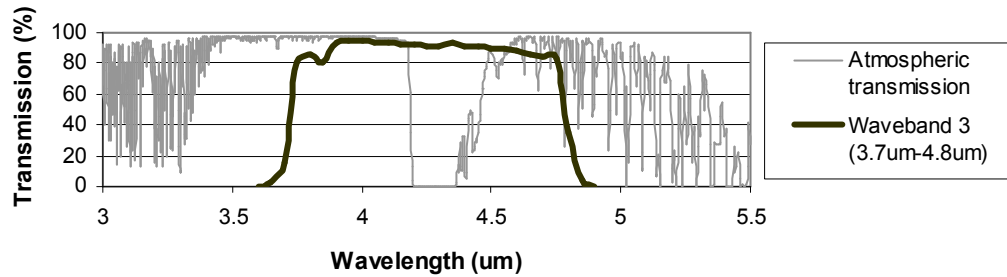
**Atmospheric Transmission and Filter 1 Characteristics**



**Atmospheric Transmission and Filter 2 Characteristics**



**Atmospheric Transmission and Filter 3 Characteristics**



**Atmospheric Transmission and Filter 4 Characteristics**

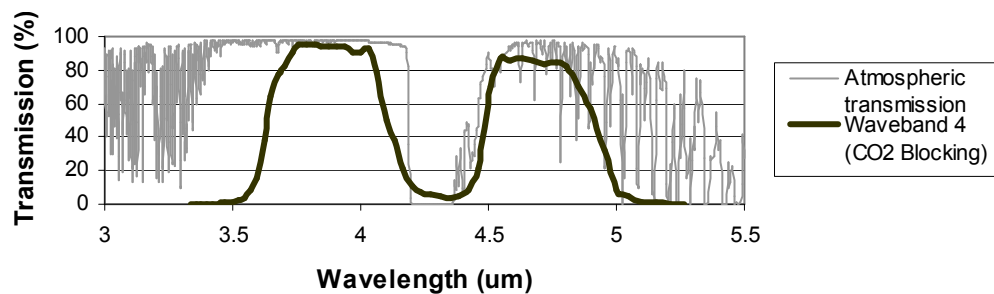


Figure 26. Atmospheric transmission model and spectral wavebands for each cold filter.

### **4.3 Correlation Analysis**

For the portion of the data evaluated, nighttime images of the natural backgrounds were not useful because of low SNR. The analysis was limited to comparisons of vehicles at night between their three states of operation and comparisons of information for both backgrounds and vehicles through the day. All images were segmented to exclude unwanted objects from the comparison. All pixels that were not part of the target were set to zero, as shown in Figure 27. The target pixels were then converted to radiometric temperatures.

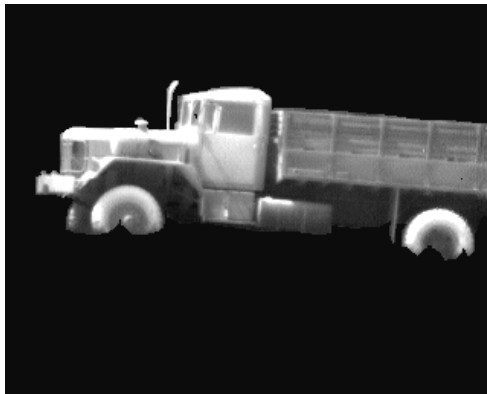


Figure 27. Segmented image of 5-ton truck

The vehicles chosen for the analysis were the M-110, M60A3, 2.5-ton truck, and 5-ton truck. These vehicles were chosen because most of the vehicle was represented in the thermal imager FOV, as shown in Figure 27.

The method for comparing information content in this research was correlation analysis. Previous research by Moyer [64] investigated four different information

comparison techniques. For the errors considered, the correlation analysis was the most consistent of the techniques. To perform this analysis, the first step was to obtain a zero-mean image. Since the spectral images were segmented, the average value for all the target pixels was calculated and subtracted from every target pixel. This image correction process is :

$$\begin{aligned} \text{Corrected Image}_1(x, y) &= \text{Image}_{1\text{tgt}}(x, y) - \text{mean}(\text{Image}_{1\text{tgt}}(x, y)) \\ \text{Corrected Image}_2(x, y) &= \text{Image}_{2\text{tgt}}(x, y) - \text{mean}(\text{Image}_{2\text{tgt}}(x, y)) \end{aligned} \quad (22)$$

where  $\text{Image}_{1\text{tgt}}$  are the target pixels of a spectral image, and  $\text{Image}_{2\text{tgt}}$  are the target pixels of a second spectral image which contained the same target as  $\text{Image}_{1\text{tgt}}$ . Once the input images had a zero mean, the spatial correlation coefficient calculation defined in Equation (23) was performed.

$$\rho_{1,2} = \frac{\max\left(\sum_{m=1}^M \sum_{n=1}^N \text{Corrected Image}_1(m, n) \times \text{Corrected Image}_2(m-x, n-y)\right)}{((M \times N) - 1) \times \sigma_{ci_1} \times \sigma_{ci_2}} \quad (23)$$

where max represents the maximum value of the correlation matrix,

$\sigma_{ci_1}$  is the standard deviation of  $\text{Corrected Image}_1$ , and  $\sigma_{ci_2}$  is the standard deviation of  $\text{Corrected Image}_2$ . Because of the similarity of the imagery, a positive value was expected in the correlation matrix. Therefore, the maximum value of the correlation matrix was used. The product of the individual image standard deviations and the size of the resultant correlation matrix normalized this maximum value, yielding the correlation coefficient. If the images were perfectly registered, the center of the correlation matrix would be the correct value for the analysis. These images were not registered, however, the images were very similar and the maximum value of the correlation matrix was taken as the correct value.

Because of the size of the targets in the images, the edges of the image were padded with additional zeros. This was to prevent any edge effects from compromising the calculation. It also allowed smooth correlations to be calculated with no discontinuities.

## **4.4 Error Analysis**

Several errors reduce the calculated correlation coefficient such as distortion, misregistration, segmentation, dead pixels, and thermal imager noise. Misregistration errors are addressed by Stocker et al. [55]. My research focused on the errors caused by dead pixels and thermal imager noise. To study the impact of these errors on the correlation coefficient calculation, the errors were simulated on pristine, high-contrast images, which were collected during the field test described in section 4.2.

### **4.4.1 Dead Pixels**

Dead pixels are those pixels that have zero response regardless of input. The dead pixels in the images were identified and replaced with an eight-pixel nearest-neighbor average. If the images were spatially registered between filters on the focal plane, the problem of dead pixels would not have been as significant. However, the sensor was positioned by hand. This meant the dead pixels would appear to be at different locations on the vehicles and backgrounds between waveband images. To quantify the impact of this error, a high-resolution image was chosen and copied. A random pixel was chosen in each image and the value replaced with zero. The images were then corrected to a common temperature scale. It was determined that a small percentage of dead pixels, one in 12,000 active

pixels, was sufficient to cause a near zero correlation coefficient. The extreme value of a dead pixel effectively caused a singularity. The resultant correlation matrix reached a maximum when the dead pixels were aligned regardless of the alignment of the target.

#### **4.4.2 Thermal Imager Noise**

The 3-D noise measurements assume that thermal imager noise is uncorrelated to the scene and all the noise components are uncorrelated with each other. This allows the noise to be characterized as spatially white and Gaussian distributed in amplitude. This type of noise would lower the correlation coefficient by increasing the target standard deviation. The original standard deviations of the natural background images used in this analysis were 0.25K, 0.36K, 0.24K, and 0.24K for waveband images 1 through 4 respectively. Seven different levels of noise were simulated and applied to the original images. The pair-wise correlation coefficients were calculated between all six combinations of the waveband imagery and the results are shown in Figure 28.

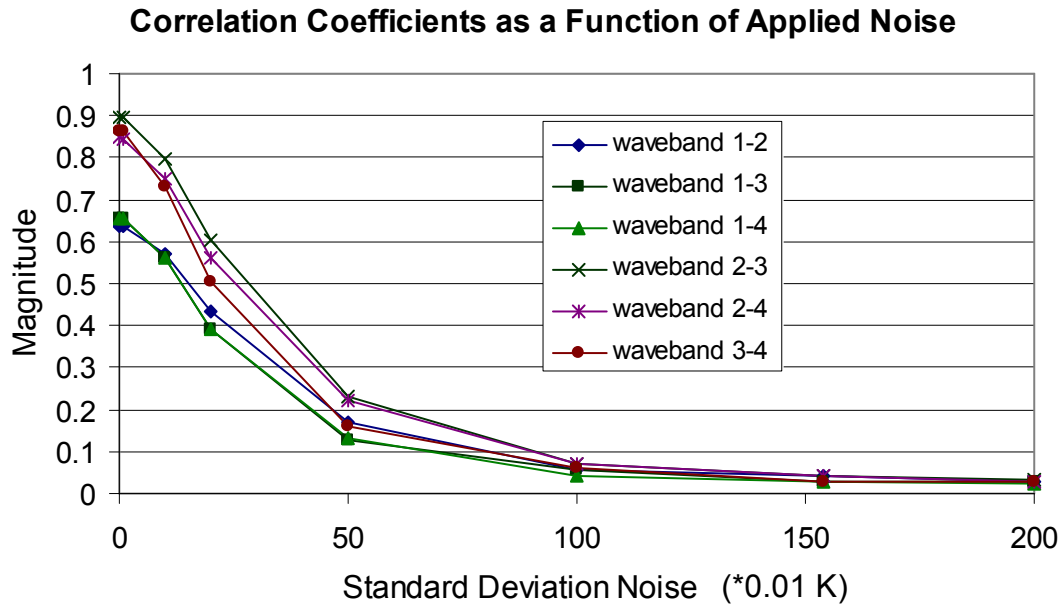


Figure 28. Correlation coefficient decay as a function of applied image noise.

As expected, the higher the standard deviation of the applied noise, the closer the correlation coefficients approached zero. If the noise only contributed to the image standard deviation, then only the denominator of Equation (23) would be affected. If this hypothesis was true, the noise term could be subtracted out in quadrature from the individual scene standard deviations using:

$$\sigma_{\text{Image}} = \sqrt{(\sigma_{ci})^2 - (\sigma_{\text{Noise}})^2} \quad (24)$$

where  $\sigma_{ci}$  is the standard deviation of the zero mean input image and  $\sigma_{\text{Noise}}$  is the standard deviation of the thermal imager noise. The noise for a single frame would be the sum of the first seven noise terms listed in Table 1. After noise correcting the standard deviations, as shown in Equation (24), the correlation coefficients were recalculated and are shown in Figure 29.

### Correlation Coefficients with Image Noise Removed

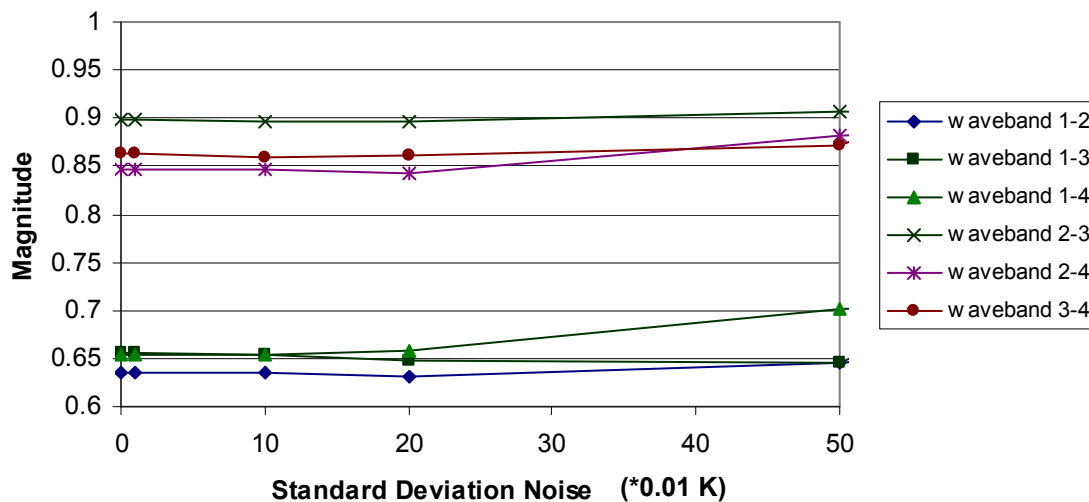


Figure 29. Noise corrected correlation coefficients.

These results show that the original correlation coefficient was predictable to within  $\pm 0.4\%$  after removing the standard deviation contribution of the noise. Note, if the standard deviation of the noise is more than twice as large as the original scene standard deviation, this error correction methodology becomes unpredictable. This research establishes a limit that the thermal imager noise needs to be less than the scene standard deviation for this correction methodology.

## 4.5 Results

The primary goal of this research was to develop a methodology of collecting multi-spectral images and quantifying the information differences between the spectra. With a sound methodology and analysis technique, the spectral information differences between

vehicles and backgrounds independent of each other could be measured. For the military vehicles, changes in the correlation coefficients could be measured versus the state of vehicle operation and versus the time of day. For the background, changes in the correlation coefficients could be measured versus the time of day. To analyze the effect of vehicle operating state on the correlation coefficient, images were chosen from 9:00 PM EDT. This ensured that the signatures being analyzed were emissive and did not depend on vehicle reflectivity from down-welling solar radiance. Table 3 shows the pair-wise correlation coefficients between wavebands for the vehicles under various operating conditions.

Table 3. Measured average pair-wise correlation coefficients for vehicles spanning their operational extent. (a) cold vehicles, (b) idled vehicles, and (c) exercised vehicles.

		Waveband			
		1	2	3	4
Waveband	1	1.00			
	2	0.79	1.00		
	3	0.81	0.86	1.00	
	4	0.80	0.85	0.88	1.00

(a)

		Waveband			
		1	2	3	4
Waveband	1	1.00			
	2	0.80	1.00		
	3	0.82	0.93	1.00	
	4	0.79	0.91	0.93	1.00

(b)

		Waveband			
		1	2	3	4
Waveband	1	1.00			
	2	0.83	1.00		
	3	0.81	0.94	1.00	
	4	0.83	0.94	0.96	1.00

(c)

There appears to be a slight systematic increase in the correlation coefficient through the states of operation. Shown in Figure 26 are the spectral extents for the filters. Recall that waveband 1 consists of radiation only less than the CO<sub>2</sub> notch. Waveband 2

consists of radiation only greater than the CO<sub>2</sub> notch. Wavebands 3 and 4 have radiation contributions from both sides of the CO<sub>2</sub> notch. When the short wavelength filter, waveband 1, was correlated with the other filters there was at most a 5 percent increase in the correlation coefficient. However, when the filters that contained longer wavelength contributions, wavebands 2, 3, and 4, were correlated to each other there was an increase of 10 percent in the correlation coefficient. As the vehicles generated their own source of heat, the wavebands that contained longer wavelengths became more similar. When the short wavelengths were isolated from the long wavelengths, the information differences remained relatively constant.

In order to compare the correlation coefficients for the military vehicles throughout the day, images were selected from three different hours on the day that the vehicles were cold; 11:00 AM EDT, 1:00 PM EDT, and 9:00 PM EDT. The backgrounds were analyzed for the 11:00 AM EDT and 1:00 PM EDT. At 9:00 PM EDT the backgrounds did not possess a sufficient variance in temperature. Hence, the thermal imager noise, as shown in section 4.4.2, was larger than the scene variance. Table 4 shows the correlation coefficients for the vehicles during these hours and Table 5 shows the correlation coefficients between wavebands for the backgrounds.

Table 4. Measured average pair-wise correlation coefficients of vehicles for specific hours over the day. (a) 1100 hours, (b) 1300 hours, and (c) 2100 hours.

		Waveband			
		1	2	3	4
Waveband	1	1.00			
	2	0.90	1.00		
	3	0.94	0.96	1.00	
	4	0.91	0.96	0.97	1.00

(a)

		Waveband			
		1	2	3	4
Waveband	1	1.00			
	2	0.89	1.00		
	3	0.90	0.96	1.00	
	4	0.90	0.94	0.94	1.00

(b)

		1	2	3	4
Waveband	1	1.00			
	2	0.79	1.00		
	3	0.81	0.86	1.00	
	4	0.80	0.85	0.88	1.00

(c)

Table 5. Measured average pair-wise correlation coefficients of backgrounds for specific hours over the day. (a) 1100 hours and (b) 1300 hours.

		Waveband			
		1	2	3	4
Waveband	1	1.00			
	2	0.64	1.00		
	3	0.66	0.90	1.00	
	4	0.65	0.85	0.86	1.00

(a)

		Waveband			
		1	2	3	4
Waveband	1	1.00			
	2	0.34	1.00		
	3	0.34	0.42	1.00	
	4	0.28	0.43	0.49	1.00

(b)

There was a decrease in the correlation coefficient throughout the day for both vehicles and background. The background correlation coefficients changed radically between 11:00 AM EDT and 1:00 PM EDT. At 11:00 AM, the sun was closer to the horizon and more directly illuminated the background images. At 1300, the sun was overhead and illuminated the tree canopy, producing lower dynamic range images. The change in this sun-scene-sensor geometry may have caused the reduction reported for the

backgrounds. Another possible cause for the decorrelation in the background images was wind speed and direction. This effect could cause subject matter in the scenes, trees, to shift to different relative positions within the scene and would provide a decorrelation effect. The effect of wind would go unobserved for the military targets in this research. There was about a 0.1 decrease in the correlation coefficient for all pair-wise vehicle correlations from 11:00 AM until 9:00 PM. It should be noted that during the day the short wavelength filter, waveband 1, possessed a correlation coefficient of 0.9 and greater with all other wavebands. This suggested that for non-operated vehicles, the downwelling solar radiance provided a more similar scene between the short wavelengths and the longer wavelengths.

#### ***4.6 Multiband Discussion***

There are two important points seen in this research. The research presented compared a more reflective waveband, waveband 1, with a more emissive waveband, waveband 2. The short wavelength midwave region is known to possess a larger reflective component for most materials than the long wavelength midwave region. The correlation coefficients for the backgrounds at 11:00 AM were 0.64 in this research. While not comparing the same identical wavebands, the natural background measurements in my research have less than a 10 percent difference from Scribner's midwave/long wave comparison of a whole scene. The vehicles at this same time, possessed a correlation coefficient of 0.90. This yields a difference of more than 50 percent between Scribner's comparison and mine. Scribner's whole-scene correlations may have been dominated by the natural background component.

The second important point is that the daytime correlations between wavebands were higher than the nighttime correlations for vehicles. It is usually assumed that the solar reflections in the shorter wavelength midwave region cause a significantly different signature than in the longer wavelength midwave region because of higher material reflectivity at these wavelengths. I found the opposite effect in my research. It is possible that the lack of ambient light reflected from the target in the shorter wavelength region makes for a less radiometrically equivalent signature than in the longer wavelength region. While solar irradiance is significant, it is modified by a small reflectivity where the sum of the total radiance, both emitted and reflected, is closer to the longer wavelength signature. I observed these points for this research and these points may not necessarily be generalized for all radiometric cases.

The effects of dead pixels and thermal imager noise on the correlation coefficient calculation were investigated. The correlation coefficient was found to be extremely sensitive to dead pixels such that if dead pixels exist in the imagery those pixels need to be replaced prior to the calculation. A technique was found and tested to remove the effect of thermal imager noise from the correlation coefficient calculation. This technique corrects the calculation to within  $\pm 0.4$  percent of a noise free coefficient value, but is only reliable if the standard deviation of the noise is less than the standard deviation of the input scene. This noise correction technique provides guidance on the quality of thermal imager necessary to conduct future research with this methodology.

## 5 Target Acquisition Model for Handheld Objects

With the current emphasis on urban operations in the Army, force protection in the Navy, and population security in Homeland Defense, researchers are proposing the utilization of various imaging systems to create a more secure environment. My research is the first attempt to develop a mathematical imager performance model that addresses a facet of this complex problem. The target acquisition identification model is successfully applied to various sets of military vehicles in multiple wavebands and also to the detection of humans. My research further extends the target acquisition approach to a set of handheld objects for the determination of a 50-percent probability of identification cycle criterion ( $N_{50}$ ). This cycle criterion, coupled with the thermal imager MRT and the target characteristics, allows the probability of identification versus range to be calculated for the visual identification task, thus providing a useful target acquisition model for urban applications. To measure a relevant visual task discrimination criterion requires: defining target sets and target area, quantifying the observers variability and minimizing their learning effects, and confirming the measurements.

This research objective is to develop a target acquisition model for the MWIR and LWIR spectrum that addresses a visual identification task found in an urban environment. The targets in this research are not military vehicles, but rather objects normally held or used in a single hand.

This chapter begins with the development of a list of relevant objects, examples of the image sets used in the perception tests, and a description of the image processing performed to prepare the images for the human perception model development experiment. These experimental results are presented along with the target acquisition

model for each waveband. Using this new target acquisition model in conjunction with the thermal imager model, NVTherm 2002, a comparison is shown between the model predictions and a second independent human perception experiment (i.e., validation of the developed model).

### ***5.1 Defining the Object Set***

Table 6 shows a list of 33 objects created for my experiment. This list was sent to 22 law enforcement officers, both civilian and military police. The officers were directed to order the list of items as they would expect to encounter them in society, starting with the most common item they expected to see. The purpose of ordering the list was to solicit expert opinion in identifying those objects most commonly found in a largely peaceful population while including the most common items they were likely to encounter.

Table 6. List of 33 items presented to law enforcement officers for ordering.

<b>Items</b>	<b>Items</b>
Pack of Cigarettes	Knife
Soda Can	Rock
Mug/Cup	Hat (ski)
Lighter	Pistol
Flashlight	Brick
Sunglasses	Flask (liquor)
Radio (communication)	Night Vision Goggles (NVG's)
Wallet	PDA
Cell Phone	Binoculars
Newspaper (folded)	Hand Grenade
Water Bottle (glass)	C4 Explosive
Camera	Dynamite
Walkman/CD Player	Camcorder
Towel (hand)	Hammer
Purse (small)	Molotov Cocktail (not lit)
Book (small)	Electric Drill
Small Umbrella	

Upon ranking the objects in the order of expected appearance, the list was split into three categories based on a person's associated intent with the object. The three categories were innocuous, surveillance, and dangerous/lethal objects. Table 7 lists the objects in their respective categories. These objects and categories provided the most common items that law enforcement personnel expected to encounter that included both threatening and non-threatening intent. This allows the target acquisition model to reflect the most important situations law enforcement officers are required to discern.

Table 7. Ordered list of all items separated into categories.

Innocuous Items	Surveillance Items	Dangerous/Lethal Items
Pack of Cigarettes	Radio (communication)	Knife
Soda Can	Cell Phone	Rock
Mug/Cup	Camera	Pistol
Lighter	Camcorder	Brick
Flashlight	PDA	Hand Grenade
Sunglasses	Binoculars	C4 Explosive
Wallet	Night Vision Goggles (NVG's)	Dynamite
Newspaper (folded)		Molotov Cocktail (not lit)
Water Bottle (glass)		
Walkman/CD Player		
Towel (hand)		
Purse (small)		
Book (small)		
Small Umbrella		
Hat (ski)		
Flask (liquor)		
Hammer		
Electric Drill		

Of the 15 objects listed in the first five rows of Table 7, only 12 objects were required to construct a human perception experiment of reasonable length. There are numerous discrimination research efforts based on 12 representative targets at 12 representative aspects that have been shown to eliminate target and aspect biases. All 15 objects were obtained in the data collection for future comparative studies. However, in this first research only 12 objects were used. The following 12 objects, as shown in Table 8, were chosen to represent a mixture of innocuous, surveillance, and potentially lethal objects.

Table 8. Final list of objects imaged for the human perception experiments.

Soda Can
Mug/Cup
Flashlight
Radio (communication)
Cell Phone
Camcorder
PDA
Knife
Rock
Pistol
Brick
Hand Grenade

## **5.2 Image Collection**

The image collection of the 15 items listed in Table 8 was performed at night. All images were collected within a 24-hour period. Table 9 lists the thermal imager specifications, the range from the imager to the objects, and the height from the ground to the imagers.

Each object was imaged at 12 aspects, yielding 180 images. Eight of the aspects were taken at a shallow angle, as shown in Figure 30, and the other four aspects were taken at a large down-look angle of  $55^\circ$  at the aspects of  $0^\circ$ ,  $90^\circ$ ,  $180^\circ$ , and  $270^\circ$ . These aspects were chosen as representative of what a law enforcement officer would see through a thermal imager when viewing a person with an object in his/her hand. By simplifying the collection to these 12 aspects, a well-defined image set could be constructed.

Table 9. Sensor specifications, heights, and ranges to the objects for each waveband.

	MWIR Sensor	LWIR Sensor
Nomenclature	TVS 8500	TVS 700
lens focal length	30mm	35mm
sensor FOV	14.6°	26°
imager array format	256 x 236	320 x 240
individual detector size	30μm	50μm
Range to Object (Shallow Angle)	7' 9" 2.36 m	4' 2" 1.27 m
Height from Ground (Shallow Angle)	4' 6" 1.37 m	4' 6" 1.37 m
Range to Object (Large Angle)	6' 6" 1.98 m	4' 4" 1.32 m
Height from Ground (Large Angle)	8' 3" 2.51 m	6' 11" 2.11 m

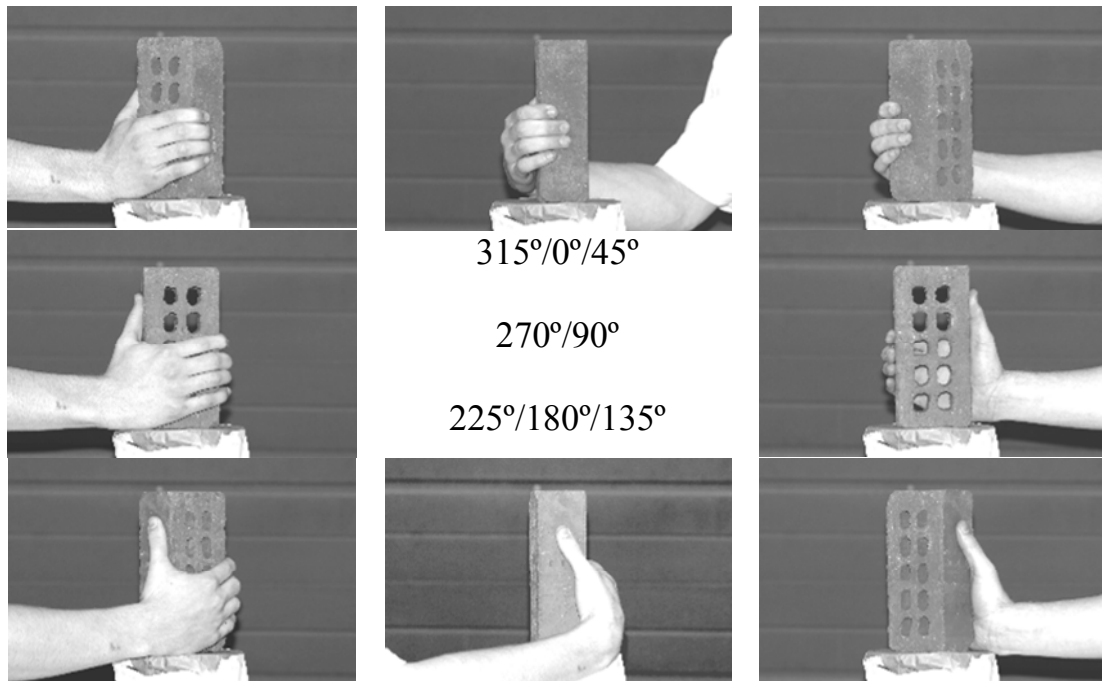


Figure 30. Visible image illustrating the orientation of the objects to the thermal imagers.

As shown in Figure 30, the objects were held in a single hand on top of a tripod to ensure that all objects would be at the same height, 4.5 feet. The tripod allowed directional markings to be used as reference points for consistent orientation between the hand and the thermal imagers. The background was characterized as low-clutter that did not provide significant competing information with the imaged objects. The thermal imagers were radiometrically calibrated and provided a conversion from gray scale values to temperature.

### ***5.3 Image Processing for Experimentation***

Each thermal imager possesses a different focal plane format and imaging characteristic, as listed in Table 9. This section outlines the image processing performed on all images from their raw form to the final processed experimental imagery presented to the observers. The image processing for each waveband is presented individually and the section concludes with the target-to-background contrast and critical dimension calculations for each image set.

#### **5.3.1 Mid-wave Infrared (MWIR) Spectrum**

MWIR images were acquired with an Avio TVS-8500 cooled InSb radiometrically calibrated thermal imager. The spectral range of the imager was 3 to 5  $\mu\text{m}$ , with a blocking filter between the wavelengths of 4 to 4.2  $\mu\text{m}$ . This blocking filter eliminated the spectral contribution from emissions of the CO<sub>2</sub> absorption band. The output image was 256 x 236 pixels and was sufficient to provide good rendition of the objects. Shown in Figure 31 is an example of these objects in the MWIR spectrum at the same aspect.

These example images are a subset of the 144 baseline images for the MWIR spectrum perception experiment.

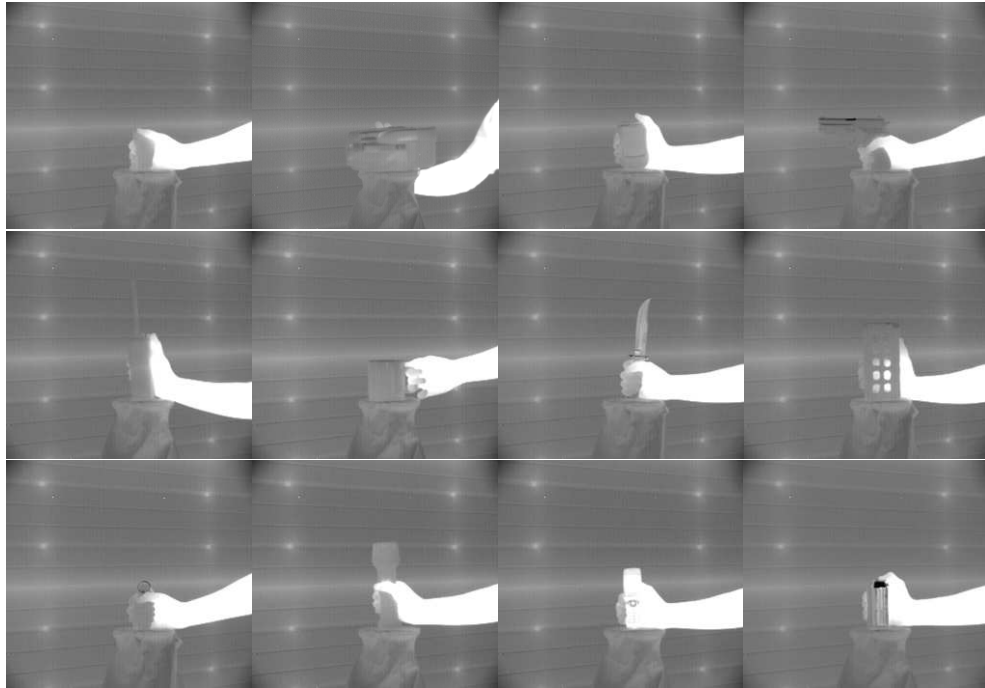


Figure 31. Example MWIR images of all 12 objects at the same aspect.

Similar to the sampling experiments performed in section 3.2.2, the image set was evenly divided between six experimental cells. Each experimental cell contained 24 images consisting of two images from each aspect and two images of each object. Distributing the 144 images among six experimental cells eliminated experimental biases of target groupings and aspects while maintaining a short perception experiment to minimize observer fatigue. The blur levels were increased for each experimental cell, as illustrated in Table 10.

Table 10. Experimental matrix showing the width of the applied blur parameters.

	Blur(Pixels)					
	5	8	11	14	17	20
Cell	A	B	C	D	E	F

The blur values from Table 10 were used as the b parameter in constructing the blur kernel that was applied to the imagery. The blur kernel took the form

$$\text{blur} = \exp\left(-\pi\left(\frac{x}{b}\right)^2\right), \quad (25)$$

where b dictates the width of the Gaussian type blur. Equation (25) was convolved over each image in both the x and y-dimensions separately. This method allowed for the contraction of the system MRT in a regular and known fashion so that the number of resolvable cycles could be easily calculated. It should be noted that in this first experiment, only the system MRT was contracted to limit the number of resolvable cycles seen by the observer. There was no attempt to create a range simulated image for this experiment.

### 5.3.2 Long Wave Infrared (LWIR) Spectrum

LWIR images were acquired with an Indigo TVS-700 uncooled microbolometer radiometrically calibrated thermal imager. The spectral range of the imager was 8 to 12  $\mu\text{m}$ . The output was a 320 x 240 pixel image. The images were cropped to form a 256 x 236 image. Cropping the image allowed the stimulus area presented to the observers eye

to remain constant between the MWIR and LWIR experiments. Figure 32 shows an example of these images. These example images were a subset of the 144 baseline images for the LWIR spectrum perception experiment.

Similar to the MWIR spectrum, these images were divided among the six experimental cells such that each experimental cell contained two images of all 12 objects shown at two aspects. The experimental images presented to the observers were created with the identical process as in the MWIR spectrum. The imagery between the MWIR and LWIR sets appeared very similar. The highly reflective surfaces, such as the top of the soda can, the receiver slide of the pistol, and the knife blade, all showed strong environment reflections. For the surfaces pointing upward, a strong cold sky reflection was seen. For the entire data set, the task of identifying these objects in the MWIR and LWIR appeared to be equally difficult.

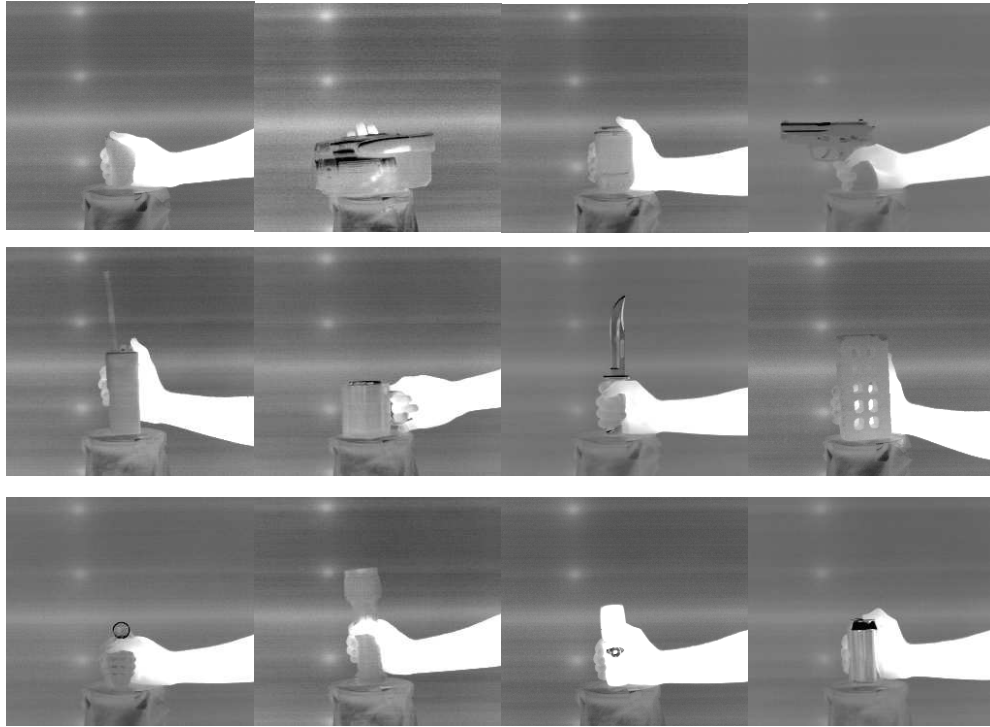


Figure 32. Example LWIR images of all 12 objects at the same aspect.

### 5.3.3 Image Calculations

Each image was segmented to clearly define the target area and the background. The target area for this research was defined as the inanimate object and the individual's hand to the wrist. This approach took into consideration the fact that hand/finger position relative to the object also provides some information for identifying the object. Once the images were segmented, the target area was calculated as the square root of the number of pixels on the object and hand. When calculating resolvable cycles, the area measured in display pixels was converted to a linear measurement in centimeters using the sample spacing of a pixel on the display. This linear measurement was converted to an angular

measurement to the eye by knowing the distance the observer's eye was located from the display.

With the definition of target characteristic dimension being the square root of an area, the target characteristic dimension cannot be related back to line pairs of resolution as was possible when the target was characterized by a 1-D critical dimension as was used in the original Johnson paper [7]. Table 11 shows the average characteristic dimension of the objects in each experimental cell. Although there is variability in size between the wavebands studied, the size between experimental cells within a waveband has much less variability. Therefore, the applied blur for each experimental cell will determine the human observer performance and not the changes in the characteristic dimension.

Table 11. Average characteristic dimension and contrast for the image set for each experimental bin.

Experimental Cell	MWIR		LWIR	
	Size (pixels)	Contrast	Size (pixels)	Contrast
A	51.96	0.237	67.06	0.252
B	52.46	0.240	66.45	0.250
C	52.58	0.240	68.00	0.257
D	52.64	0.249	67.41	0.267
E	53.41	0.252	67.33	0.262
F	54.13	0.257	66.56	0.264

The contrast metric for all wavebands is calculated as

$$\text{Contrast} = \frac{\sqrt{\Delta\mu^2 + (\sigma_{tgt})^2}}{2\mu_{scene}}, \quad (26)$$

where  $\Delta\mu$  is the difference between the average object pixel value and the average background pixel value in gray levels respectively. The standard deviation of the target is described by  $\sigma_{\text{tgt}}$  and the result is normalized by twice the average scene pixel value  $\mu_{\text{Scene}}$ . The average scene value consists of the average value of the target and the background adjacent to the target. For this calculation, the number of pixels on the background should equal the number of pixels on the target. This contrast metric models the meaningful stimulus received by the eye from the monitor and may be directly compared to the human eye CTF.

#### ***5.4 Experimental Methodology and Observer Results***

An underlying assumption of the NVESD models is that all observers are experts in the particular visual perception task being investigated. This means that all observers can perform the required task, in this case visual identification of objects, to 95 percent proficiency. Training an observer to 95 percent proficiency for the task minimizes the amount of learning an observer could achieve while participating in an experiment.

To assist the observers, a training session was conducted utilizing a PowerPoint slide show. The training described the goal of the experiment, the experimental format, and showed example imagery of each target in both spectra. The training was self-paced and when the observer felt ready, a training test was administered to ensure 95 percent proficiency for the identification task in both spectra. If the observer failed to perform to this level, a test administrator provided feed back, such as which targets should be studied closer, and the observer returned to the training with emphasis on the misidentified objects.

The psychophysical test was designed as a timed 12-alternative forced choice (12AFC) experiment. When an image was presented, all possible object choices were present as selection options. The observer selected an object identification button and moved on to the next image. The results from 28 military observers were collected and the total average corrected probability of identification was calculated by

$$P(Id)_{corrected} = \frac{P(Id)_{Measured} - P(Guess)}{1 - P(Guess)}. \quad (27)$$

The  $P(Id)_{Measured}$  is the average of all 28 observer correct responses for an experimental cell. The  $P(Guess)$  is the probability that the observer had guessed correctly. In this experiment given, 12 objects, the probability of a correct guess is 1/12. The performance of the observers as a function of blur, number of pixels for the  $b$  parameter of Equation (25), is shown in Figure 33.

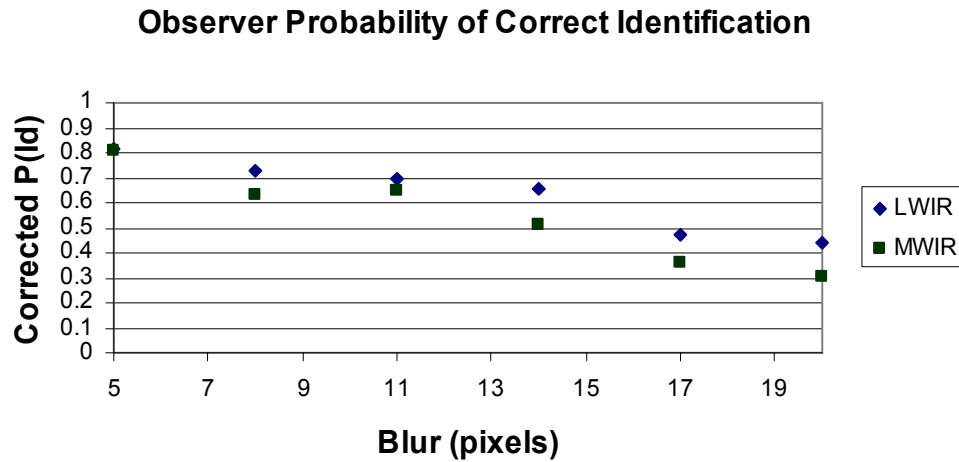


Figure 33. Human observer results, corrected for chance, and shown by experimental cell as a function of the  $b$  parameter.

As shown in Figure 33, the corrected observer probabilities spanned a range from greater than 0.8 to less than 0.5. Although observers performed worse on the MWIR images, this does not necessarily indicate that the MWIR spectrum was harder than the LWIR spectrum for this visual identification task. In order to assess which spectrum was more difficult, the resolvable cycle calculations had to be performed.

## **5.5 Resolvable Cycles Calculations**

The resolvable cycles were calculated using the Johnson metric, and as provided in section 2.3.2, were applied to both wavebands. The measurement of the resolvable cycles and curve fit of the data were performed in eye-space. The measurements necessary for the resolvable cycles calculation were related to the quantities associated with the system display. The display had been characterized for both system MTF and the mapping of gray shade values to luminance. Because of the low noise of all the imagery, Equation (4) was used. The display contrast was approximated as 1 and this reduced the system CTF curve to

$$CTF_{Sys} = \frac{CTF_{eye}}{MTF_{Sys}}, \quad (28)$$

where  $MTF_{Sys}$  was dominated by the applied experimental blur levels shown in Table 10. The limiting frequency for each experimental cell was then determined as described in section 2.3.2. Figure 34 shows the MWIR system vertical CTF calculated for experimental cell A. The intersection of the system CTF and target contrast defined the limiting resolvable frequency. The number of resolvable cycles on the target was found by multiplying the limiting resolvable frequency by the size of the target characteristic dimension in millimeters.

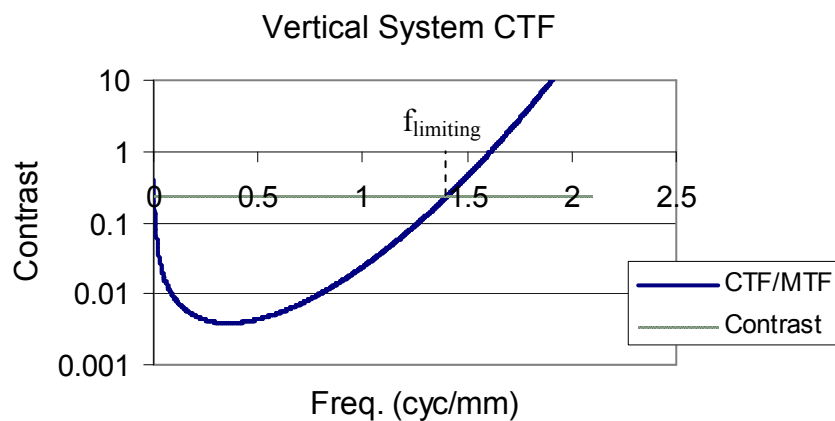


Figure 34. Example of the MWIR vertical system CTF as calculated using Equation (28).

Shown in Figure 35 are the calculated resolvable cycles for the ACQUIRE model for the experimental data and also the ACQUIRE TTPF curve fitted with the calibration factors required to achieve these fits. Although the corrected probabilities of identification for both the MWIR and LWIR spectrum were different, shown in Figure 33, the  $N_{50s}$  between these wavebands were identical. There was only a 2 percent difference between the MWIR and LWIR spectrum. To the human observer, the visual identification task for this target set in both the MWIR and LWIR waveband was equally difficult.

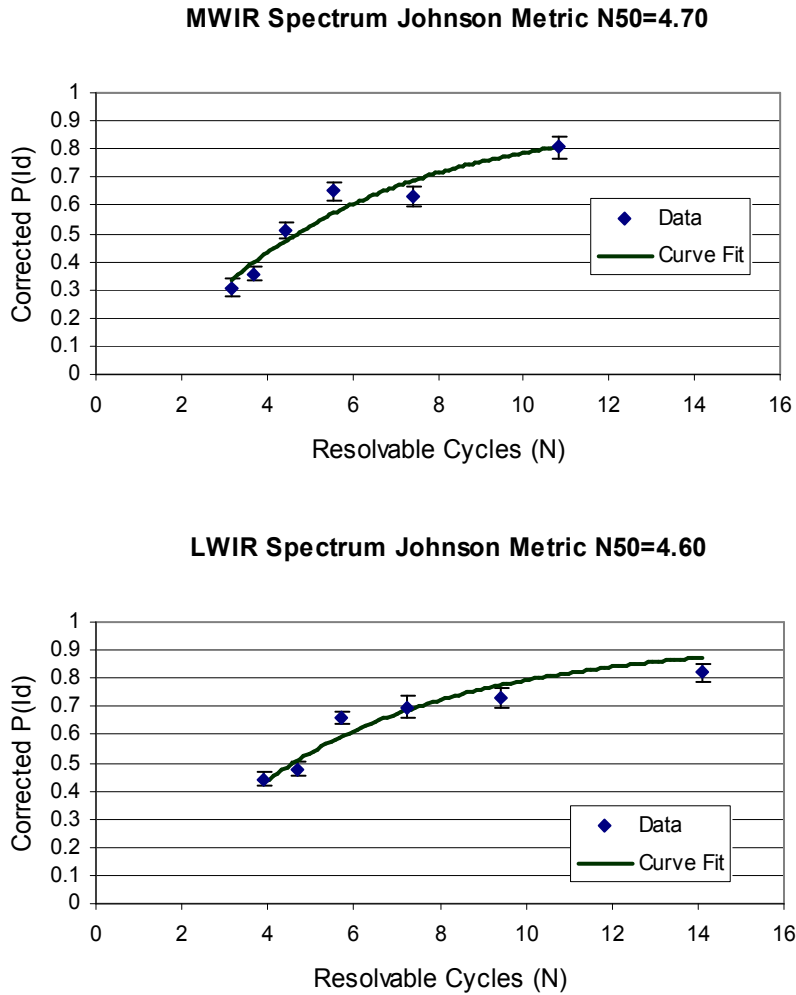


Figure 35. Resolvable cycles measured by the Johnson metric and the best fit curve for each spectrum.

Table 12. Johnson calibration factors for MWIR, and LWIR spectrum with coefficient of determination.

Spectrum	N <sub>50</sub>	Coefficient of Determination
MWIR	4.70	0.925
LWIR	4.60	0.905

## **5.6 Performance Model Predictions**

In section 5.5 the discrimination factors for the ACQUIRE model in the MWIR and LWIR spectrum possessed a number of unrealistic conditions. To reduce the number of resolvable cycles, an MTF constriction was used to reduce the number of resolvable cycles in a manner similar to an increasing range. The calculated system CTF was based on the observer CTF modified by only the monitor MTF and the applied MTF constriction. The imagery presented was noiseless, meaning the temporal and fixed pattern noises were small compared to the eye CTF. The calculations were performed in eye-space, or as the image appeared on the monitor. This approach assumed that Equation (26) in conjunction with the observer CTF was directly related to the  $\Delta T_{RSS}$  metric used in the thermal imager ACQUIRE model. Agreement between the predicted range performance of NVTherm 2002 and human perception experiments was necessary to verify that the developed  $N_{50}$  was reasonable for use in thermal imager design modeling for this task.

To test these experimental approaches, another human perception experiment was performed. Images were prepared by convolving a blur function with the imagery and then down-sampling. Convolving a blur function prior to down-sampling the imagery avoided complications resulting from aliasing. This processing produced imagery where the target size was incrementally reduced in each experimental cell and therefore more closely approximated a variable range experiment. The image set was the same as in the experiment described in section 5.4.

The inputs to NVTherm 2002 were not contrast as calculated in Equation (26) but rather contrast calculated by the  $\Delta T_{RSS}$  metric and measured in K or °C. The image set

was converted to temperature from gray shade values and the contrast for the entire image set was calculated using the  $\Delta T_{RSS}$  metric

$$\Delta T_{RSS} = \sqrt{(\Delta\mu)^2 + (\sigma_{tgt})^2} . \quad (29)$$

The average temperature of each target ( $\mu_{tgt}$ ) and the average temperature of each background ( $\mu_{bgd}$ ) were found in Kelvin, and added to the variance of the target,  $(\sigma_{tgt})^2$  also in Kelvin. Once the  $\Delta T_{RSS}$  metric was calculated for each input image, the contrast for the set of images was calculated as the average of all 144 images. The average contrast for the MWIR images was measured as 3.29°C and for the LWIR images as 2.99°C. Both the MWIR and LWIR sensors were temperature calibrated sensors, however, the 0.3°C difference in measured contrast, while small, could be accounted for in differences in emissivity between the spectra.

The characteristic dimension was calculated from the pixel count in Table 11. The number of pixels of the characteristic dimension was multiplied by the sample spacing of the sensor to arrive at an angular measurement and then multiplied by the range from the sensor to the object. The characteristic dimension for the MWIR images was 11 cm and for the LWIR images it was 11.7cm. The 7mm, or 6 percent difference between the measurements was accounted for in the sample spacing differences between the sensors and segmentation inconsistencies.

Table 13 shows the simulated ranges used for the target set and the corrected probability of identification at each range for 18 military observers. The probabilities were corrected using Equation (27). In order to achieve an independent measurement, these 18 observers did not participate in the experiment that was used to measure the  $N_{50}$  values and develop the target acquisition model.

Table 13. Simulated ranges for the MWIR and LWIR spectrum with the corrected P(Id) at each range and the associated 95% confidence interval.

MWIR			LWIR		
Ranges (m)	Corrected P(Id)	95% Confidence	Ranges (m)	Corrected P(Id)	95% Confidence
1.74	0.90	0.023	1.04	0.91	0.026
2.09	0.81	0.020	1.25	0.82	0.026
2.61	0.78	0.025	1.56	0.81	0.040
3.48	0.66	0.041	2.08	0.81	0.032
5.23	0.46	0.050	3.13	0.56	0.061
10.45	0.14	0.042	6.25	0.34	0.048

This perception experiment was also performed as a timed 12AFC experiment. However, unlike the model development experiment, the imagery was blurred and sized proportionately to the range that was simulated. The observers were trained to a 95 percent visual identification ability for the target set using the same training package as the discrimination criteria experiment.

The experimental results in Table 13 show the chance corrected probability of identification versus range with the 95 percent confidence intervals. The observer results have been corrected in the same manner as given by Equation (27). The 95 percent confidence interval was calculated as

$$Confidence = \mu \pm 1.96 \bullet \left( \frac{\sigma}{\sqrt{N}} \right), \quad (30)$$

where  $\mu$  and  $\sigma$  represent the average and standard deviation of the observer's average performance,  $N$  is the number of observers who participated in the experiment, 18, and

1.96 is the area enclosed by the normal distribution curve to the 95 percent point of the distribution.

The thermal imagers, both MWIR and LWIR, display, and additional MTFs were then modeled in NVTherm 2002 using the  $\Delta T_{RSS}$  contrast, calculated target dimension, and  $N_{50}$  measured from the model development experiment. NVTherm 2002 was employed in two sets of calculations. The first set of performance calculations was performed on a range-by-range basis. This means the NVTherm 2002 predictions had the same additional pre-sample MTF that was applied to the images at each range. The predictions are listed in Table 14 and Table 15 for the MWIR and LWIR imagers respectively.

Table 14. Observer performance with MWIR range simulated imagery and model predictions for the same task.

MWIR	Observers		NVTherm 2002 Prediction	Absolute Difference
Range (m)	P(Id)	Confidence Interval $\pm$	P(Id)	
1.74	0.90	0.023	0.92	0.000
2.09	0.81	0.020	0.87	0.040
2.61	0.78	0.025	0.81	0.005
3.48	0.66	0.041	0.73	0.029
5.23	0.46	0.050	0.58	0.070
10.45	0.14	0.042	0.33	0.148

Table 15. Observer performance with LWIR range simulated imagery and model predictions for the same task.

LWIR Range (m)	Observers		NVTherm 2002 Prediction	Absolute Difference
	P(Id)	Confidence Interval $\pm$	P(Id)	
1.04	0.91	0.026	0.95	0.014
1.25	0.82	0.026	0.92	0.074
1.56	0.81	0.040	0.88	0.030
2.08	0.81	0.032	0.82	0.000
3.13	0.56	0.061	0.70	0.079
6.25	0.34	0.048	0.45	0.062

The absolute difference column in each table is the difference between the NVTherm 2002 predictions and the measured corrected probability of identification of the observers with the confidence interval. For the MWIR spectrum, the prediction with the largest difference occurred at the longest range with a measured probability including confidence interval being 0.182 and NVTherm 2002 predicting 0.33. Because of the low probabilities, this point was less important for the identification task. All other predicted points are within 7 percent of the measured values with 95 percent confidence and the correlation coefficient between the measured probability and the predicted probability was 0.998. For the LWIR spectrum, all predicted points are within 8 percent of the measured values with 95 percent confidence and the correlation coefficient between the measured probability and the predicted probability was 0.982.

To show a continuous range versus probability performance curve from NVTherm 2002, the additional applied pre-sample MTFs at each range were averaged together. This method does not represent the system at each range but rather the system

averaged over all ranges. The predicted range performance curves for these averaged thermal imaging systems are shown in Figure 36.

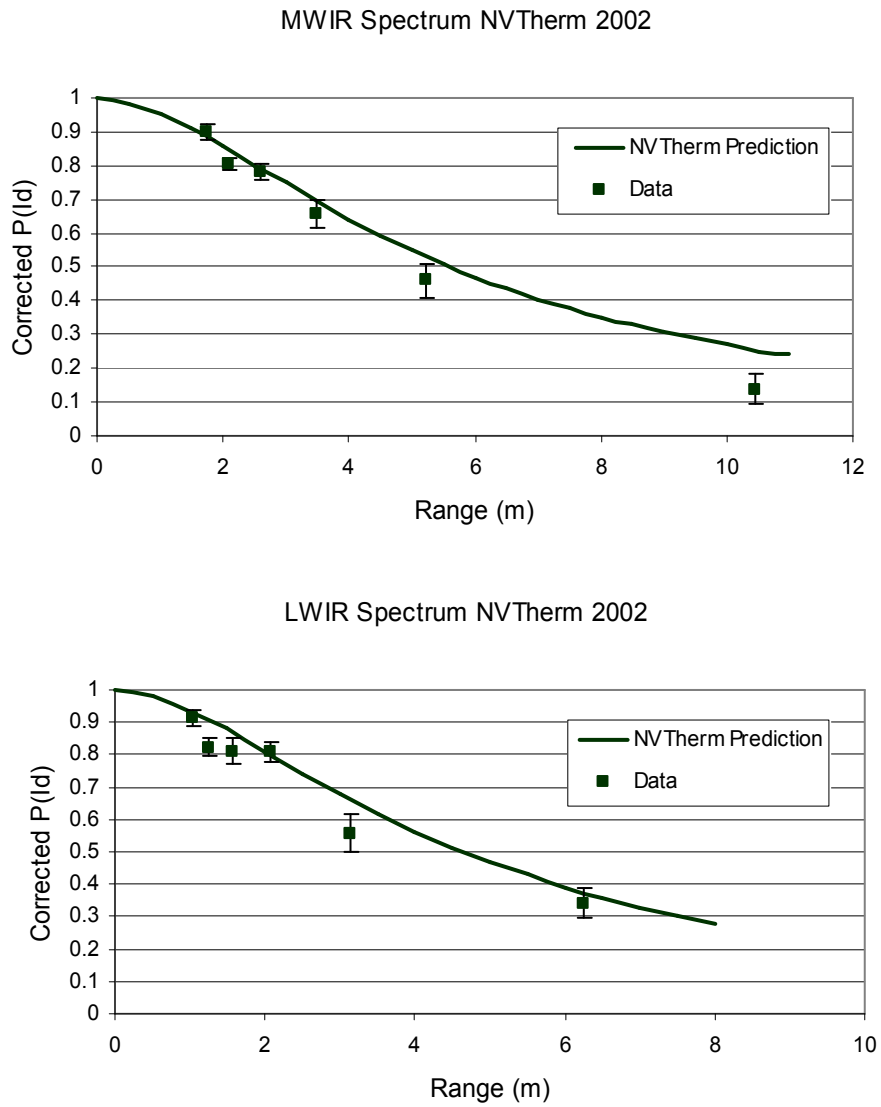


Figure 36. Measured probabilities of identification and NVTherm 2002 range performance predictions for both the MWIR and LWIR sensors.

NVTherm 2002 tended to overpredict the measured probabilities of identification for these average systems. However, even with the simplification that all additional pre-sample MTFs were the same as an average value, the range prediction curves came within a few percentage points of each measured data points error bars.

## ***5.7 Handheld Object Discussion***

The purpose of this portion of the research was to develop a target acquisition model to accurately predict thermal imager range performance when used to identify objects held in a human hand. Two human perception experiments were conducted: One measured the psychophysical model discrimination criteria required to quantitatively describe the difficulty of the task and the second confirmed the measurement technique used and its ability to interact with NVTherm 2002 to accurately describe human performance..

The discrimination criteria experiment developed a target acquisition model for both spectra under investigation. This was the first application of the ACQUIRE methodology to the identification of a set of targets other than vehicles and the first target acquisition model that included inanimate objects interacting with humans. The percent difference between the MWIR and LWIR spectrum  $N_{50}$  factors was 2 percent. This means, to the human observer, the task of identifying small handheld objects can be performed equally well in the MWIR and LWIR spectrum.

The validation perception experiment served as a test of realistic conditions for thermal imagers. To achieve this, the images were processed to simulate range effects. For the 12 data points that existed between the spectra, 25 percent of the model predictions were within the statistical error of the measured data and over 90 percent of

the model predictions were within 8 percent of the statistical error of the measured data. This confirmation experiment allowed both the thermal imager model and the range performance model to be used. These statistical models working together provided good agreement to the measured observer responses and verified the measurement methodology developed in the discrimination criteria experiment.

Also shown in my research is the ability of the ACQUIRE methodology to be adapted to a new set of targets, with a high degree of confidence, taking into account that the ACQUIRE methodology is purely statistical: the descriptors of the target set are an average statistical measurement of target contrast and area representation, two measured values that encapsulate the target set, and the task difficulty descriptor  $N_{50}$ .

## 6 Discussion

According to Lloyd [33], an imager may possess up to seven degrees of freedom, as shown in Table 16; three spatial dimensions, time, intensity, wavelength, and polarization. The three spatial dimensions are vertical, horizontal, and range. Most imagers perspective map the vertical and horizontal dimensions and collapse the range onto this 2-D array. Time is addressed by the length of time the imager integrates a scene and also the thermal imager frame rate. An imager maps both the temporal change and location of different intensities. However, with manual and automatic gain controls, the intensity of a scene may have a non-unique mapping to the display. An imager is sensitive to specific wavelengths; for a broadband LWIR thermal imager, the detectors are sensitive to all wavelengths between 8 and 12  $\mu\text{m}$ . An imager may only receive select polarizations of radiation. Useful thermal imager performance models need to accurately account for each of the seven degrees a thermal imager possesses.

Table 16. Comparison of Loyd’s seven degrees of freedom as applied to past, present, and future generations of thermal imagers.

	1 <sup>st</sup> -Gen	2 <sup>nd</sup> -Gen	3 <sup>rd</sup> -Gen	4 <sup>th</sup> -Gen	Future-Gen
3-D	2-D fixed	Fixed (higher res.)	Fixed (staring)	Fixed (staring)	Variable
Time	Fixed	Fixed	Variable	Variable	Variable
Intensity	Sensed	Sensed	Sensed	Sensed	Sensed
Wavelength	BW fixed	BW fixed	BW fixed	Variable	Variable
Polarization	All	All	All	All	Variable

Future thermal imagers may exploit all degrees of freedom. Detector sizes continue to decrease, allowing for finer samples of the horizontal and vertical dimensions. Techniques such as laser range gated imagers could provide range information at user defined resolutions. Integration time and intensity are currently user adjustable parameters for thermal imagers. Tunable focal plane arrays and polarizing optics would allow the user to define not only the wavelengths that are detected but also the polarization of incident radiation. The current state of thermal imager modeling is unable to address the performance impacts of all of the degrees of freedom.

First- and second-generation thermal imagers were very limited in the number of degrees of freedom. The detector vertical dimension was fixed. The horizontal dimension and integration time could be varied based on the thermal imager scan rate. These imagers also allowed for user-defined intensity mappings. However, the thermal imager was sensitive to a single broad band group of wavelengths, accepted all polarizations of

radiation, and did not provide any range data. The performance of these early generation thermal imagers was well modeled.

Third-generation thermal imagers have been defined as staring array focal planes with 20  $\mu\text{m}$  detectors that are sensitive to both the MWIR and LWIR wavebands. While not allowing complete user-defined control of all seven degrees of freedom, this next generation of thermal imager does provide smaller detectors, user-defined integration time, intensity mapping, and sensitivity to multiple broad bands of wavelengths. This imager could provide range information if coupled to a thermal source such as a MWIR laser, but the imager will not provide any polarization selectivity. The current thermal imager performance models cannot assess the abilities of third generation thermal imagers.

The current mathematical models are insufficient in describing future generations of thermal imagers. The impacts of techniques, such as super resolution, which increases thermal imager spatial sampling frequencies, and image fusion, the combination of separate discrete wavelength images, are unknown. The human performance impact of color images vice monochrome or gray scale imagery is also unknown. However, issues that need immediate addressing are further investigation of the performance impacts of discrete sampling of a scene, the performance impact of utilizing multiple wavelengths, and the characterization of environments other than open field combat.

The research presented in this dissertation showed the development and confirmation of a thermal imager performance model for small handheld objects, which may be used for multiple wavebands which also takes into account the performance impact of under-sampled thermal imagers. Additional research was performed in

comparing the spectral information content differences between different infrared wavebands and the refinement of the performance degradation resulting from the amount of aliasing that occurs in an image.

By investigating the performance of theoretical under-sampled imagers, thermal imagers could be designed better with the desired amount and optimum location of the aliased spectrum to minimize the impact of sampling on human performance. This research considered not just the amount of aliasing that occurred but also investigated the human performance effects on the location of the aliased spectrum. The results from the historical sampled imager experiments combined with the results of this dissertations research defined the relationship used in the thermal imager model NVTherm2002 to accurately predict the performance degradation of under-sampled thermal imagers.

A technique for acquiring and radiometrically correcting thermal imagery was developed in this research to compare information differences of military vehicles and natural backgrounds between spectral images. The information comparison metric chosen was the correlation coefficient. In the execution of this research, the impact of dead pixels and thermal imager noise on the correlation coefficient was quantified. In the case of imager noise, a method was developed that allowed the correlation coefficient to be corrected to a noise free value. This technique is a first step towards collecting imagery for spectral comparison outside of a laboratory environment while accounting for specific errors of dead pixels and thermal imager noise.

My research was the first application of the ACQUIRE methodology to the identification of a set of small handheld objects. This performance model was empirically developed through the use of forced-choice human perception experiments. The model

was shown to be correct through independent experimentation. For the confirmation experiment, the effects of aliasing were mitigated through experimental design and image processing. The performance model was developed for both the MWIR and LWIR spectra.

Third-generation thermal imagers have been defined as staring array focal planes with 20  $\mu\text{m}$  detectors that are sensitive to both the MWIR and LWIR wavebands. Reported in this research are experimental results that refined the performance impacts of insufficient scene sampling, the development of a methodology to measure the information differences between discrete wavelength images, and the development of a target acquisition model that addresses not only multiple wavebands but also a target set other than vehicles. The completion of these three tasks has provided critical steps toward improving the accuracy of modeling third-generation thermal imagers.

## 7 Recommendations

There still exist several research areas that need to be investigated. The quantities of aliasing investigated in this and previous research have not been exhaustive. With the utilization of electronic image enhancements such as electronic zoom, large levels of aliasing can be achieved in thermal imagers. Larger levels of aliasing need to be investigated and the models changed as necessary to accurately predict thermal imager performance.

The correlation coefficient has been a useful method to quantify information differences between different data sets. To fully investigate the effects of different uncertainties on this method, more imager-type uncertainties need to be investigated such as optical distortion and spectral MTF differences. Calibrating the correlation coefficient to a human performance measure would allow the mathematical computation to aid in evaluating the potential human impact on an observer.

Currently, the only reliable methodology for developing an ACQUIRE-type model for other object or target sets is an empirical method through the use of human perception experiments. The goal of research in this area should be minimizing the reliance on human perception experiments and, eventually, the ability to develop human perception models without observer input.

## 8 References

---

1. U. S. Army Night Vision and Electronic Sensors Directorate, *FLIR92 Thermal Imaging Systems Performance Model Analyst's Reference Guide*, Ft. Belvoir, VA, (1993).
2. M. C. Dudzik, "Electro-Optical Systems Design, Analysis, and Testing," *The Infrared and Electro-Optical Systems Handbook*, Vol. 4, Environmental Research Institute of Michigan, Ann Arbor, Michigan, (1993).
3. J. A. Ratches, W. R. Lawson, L. P. Obert, R. J. Bergemann, T. W. Cassidy, and J. M. Swenson, "NVL Static Performance Model for Thermal Viewing Systems." U. S. Army, Army Electronics Command, Ft. Monmouth, NJ. Tech. Rep. ECOM-7043, April, (1975).
4. J. A. Ratches, R. Vollmerhausen, and R. Driggers, "Target Acquisition Performance Modeling of Infrared Imaging Systems: Past, Present, and Future," *IEEE Sensors J.*, **1**, 31, (2001).
5. R. Vollmerhausen, "Incorporating Display Limitations into Night Vision Performance Models," *Proc. IRIS Specialty Group on Passive Sensors*, **2**, 11, (1995).
6. U. S. Army Night Vision and Electronic Sensors Directorate, *Night Vision Thermal Imaging Systems Performance Model Users Manual and Reference Guide*, Ft. Belvoir, VA, (2002).
7. J. Johnson, "Analysis of Image Forming Systems," *Proc. Image Intensifier Symposium*, 249, (1958).
8. J. A. Ratches, "Static Performance Model for Thermal Imaging Systems", *Opt. Eng.* **15**, 525, (1976).
9. J. A. Ratches, "Comparison of NVL Model and Four Contractor Models for Minimum Resolvable Temperature (MRT)", U. S. Army, Army Electronics Command, Ft. Monmouth, NJ. Tech. Rep. ECOM-7050, January (1976).
10. J. A. Ratches, "NVL modeling; historical perspective", *Proc. SPIE Conf. on Infrared Imaging Systems*, **3701**, 1, 1999.
11. W. R. Lawson, and J. A. Ratches, "Modeling Detection or The Detection Game", *Proc. IRIS Specialty Group on Targets, Backgrounds and Discrimination*, (1980).
12. M. Self, B. Miller, and D. Dixon, "Acquisition Level Definitions and Observables for Human Targets, Urban Operations, and the Global War on Terrorism," U. S. Army, Night Vision and Electronic Sensors Directorate, Ft. Belvoir, VA Tech. Rep. AMSRD-CER-NV-TR-235, March, 2005.

- 
13. L. M. Biberman (Ed.), "Electro-Optical Imaging System Performance and Modeling," Ch. 12, SPIE, Bellingham, WA, (2000).
  14. R. G. Driggers, C. Webb, S. J. Pruchnic Jr., C. E. Halford, and E. E. Burroughs Jr., "Laboratory measurements of sampled infrared imaging system performance," *Opt. Eng.*, **38**, 852, (1999).
  15. M. A. Chambliss, J. A. Dawson, and E. J. Borg, "Measuring the MTF of undersampled staring IRFPA sensors using 2D discrete Fourier transform," *Proc. SPIE Conf. on Infrared Imaging Systems*, **2470**, 312, 1995.
  16. Z. Fang, G. Zhiyun, S. Meikai, and L. Guangrong, "An approach for MTF measurement of discrete imaging system," *Proc. SPIE Conf. on Electr. Imaging and Multimedia Tech.*, **4925**, 668, 2002.
  17. T. L. Williams, and N. T. Davidson, "Measurement of the MTF of IR staring array imaging systems," *Proc. SPIE Conf. on Infrared Imaging Systems*, **1689**, 53, 1992.
  18. E. L. Dereniak, and G. D. Boreman, *Infrared Detectors and Systems*, Ch. 14, p. 531, John Wiley and Sons, Inc., 1996.
  19. L. Scott, J. D'Agostino, and C. Webb, "Applications of 3-D Noise to MRTD Prediction," *Proceedings of IRIS Passive Sensors*, **1**, 65, 1992.
  20. J. A. D'Agostino, "The Modeling of Spatial and Directional Noise in FLIR90 Part1: A 3-D Noise Analysis Methodology," *Proc. of IRIS Passive Sensors*, **1**, 211, 1991.
  21. C. M. Webb, "An Approach to 3-Dimensional Noise Spectral Analysis," *Proceedings of SPIE*, vol. 2470, pp.288-299, 1995.
  22. E. Jacobs, J. Cha, K. Krapels, and V. Hodgkin, "Assessment of 3-D Noise Methodology for Thermal Sensor Simulation," *Proceedings of SPIE*, vol. 4372, pp.154-161, 2001.
  23. C. Webb, "Laboratory Analysis of Discretely Sampled Thermal Imaging Systems," *Proc. of IRIS Passive Sensors*, **1**, 311, 1990.
  24. R. Vollmerhausen, R. G. Driggers, C. Webb, and T. C. Edwards, "Staring imager minimum resolvable temperature measurements beyond the half sample rate," *Opt. Eng.*, **37**, 1763, 1998.
  25. P. Bijl, and J. M. Valetton, "Triangle orientation discrimination: the alternative to minimum resolvable temperature difference and minimum resolvable contrast," *Optical Engineering*, vol. 37, no. 7, pp.1976-1983, July 1998.

- 
26. P. Bijl, and J. M. Valeton, "Validation of the new triangle orientation discrimination method and Acquire model predictions using observer performance data for ships," *Optical Engineering*, vol. 37, no. 7, pp.1984-1994, July 1998.
  27. P. Bijl, J. M. Valeton, and A. N. de Jong, "TOD predicts target acquisition for staring and scanning thermal imagers," *Proceedings of SPIE*, vol. 4030, pp.96-103, 2000.
  28. P. Bijl, M. A. Hogervorst, and J. M. Valeton, "TOD, NVTherm, and TRM3 model calculations: a comparison," *Proceedings of SPIE*, vol. 4719, pp.51-62, 2002.
  29. W. Wittenstein, "Minimum temperature difference perceived- a new approach to assess undersampled thermal imagers," *Optical Engineering*, vol. 38, no. 5, pp. 773-781, May 1999.
  30. O. Schade, "Image Reproduction by a Line Raster Process," *Perception of Displayed Information*, (L. Biberian, Ed.), 233, Plenum, New York, (1973).
  31. R. Legault, "The Aliasing Problems in Two-Dimensional Sampled Imagery," *Perception of Displayed Information*, (L. Biberian, Ed.), 279, Plenum, New York, (1973).
  32. C. H. Sequin, "Interlacing in Charged-Coupled Imaging Devices," *IEEE Transactions on Elec. Devices*, **20**, 535, (1973).
  33. J. M. Loyd, *Thermal Imaging Systems*, 1<sup>st</sup> ed., Plenum Press, New York, 1982.
  34. H. R. Luxenberg and R. L. Kuehn, *Display Systems Engineering*, McGraw-Hill, 1968.
  35. W. E. Glenn, "Visual perception studies to improve the perceived sharpness of television images," *Journal of Electronic Imaging*, **13**, 3, (2004).
  36. W. Wittenstein, W. Fick, and U. Raidt, "Range Performance of Two Staring Imagers - Presentation of the Field Trial and Data Analysis," *Proc. SPIE Conf. on Infrared Imaging Systems*, **2743**, 132, (1996).
  37. C. M. Webb and C. E. Halford, "Dynamic Minimum Resolvable Temperature Difference Testing for Staring Array Imagers," *Opt. Eng.*, **38**, 845, (1999).
  38. S. Park and R. Hazra, "Aliasing as Noise: A Quantitative and Qualitative Assessment," *Proc. of SPIE Conf. on Infrared Imaging Systems*, **1969**, 54, (1993).
  39. T. Meitzler and G. Gerhart, "Spatial Aliasing Effects in Ground Vehicle IR Imagery," *Proc. SPIE Conf. on Infrared Imaging Systems*, **1689**, 226, (1992).

- 
40. P. Owen and J. Dawson, "Resolving The Differences In Oversampled and Undersampled Imaging Sensors: Updated Target Acquisition Modeling Strategies for Staring and Scanning FLIR Systems," *Proc. SPIE Conf. on Infrared Imaging Systems*, **1689**, 251, (1992).
  41. F. Huck, S. Park, D. Speray, and N. Halyo, "Information Density and Efficiency of Two-Dimensional Sampled Imagery," *Proc. SPIE Conf. on Image Quality*, **310**, 36, (1981).
  42. J. Kruthers, T. Williams, G. O'Brien, K. Le, and J. Howe, "Study of the Effects of Focal Plane Array Design Parameters on ATR Performance," *Proc. SPIE Conf. on Arch., Hardware, and FLIR Issues in Automatic Object Recognition*, **1957**, 165, (1993).
  43. J. D'Agostino, M. Friedman, R. LaFollette, and M. Crenshaw, "An Experimental Study of the Effects of Sampling on FLIR Performance," *Proc. IRIS Specialty Group on Passive Sensors*, (1990).
  44. J. Howe, L. Scott, S. Pletz, J. Horger, and J. Mark, "Thermal Model Improvement Through Perception Testing," *Proc. IRIS Specialty Group on Passive Sensors*, (1990).
  45. R. Vollmerhausen, "Impact of display modulation transfer function on the quality of sampled imagery," *Proc. SPIE Conference on Infrared Imaging Systems*, **2743**, 12, (1996).
  46. R. Vollmerhausen, "Display of Sampled Imagery," *Proc. IRIS Specialty Group on Passive Sensors*, **1**, 175, (1990).
  47. R. H. Vollmerhausen and R. G. Driggers, *Analysis of Sampled Imaging Systems*, SPIE Tutorial Texts in Optical Engineering, Bellingham, WA, SPIE Press, 2000.
  48. R. G. Driggers, R. H. Vollmerhausen, B. L. O'Kane, "Equivalent Blur as a function of spurious response of a sampled imaging system: application to character recognition," *J. Opt. Soc. Am. A*, **16**, 1026, (1999).
  49. R. H. Vollmerhausen, R. G. Driggers, B. L. O'Kane, "Influence of sampling on target recognition and identification," *Opt. Eng.*, **38**, 763, (1999).
  50. S. Park and R. Schowengerdt, "Image Sampling, Reconstruction, and the Effect of Sample-Scene Phasing," *App. Opt.*, **21**, 3142, (1982).
  51. W. Wittenstein, J. Fontanella, A. Newberry, and J. Baars, "The Definition and the OTF and the Measurement of Aliasing for Sampled Imaging Systems," *Opt. Acta*, **29**, 41, (1982).

- 
52. J. N. Cederquist, T. J. Rogne, and C. R. Schwartz, "Multispectral infrared target detection: phenomenology and modeling." SPIE vol. 1954, pp.192-197, 1993.
  53. M. T. Eisman, J. N. Cederquist, and C. R. Schwartz, "Infrared Multispectral Target/Background Field Measurements," SPIE vol. 2235, pp. 130-147, 1994.
  54. W. A. Shaffer and R. O. Johnson, "Infrared multispectral field measurements for the Joint Multispectral Program," SPIE vol. 2469, pp. 537-547, 1995.
  55. A. D. Stocker, A. Oshagan, W. A. Shaffer, M. R. Surette, M. J. McHugh, A. P. Schaum, M. T. Eismann, K. K. Ellis, R. A. Maxwell, J. H. Seldin, "Analysis of Infrared Hyperspectral Measurements by the Joint Multispectral Program," SPIE vol.2469, pp.587-602, April 1995.
  56. C. R. Schwartz, J. N. Cederquist, D. R. Twede, and M. T. Eisman, "Detection Of Low Contrast CC&D Targets Using Hyperspectral Infrared Image Data," Proceedings of IRIS Specialty Group on Camouflage Concealment and Deception, pp.1-15, October, 1997.
  57. J. C. Leachtenauer, R. G. Driggers, *Surveillance and Reconnaissance Imaging Systems Modeling and Performance Prediction*, 1<sup>st</sup> ed., Artech House, Massachusetts, 2001.
  58. P. G. Lucey, T. Williams, M. Mignard, J. Julian, D. Kokobun, G. Allen, D. Hampton, W. Schaff, M. Schlangen, E. M. Winter, W. Kendall, A. Stocker, K. Horton, and A. P. Bowman, "AHI: An airborne long wave infrared hyperspectral imager," *Proc. SPIE Conference on Airborne Reconnaissance*, **3431**, 36, (1998).
  59. M. P. Satyshur, D. A. Scribner, and M. R. Kruer, "Multispectral Imaging: Band Selection and Performance Predictions," *Proc. IRIS Specialty Group on Targets and Backgrounds*, (1997).
  60. D. A. Scribner, J. Schuler, and M. R. Kruer, "Infrared Multispectral Sensors: Reconsidering Design Assumptions," *Proc. IRIS Specialty Group on Targets and Backgrounds*, (1998).
  61. S. Evans, J. Hargreaves, P. Evans, P. Randall, and M. Bernhardt, "SPIRIT: A Hyperspectral Infrared Imager." *Proc. SPIE Conference on Signal and Data Processing of Small Targets*, **3809**, 174, (1999).
  62. K. J. Barnard, M. T. Eismann, C. R. Schwartz., and M. Nayeri, "Optimization of Thermal Multispectral Sensors for Detecting Camouflaged and Concealed Targets," *Proc. MSS National Military Sensing Symposium*, (2001).

- 
63. H. L. Van Trees, *Detection, Estimation, and Modulation Theory*, 1<sup>st</sup> ed., John Wiley and Sons, New York, 2001.
64. S. Moyer, R. G. Driggers, R. Vollmerhausen, M. Soel, P. Warren, G. Welch, and W. T. Rhodes, "Information Differences between Sub-bands of the Infrared Spectrum over the Diurnal Cycle," *Proc. MSS Specialty Group on Passive Sensors*, (2002).